Doctoral Dissertation

A Study on Ordering of Fe Atoms in Fe_xTiS_2 Structures and Their Magnetic Properties

Chiew Yi Ling

Supervisor: Prof. Yoshifumi Oshima

Graduate School of Advanced Science and Technology
Japan Advanced Institute of Science and Technology
[Materials Science]

September 2020

Referee-in-chief:

Professor Yoshifumi Oshima
Japan Advanced Institute of Science and Technology

Referees:

Professor Masahiko Tomitori
Japan Advanced Institute of Science and Technology
Professor Mikio Koyano
Japan Advanced Institute of Science and Technology
Professor Eisuke Tokumitsu
Japan Advanced Institute of Science and Technology
Professor Shigeo Ohara
Nagoya Institute of Technology

ABSTRACT

A Study on Ordering of Fe Atoms in Fe_xTiS_2 Structures and Their Magnetic Properties

Chiew Yi Ling
s1720417

Two dimensional transition metal dichalcogenide (TMDC) structures have received much interest due to the emergence of unique physical or chemical properties by being intercalated with various guest atoms or molecules. Thus, extensive studies have been performed to synthesize such intercalated layered structures for various applications such as superconductors, thermal conductors and magnetic materials. Iron-intercalated titanium disulfide (Fe_xTiS_2) structure, which is one of such materials, had been reported to show various magnetic or thermoelectric properties that varied depending on the concentration of Fe atoms in the van der Waals gaps of the TiS_2 host structure. So, to fully understand the physical properties of Fe_xTiS_2, it is important to first know the arrangement of Fe atoms. Experimental and theoretical calculations had been performed to identify the ordering of Fe atoms in Fe_xTiS_2 at different concentrations but no conclusive results could be obtained since some showed contradictory results. So, it is worth investigating these samples with transmission electron microscopy (TEM) since they could provide more in depth information on the local ordering of Fe atoms in the van der gaps of the host structures. In this study, we have investigated the Fe_xTiS_2 structures with various Fe concentrations systematically to clarify the arrangement of intercalated Fe atoms in the TiS_2 structure by transmission electron diffraction (TED) and scanning transmission electron microscopy (STEM) observation. Especially since atomic resolved STEM image is a powerful tool in identifying individual Fe atoms, it can be used to find the short range ordering of Fe atoms at low intercalation concentrations.

STEM observations of the crystals three-dimensionally revealed short-range in-plane ordering of $\sqrt{3}a$ and $2a$ at $x \leq 0.15$, with a higher ratio of atoms with $\sqrt{3}a$ distances. $x = 0.20$ showed the onset of three-dimensional ordering of Fe atoms within the planes and along the *c*-axis, forming short-range ordering of $2a \times 2a \times 2c$. As more Fe atoms were intercalated, long-range ordering of $2a \times 2a \times 2c$ at $x = 0.25$ and $\sqrt{3}a \times \sqrt{3}a \times 2c$ at $x = 0.33$ were observed. The ordering of the Fe atoms could be attributed to the Fe interatomic interactions. At low Fe concentrations ($x \leq 0.15$), Fe atoms would only interact with one another within the plane and thus the main interaction was repulsive forces, creating preferential atomic pairs at $\sqrt{3}a$ distances. Whereas at higher Fe concentrations ($x \geq 0.20$), there were more Fe atoms between the TiS_2 layers and thus the interaction of Fe atoms between the layers would influence the atomic arrangement of Fe atoms in the layers as well, thus creating 3D superstructures.

TED analysis using Patterson method revealed some unprecedented superstructures of $\sqrt{7}a \times \sqrt{7}a$, $\sqrt{31}a \times \sqrt{31}a$ and $\sqrt{43}a \times \sqrt{43}a$, which is equivalent to Fe concentrations of 0.14, 0.29 and 0.26, respectively. In these superstructures, the Fe atoms were separated almost equidistant, suggesting that the Fe atoms would always try to distance themselves equally apart and thus, they did not only occupy octahedral sites as previously reported, but at tetrahedral sites as well. The occupancy of Fe atoms at tetrahedral sites was confirmed by STEM imaging which showed some darker contrasts at S site, which is also known as the tetrahedral sites.

Lastly, the magnetic measurements showed that the crystals switched from spin glass behavior at $x \leq 0.15$ to ferromagnetic behavior at $x \geq 0.20$. The onset of ferromagnetic behavior at $x = 0.20$ was a match to the onset of 3D Fe ordering at $x = 0.20$ in the STEM observation. So, the magnetic properties displayed by these crystals could be a result of whether the crystal had 2D Fe ordering or 3D Fe ordering. The short-range in-plane ordering at low concentrations indicated smaller exchange interactions of the spins and thus led to spin glass behavior. Whereas at higher concentrations, the 3D Fe ordering meant stronger exchange interactions of the spins, which allowed the spins to align easier to the magnetic field and thus display ferromagnetic behavior.

Keywords: Fe_xTiS_2, superstructure, atomic ordering, electron diffraction, scanning transmission electron microscopy

ACKNOWLEDGEMENT

First, I would like to express my sincere gratitude to my supervisor, Prof. Yoshifumi Oshima for his kind guidance and constructive suggestions in the completion of this work. I am really thankful to him for teaching me everything on transmission electron microscopy and even allowing me the chance to have hands on experience on the systems. His constant patience and consideration towards students also eased my time as a student here in JAIST.

I am also deeply grateful to Prof. Mikio Koyano and Prof. Masanobu Miyata in JAIST for providing their valuable technical support and helpful discussion sessions in understanding the magnetic aspects of my work. I am totally new in the field of magnetism and yet both of them were really patient with me and provided all the support I needed.

In addition, I would like to extend my gratitude to Assoc. Prof. Zhang Xiaobin. While she was working here in JAIST, she taught me a lot on the operations and principles of transmission electron microscope. She was also very kind in helping me adapting to life in Japan when I first arrived and even though she no longer work in JAIST, she is still being very helpful and will provide any support or suggestions needed.

Special thanks to the staffs of the Center for Nano Materials and Technology in JAIST as well for their support, teaching and valuable suggestions in the operations of the TEM, SEM and FIB systems.

I would also like to acknowledge my gratitude to MEXT and JAIST for providing me the financial support, research and travel grants that are essential for my life here in Japan and the

completion of my work.

Lastly, special thanks to my family, fellow labmates and friends for their constant understanding, encouragement and their support no matter the situation. They really helped me to stay focused while remained positive in moving towards my goal.

TABLE OF CONTENT

CHAPTER 1

Introduction

Intercalation in two-dimensional (2D) transition metal dichalcogenides (TMDCs) have attracted attention for the past several decades due to their tunability in physical and chemical properties. Iron-intercalated titanium disulfide (Fe_xTiS_2) is one such material. When intercalated with Fe atoms, the material's properties were found to be different from that of the host structure. Different magnetic phases have also been reported for the intercalated Fe_xTiS_2. They exhibited either spin glass or cluster glass behavior at low Fe concentrations and ferromagnetic behavior at high Fe concentration [1], [2]. Through specific heat measurement, photoemission spectroscopic studies and transport measurements, it was found that charge transfer from the Fe atoms to the host Ti 3d conduction band occurred and this led to a change in the Fermi energy E_F and density of states at E_F when Fe atoms are intercalated into TiS_2 [3]. The change in the electronic structure might have led to the different properties observed in the intercalated materials as compared to the host structure.

How the electronic band structure was changed would depend on the concentration of Fe atoms intercalated and the arrangement of iron atoms in the TiS_2 host structure [3]. There are two possible sites in which Fe atoms could occupy in the van der Waals gaps of the TiS_2 layers, namely the tetrahedral and octahedral interstitial sites but Fe atoms had been reported to occupy only octahedral sites [3]. As more atoms occupy these interstitial sites, ordering of these atoms would form new unit cells that are larger than that of TiS_2. Therefore, they can create various forms of superstructures. XRD studies have shown the formation of $2\sqrt{3}a \times 2a \times 2c$ or $2a \times 2a \times 2c$

superstructures at $x = 0.25$ and $\sqrt{3}a \times \sqrt{3}a \times 2c$ at $x = 0.33$ but no data could be obtained for the Fe ordering at low concentrations [4]. However, recently, another study only showed the formation of $\sqrt{3}a \times \sqrt{3}a$ superstructure in Fe_xTiS_2 using transmission electron diffraction (TED) at $0.086 \leq x \leq 0.703$ displaying different magnetic behavior [5]. The contradicting structural results might have led to the different magnetic behavior. Thus, it is important to understand the atomic structure of Fe_xTiS_2 formed at different Fe concentrations.

Transmission electron microscopy (TEM) offers a solution to this problem. It is a powerful system with high resolution down to 2 Å, which allows us to view individual atomic columns and gives us an insight of the atomic structure of materials. This would especially be useful in identifying the arrangement of intercalated Fe atoms in the Fe_xTiS_2, especially for low Fe concentrations.

The goal of this thesis is to study the different Fe ordering in Fe_xTiS_2 at varying Fe concentrations by means of transmission electron microscope techniques and then correlate the measured magnetic properties to the Fe orderings. Fe_xTiS_2 specimens would be prepared by chemical vapor transport method and then subjected to structural characterization using X-ray diffraction (XRD) and transmission electron microscopy (TEM). DC magnetic measurements were performed and these results were then correlated to the identified Fe ordering.

Chapter 2 of this thesis explains some fundamental concepts. A brief explanation is given on the transition metal dichalcogenides and the effect of intercalation on the atomic structures. Some fundamental knowledge of transmission electron microscopy and basic concepts of magnetism are included as well.

Chapter 3 is focused on the structural analysis of Fe_xTiS_2 using transmission electron microscopy techniques. Combining the different modes of TEM, which include scanning

transmission electron microscope (STEM), TED, electron energy loss spectroscopy (EELS) and energy dispersive spectroscopy (EDS) analyses, the Fe ordering of Fe_xTiS_2 at different concentrations were determined and the ordering mechanisms were discussed.

Chapter 4 is focused on the study of Fe_xTiS_2 unknown superstructure using transmission electron diffraction. Superstructures with unknown symmetry could be determined by performing Fourier transform on the electron diffraction pattern to create a partial Patterson map that shows a map of different Fe atomic correlations. From this map, the Fe arrangement in the superstructure could be deduced.

Chapter 5 is focused on the magnetic measurement of Fe_xTiS_2 grown at different concentrations of Fe. The correlation of the magnetic properties with the structural information obtained from TEM studies is also included in the thesis.

Lastly, Chapter 6 summarizes the work performed in this thesis.

CHAPTER 2

Fundamental Concepts

2.1. Transition metal dichalcogenides (TMDC) and Intercalation

2.1.1. Transition metal dichalcogenide (TMDC)

Transition metal dichalcogenides (TMDC) are a class of two-dimensional (2D) compounds with the general formula TX_2, where T is a transition metal from groups IVb, Vb or VIb, and X is a chalcogen (S, Se or Te). Each TX_2 slab is consisted of one layer of T atoms sandwiched between two layers of X atoms, as shown in Figure 2.1.

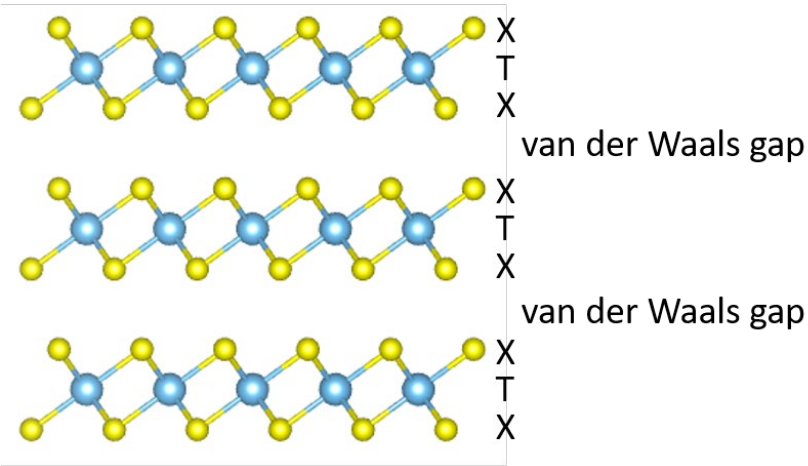

Figure 2.1: Schematic showing transition metal dichalcogenide TX2 sandwiches separated by van der Waals gaps

Each T atom in the slab is always bonded to six X atoms, either in trigonal prismatic coordination or octahedral (also known as trigonal antiprismatic) coordination. Figure 2.2 shows these two types of TX_2 coordination. The type of coordination preferred depends on the ionicity of the T-X bond. The larger the difference in electronegativity between T and X, the more ionic

the bonding is. Trigonal prismatic coordination is typically found for more covalent compounds such as MoS_2 and NbS_2, while octahedral coordination is preferred for more ionic compounds since it maximizes the distance between the negatively charged X atoms [6].

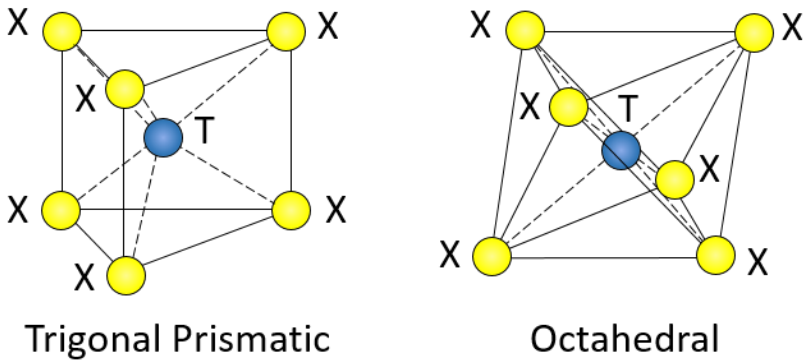

Figure 2.2: Trigonal prismatic and octahedral coordination polyhedrons of MX_2 where each T atom is surrounded by six X atoms

Since the X atoms of TX_2 have saturated orbitals, the slabs are only held together by weak van der Waals force. Due to these weak slab-to-slab interactions and the different TX_2 coordinations, various stacking sequences of TX_2 slabs are possible, which leads to the formation of different polytypes. The TX_2 stacking sequences can be represented by three non-equivalent atomic positions A, B and C in the close-packed stacking of (0001) hexagonal plane. Figure 2.3 shows the three atomic positions (A, B and C) in the close-packed stacking of (0001) plane. In the unit cell of TMDC, *a* and *b*-axes are defined by the nearest neighbor atomic correlation, X-X or T-T, and *c*-axis is defined by the perpendicular direction to the layers. Since there are two atomic species T and X, capital letters A, B and C would denote the X atoms, and small letters a, b and c would denote the T atoms at different planes. Using this notation, trigonal prismatic coordination is denoted as AbA, and octahedral coordination of TX_2 is denoted as AbC, as shown by the projection in $(11\bar{2}0)$ plane in Figure 2.3(b).

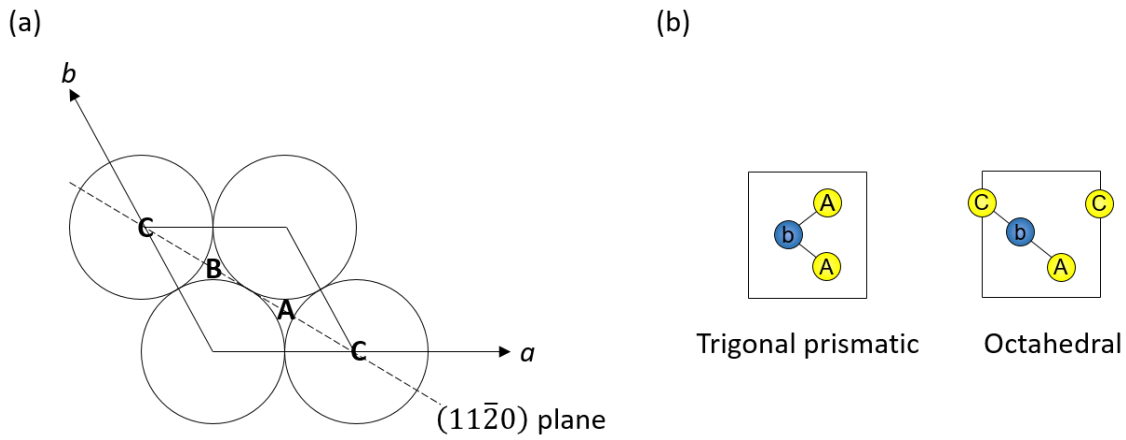

Figure 2.3: (a) Atomic positions for the ABC notations of stacking sequence, relative to the *a* and *b* axes in the (0001) plane. The diamond represents a unit cell. (b) Projection of trigonal prismatic and octahedral coordination of TX_2 in (11$\bar{2}$0) plane with the notations of AbA and AbC, respectively. Capital letters represent the X atoms and small letters represent the T atoms.

Some of the more commonly known polytypes for TMDCs are as shown in Figure 2.4, projected in the (11$\bar{2}$0) plane. These polytypes are normally identified by using a number and a capital letter based on the notations used by Brown and Beernsten [3]. The number represents the number of TX_2 slabs in the unit cell, whereas the letter represents the point symmetry such as trigonal (T), hexagonal (H) and rhombohedral (R). Sometimes, a small letter is seen next to the capital letter. It indicates different stacking sequences with the same lattice symmetry. For example, 1T structure means 1 TX_2 layer in the unit cell with trigonal symmetry.

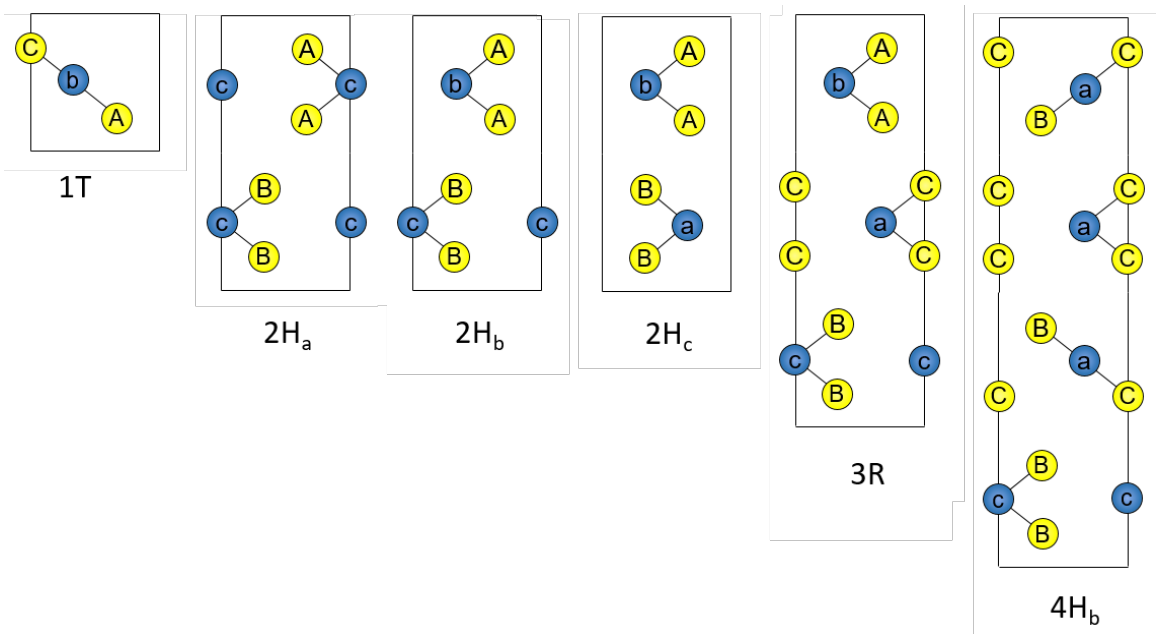

Figure 2.4: Some commonly known TMDC polytypes, projected in the $(11\bar{2}0)$ plane.

2.1.2. Intercalation Chemistry

Because of weak van der Waals forces between the TX_2 slabs, guest atoms or molecules could be inserted into these gaps. The insertion process of foreign species into the van der Waals gaps is known as intercalation. There are generally three categories of intercalation compounds that could be inserted into TMDC. These consist of alkali metal atoms (Li, Na, K and Rb), organic molecules (amides, amines, pyridine, hydrazine that contain N atoms) and 3d transition metals (V, Cr, Mn, Fe, Co, Ni and Cu).

Due to the hexagonal packing and the compact interlayer stacking in TMDC, the intercalation compound could occupy either octahedral or tetrahedral interstitial sites in the van der Waals gaps. Figure 2.5 shows the locations of such octahedral and tetrahedral interstitial sites in the different TMDC polytypes. Typically, the number of octahedral interstitial sites is equal to the number of T atoms while for tetrahedral interstitial sites, it is equal to twice the number of T atoms in the unit cell [3]. Octahedral interstitial sites are usually found in intercalation of group 1A alkali metals

and 3d transition metals, whereas tetrahedral interstitial sites are found mostly in intercalation of hydrazine, silver and copper [7]. In some special cases, intercalation compounds such as larger alkali metal ions could also occupy trigonal prismatic interstitial sites, which is achieved by the rotation of adjacent TX_2 slabs for structure stability [8].

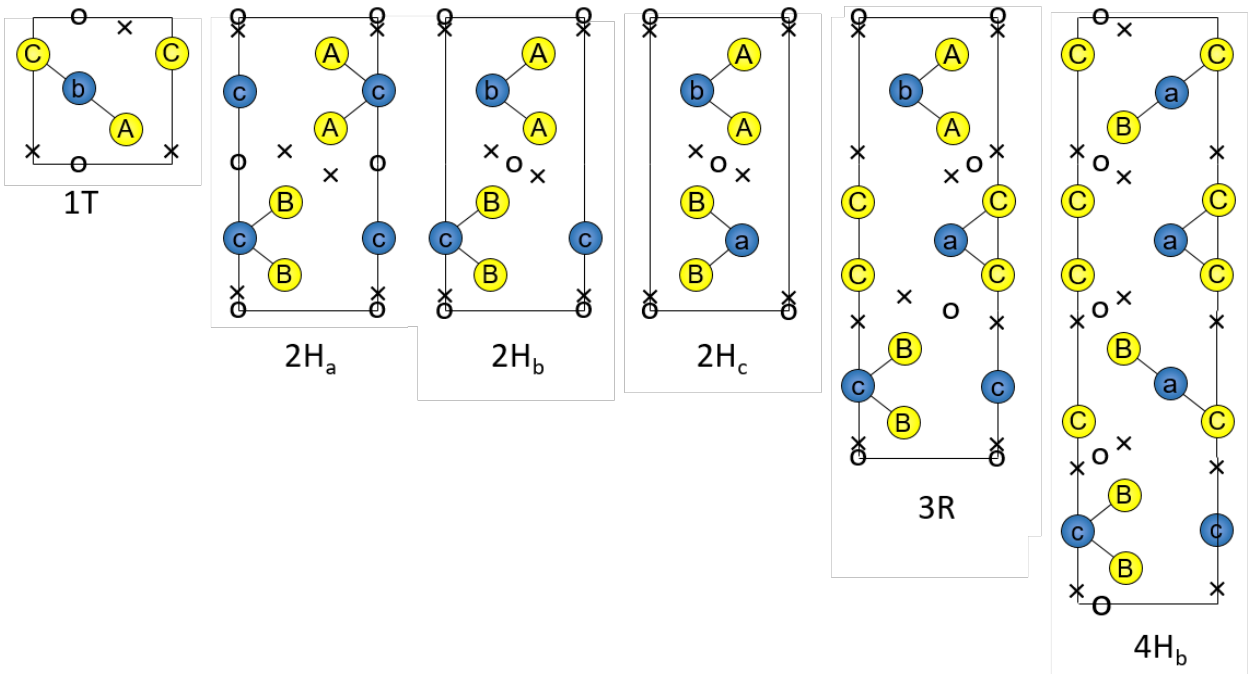

Figure 2.5: Octahedral (o) and tetrahedral (×) interstitial sites in the different TMDC polytypes.

Once these guest atoms are intercalated into the van der Waals gaps of TMDC, it causes two main effects to the host TX_2 structure. First is the change of the lattice constant in TX_2 host structure. The host structure is typically reported to expand slightly along the *c*-axis while the lattice constant in the *a*-axis does not change much. For example, when more 3d transition metal atoms (V, Cr, Mn, Fe, Co and Ni) were intercalated into TiS_2, X-ray diffraction (XRD) analysis showed that the lattice parameter *c* could be observed to increase substantially, as compared to the lattice parameter *a* [9]. The extent of structural expansion depends on several factors, which include bond ionicity, bond lengths, and atomic number of the guest atoms. For example,

intercalation of Co atoms into TiS_2 caused the host structure to shrink along the *c*-axis, rather than expand when more Co atoms were introduced into the host structure [9]. Second effect of intercalation would be the charge transfer between intercalated atoms and the host structure. For the case of TMDC, there have only been reports of intercalation of electron donor species. Thus, the electron transfers from intercalated atoms to host structure would cause a change in the electronic properties of host material.

2.2. Transmission electron microscopy (TEM)

The working principles of a conventional TEM are similar to that of a transmitted light microscope but instead of using photons, a beam of accelerated electrons is introduced onto the thin samples (< 100 nm). The wavelength of de Broglie electrons is given by the following formula:

$$\lambda = \frac{h}{\sqrt{2m_0 eE\left(1 + \frac{eE}{2m_0 c^2}\right)}}$$

where *h* is the Planck constant, *e* is the electron charge, m_0 is the electron mass, E is the incident energy in keV, *c* is the speed of light.

In any optical system, the resolution limit, d_0, is determined by Rayleigh's criterion, as shown below. This value describes the smallest resolvable distance between two points at any wavelength.

$$d_0 = \frac{0.61\lambda}{NA}$$

where NA is the numerical aperture, which is equal to $nsin\theta$. *n* is the refractive index of the medium and θ is the aperture angle. From this equation, one can see that the resolution limit is dependent

on the wavelength. So, in an electron microscope which uses electrons as illumination source, the resolution that could be achieved would be significant greater than that of light microscopy since the wavelength of electrons are very small. For example, a TEM operating at 200 kV would have a theoretical wavelength of electrons at 2.51 pm whereas the wavelength of visible light is 550 nm for green light. However, the resolution that could be reached by electron microscopes is limited by lens aberrations such as spherical aberration and chromatic aberrations.

The operations of TEM could be separated into three main parts, which consist of illumination, interaction of electrons with sample and imaging modes. This section will only explain about the interaction of electrons with sample and the imaging modes of scanning transmission electron microscopy and transmission electron diffraction.

2.2.1. Interactions of electrons with specimen

As the incident electron beam travel through the specimen, some electrons will pass through directly unaffected, some are deflected but do not lose energy while some are deflected with some energy loss [10], [11]. The deflected electrons that loses energy experience inelastic scatting while the deflected electrons that still have the same initial energy experience elastic scattering.

Two imaging models are used to obtain the atomic resolution images. The first model is related to Rutherford scattering. Here, the incident electrons are deflected by the atomic nuclei, as shown in Figure 2.6 (a). The angle of deflection is strongly dependent on the amount of positive charges in the nucleus, which is proportional to the atomic number. More electrons are deflected at high angles at higher atomic number. By detecting the electrons that are deflected at high angles, high angle annular dark field (HAADF) image can be obtained, where the intensity of each atomic

column is proportional to the square of the atomic number. Second model is related to Bragg scattering (low deflection angle). The electrons follow Bragg's law ($n\lambda = 2dsin\theta$) where incident electrons are deflected by crystal planes, as shown in Figure 2.6(b). Interference of the direct beam and the electrons in the crystal plane create phase contrast that corresponds to the projected atomic configuration in TEM imaging. In both of these scattering models, the deflected electrons do not lose energy.

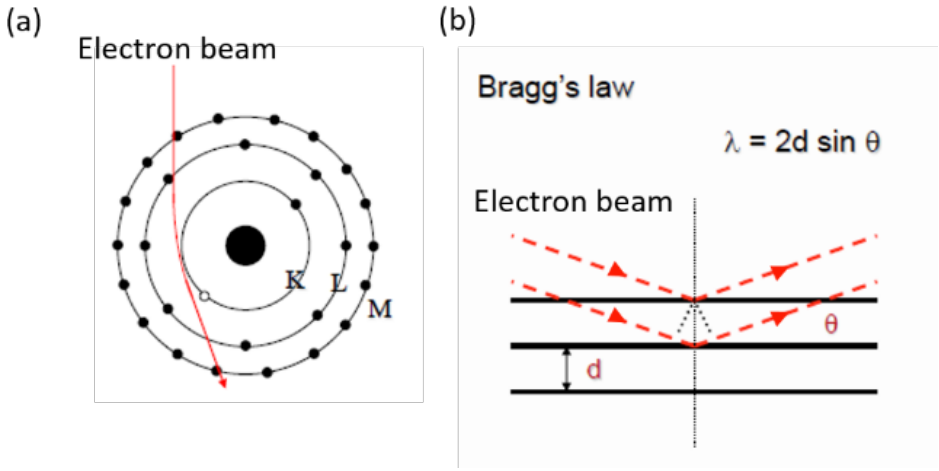

Figure 2.6: (a) Rutherford scattering and (b) Bragg scattering.

For inelastic scattering, the deflected electrons lose energy. The lost energy is normally used to generate other signals for analytical characterization such as characteristic X-rays for energy-dispersive X-ray (EDX) elemental analysis, as shown in Figure 2.7. Here, the incident electrons transfer some of their energy to the electron at the lower energy shell, causing it to be excited to higher energy level and leaving behind a vacant site. Electrons in the higher energy shells then fills the vacancy. The relaxation of ionized state occurs through emission of Auger electron or X-ray. These emissions are characteristic radiations since they reflect the shell energy structure and thus can be used for elemental identification.

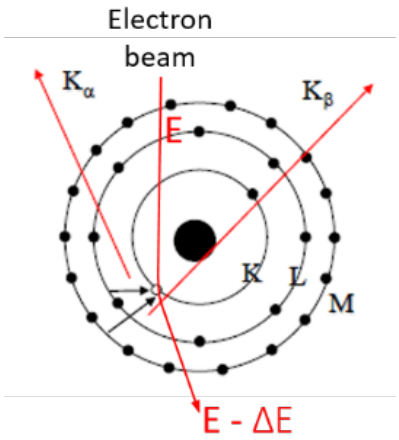

Figure 2.7: Inelastic scattering of electrons generating characteristic X-rays as electrons in higher energy shells fill the vacant site.

2.2.2. Scanning transmission electron microscopy (STEM)

In STEM mode, convergent electron probe is formed by condenser lens and focused on the sample. STEM images are obtained by scanning the electronic probe across the sample. The scattered electrons that passed through the samples are collected by the detector at the bottom and the signals are displayed in greyscale contrast simultaneously for each pixel. It is similar to scanning electron microscopy (SEM). The spatial resolution is basically determined by the size of the convergent electron probe. Typical size is about 0.2 nm, but it has improved better than 0.1 nm by correcting the spherical aberration of the condenser lens. It means the resolution of images could be improved down to sub-angstrom range where atomic columns can be identified clearly. The difference of illumination systems in CTEM and STEM is as shown in Figure 2.8 [12].

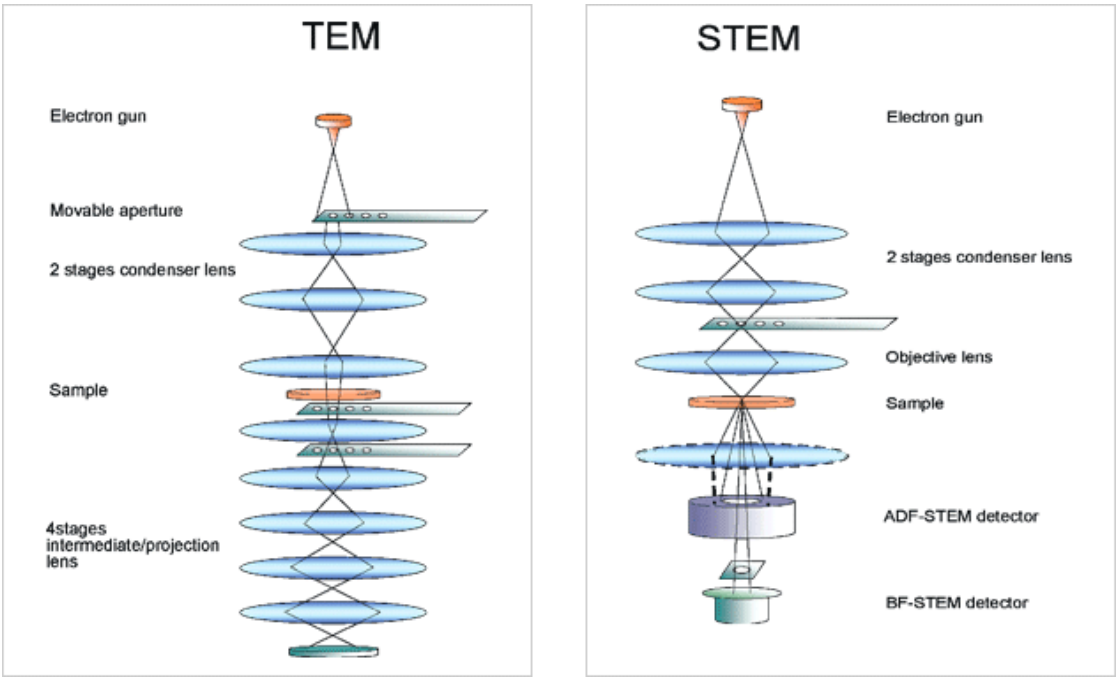

Figure 2.8: TEM and STEM illumination systems [12].

By using a corrector, the forward-scattered electrons are collected as a function of beam location as the electron beam is rastered across the sample. In the end, a virtual image is built in which the signal levels at any location is represented by the grey levels at that corresponding location as shown in Figure 2.9. It is different from the imaging mechanism of TEM image which is formed by interference. Therefore, STEM has some signal lagging issues since image is generated pixel by pixel as it raster scans through the sample.

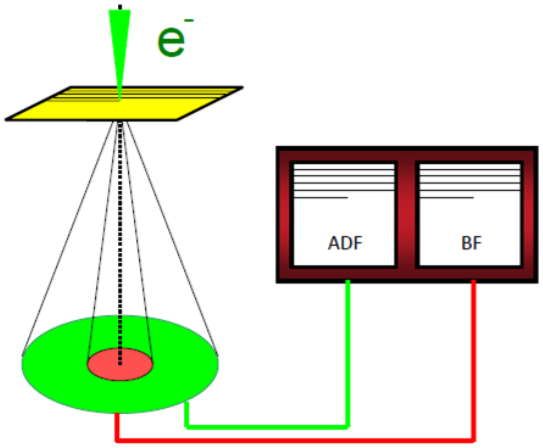

Figure 2.9: Raster scan of the focused electron beam on specimen and recording of different signals onto computer screen sequentially.

2.2.2.1. Imaging modes in STEM

In STEM mode, different geometries of detectors are developed to collect the electrons scattered at different deflection (scattering) angle, as shown in Figure 2.10, thereby giving different imaging modes of ADF, HAADF and BF. Typically, multiple signals could be collected at the same time as long as the TEM system is equipped with the required detectors to enable synchronous monitors.

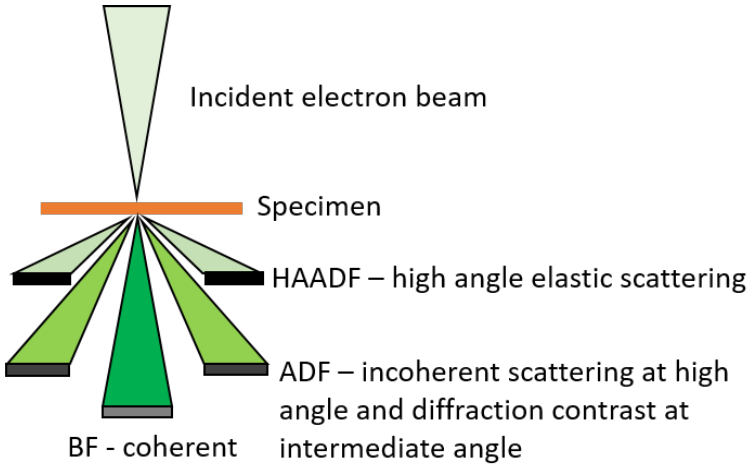

Figure 2.10: STEM detectors and signals collected.

Annular dark-field (ADF) detector collects electrons that are scattered at intermediate angles or high angle. At intermediate angles, by collecting Bragg scattered electrons, a diffraction contrast image is formed, which can show the grain structures of the specimen. ADF detector becomes a high angle annular dark-field (HAADF) detector when the camera length is reduced or the collection distance is nearer to the specimen. The camera length can be adjusted with the projector lenses of TEM. HAADF detector collects Rutherford scattered electrons that are highly sensitive to the change in atomic number *Z*. Incident electrons are scattered at higher angles by atoms with higher atomic number due to stronger electrostatic interactions between the negatively charged electron and positively charged nucleus. So, elements with higher atomic number will appear brighter in the HAADF image, known as *Z* contrast.

Bright field (BF) detector, located at the center of the detector plane, collects electrons scattered at small angles. When incident electrons are illuminated along the crystal zone axis and the sample is composed of heavy element, large number of incident electrons are scattered at higher angle and BF image will appear dark. These images are normally used to complement the ADF images. Another type of BF detector, annular bright field (ABF) detector blocks out signals near the center. The typical collection angle is 12 mrad to 24 mrad. Because of the limited collection angle, it enables the visualization of atomic columns of light atoms. Most of the scattered electrons from light elements are not collected by ABF detector because of their low scattering angle. So, the light elements appear as dark spots. Similarly, scattered electrons from elements with high atomic numbers will not be collected as well in ABF detector and thus ABF allows the simultaneous observation of light and heavy atomic columns with the same contrast [13].

2.2.2.2. Spectroscopies in STEM

As mentioned in Section 2.3.1, inelastic scattering of electrons will generate signals that could be used for elemental characterization. This includes energy dispersive X-ray spectroscopy (EDX) and electron energy loss spectroscopy (EELS).

EDX involves the use of an X-ray spectrometer to detect the characteristic X-rays that are emitted due to relaxation of ionized atoms in samples. It can be used in conjunction with the ADF detector to create elemental mapping and quantification of the observed area in ADF STEM image.

EELS uses an electron spectrometer to measure the energy loss. The data is interpreted in terms of what caused the energy loss. There are three categories of inelastic scatterings that are typically analyzed with EELS. First, inner-shell electron excitations or core excitations (50 to 2000 eV) that are useful for detecting not only elemental information but also chemical bond nature. Second, interband transition due to valence-electron excitation (0 to 10 eV). Third, plasmon excitations due to collective oscillations of free electrons (10 to 50 eV) that contain information about the band structure and dielectric properties of samples.

2.2.3. Transmission electron diffraction (TED)

TED can be used to determine the crystal periodicity and specimen orientation. As a parallel electron beam passes through a thin specimen, the electrons are scattered by the planes of atoms, according to Bragg's Law $n\lambda = 2dsin\theta$ and form spots at the back focal plane of the objective lens. These spots are then projected onto the screen to form the transmission electron diffraction pattern, as shown in Figure 2.11. The array of reflections projected onto the screen contain information about crystal structure, with each reflection representing a certain crystal plane.

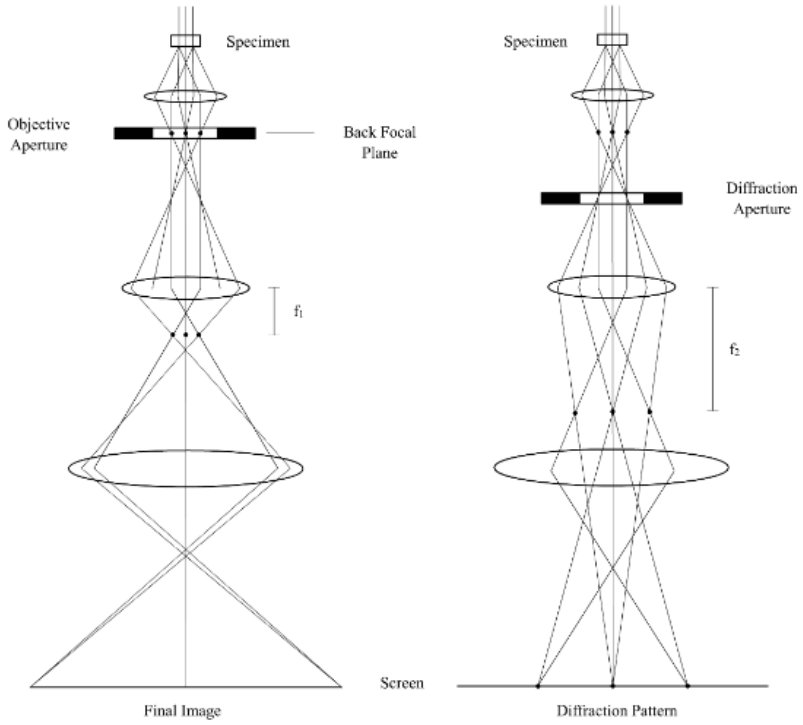

Figure 2.11: Comparison of imaging mode and diffraction mode in CTEM. Adapted from [14].

The subsequent section would give a brief explanation on how diffraction patterns are formed. Diffraction patterns are formed as a result of the intersection of Ewald sphere (1/λ) and the reciprocal lattice points in the reciprocal space. Reciprocal lattice is the Fourier transform of the real space lattice, where the reciprocal lattice point $G = ha^* + kb^* + lc^*$ and a^*, b^* and c^* are the reciprocal lattice vectors. Ewald sphere, where the radius corresponds to the wave number of the incident electrons, is constructed based on the Bragg's Law in reciprocal space, as shown in Figure 2.12 and intersects the reciprocal lattice points at certain positions. Ewald sphere is a locus of all possible scattering vectors when the direction of the incident electron beam is fixed, as indicated by $\boldsymbol{k_0}$. So only reciprocal lattice points that lie on the perimeter of Ewald sphere will appear in the diffraction pattern.

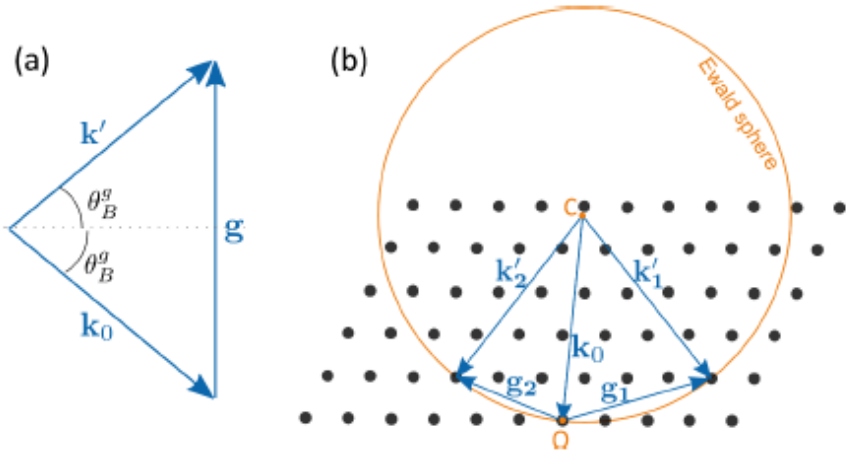

Figure 2.12: (a) Bragg's law in reciprocal space and (b) construction of Ewald sphere based on Bragg's Law.

Since the radius of Ewald sphere is dictated by 1/λ, the small wavelength of electrons means a larger Ewald sphere. Furthermore, the lattice points in the reciprocal lattice of thin samples are elongated along the perpendicular direction to the surface of the thin sample. In this case, even if diffraction deviates slightly from the Bragg condition, many reflections will still appear in the diffraction pattern, as shown in Figure 2.13, and this is one of the advantages of TED as it can provide more information on the crystal structure of the samples.

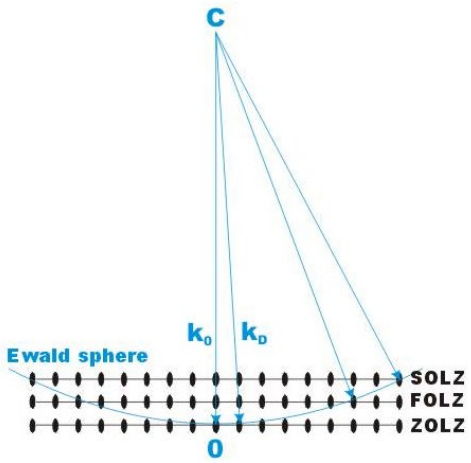

Figure 2.13: Formation of diffraction patterns from the intersection of Ewald sphere and reciprocal lattice points at different Laue zones.

2.3. Magnetism

2.3.1. Origin of magnetism in solids

Magnetism in solid arises from the orbital and spin magnetic moments associated with individual electrons in the material [15], [16]. Since electrons are charged particles, the movement of electrons orbiting around the nucleus could be considered as a current loop and thus will create a small magnetic field, as shown in Figure 2.14.

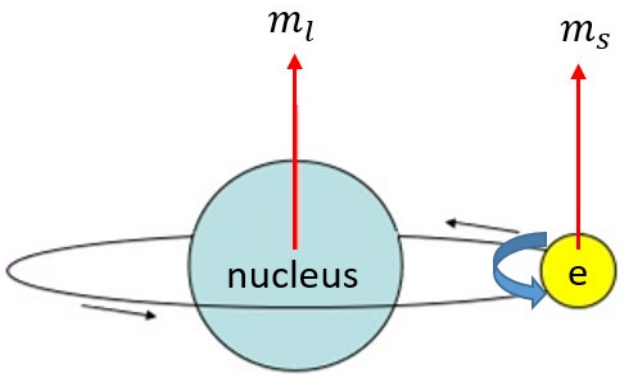

Figure 2.14: Orbital (m_l) and spin (m_s) magnetic moments of a single electron orbiting a nucleus.

If the speed of electron is v, its period of rotation is $\tau = 2\pi r/v$ and so the current generated is $I = -e/\tau$. Thus, the magnetic moment from this current loop is as follow:

$$m_l = I\,A = -\frac{ev}{2\pi r}(\pi r^2) = -\frac{evr}{2}$$

If we rewrite the equation in terms of angular momentum ($l = m_e vr$), where m_e is the mass of electrons, the moment becomes

$$m_l = -\frac{e}{2m_e} l$$

The proportionality factor between magnetic moment and angular momentum, also known as gyromagnetic ratio γ, is then equal to $-\frac{e}{2m_e}$. The negative sign indicates that m_l and *l* are opposite in direction.

And when we consider the orbital magnetic moment in quantized units of Planck's constant ($\frac{nh}{2\pi} = m_e vr$), where *n* is the orbital quantum number and ħ is the Planck's constant, the moment then becomes

$$m_l = \frac{neh}{4\pi m_e}$$

If the electron revolves in the first orbit, then *n* = 1, this orbital magnetic moment is known as the Bohr magneton (μ_B). It is the smallest possible orbital magnetic moment and defined as

$$\mu_B = \frac{eh}{4\pi m_e}$$

$1\mu_B = 9.274 \times 10^{-24}$ Am^2 and subsequent quantized orbital magnetic moments are integrals of this Bohr magneton.

For spin magnetic moment, the magnetic moment is also almost exactly one Bohr magneton. So, the smallest possible magnetic moment due to electron spin has the same definition as follow:

$$m_s = \frac{eh}{4\pi m_e}$$

Electron spins have only two possible quantum states of $+\frac{1}{2}$ or $-\frac{1}{2}$. The spin angular momentum is then given by

$$s = \frac{1}{2}\left(\frac{h}{2\pi}\right) = \frac{h}{4\pi}$$

Putting this expression back into the magnetic moment equation, the spin magnetic moment becomes

$$m_s = -\frac{e}{m_e}s$$

Here, the gyromagnetic ratio, γ is $-\frac{e}{m_e}$, which is twice the γ for orbital magnetic moment. What it means is that spin angular momentum is twice as efficient as orbital angular momentum at creating a magnetic moment. This difference is also known as g-factor. When g = 2, spin contribution arises and when g = 1, orbital contribution arises.

Combining the effects of spin and orbital magnetic moment, the magnetic moment for a single electron orbiting a nucleus is

$$\mu_e = m_l + m_s = -\frac{\mu_B}{\hbar}(l + 2s)$$

where $\hbar = \frac{h}{2\pi}$.

In most cases, two or more electrons contribute to the total magnetic moment of atom. The orbital or spin magnetic moment might cancel each other. For example, a 3d transition metal with 7 valence electrons, the effective magnetic moment would be $3\mu_B$ and not $7\mu_B$, since two electron pairs cancel each other and if a material has all its electron shells filled, the net magnetic moment would be zero, which means it cannot be magnetized. Thus, the net magnetic moment is the sum of magnetic moment of all electrons, taking into the filled states. Mathematically, the total angular momentum *J* for one atom is given by

$$J = L + S$$

where L is the total orbital angular momentum for electrons ($L = l_1 + l_2 + l_3 + \cdots + l_n$) and S is the total spin angular momentum for electrons ($S = s_1 + s_2 + s_3 + \cdots + s_n$). The resultant total magnetic moment of an atom is then as shown below

$$\mu = -\frac{\mu_B}{\hbar}(L + 2S) = -gJ\mu_B$$

where g is the g-factor and given in the equation of $g = \frac{1+J(J+1)+S(S+1)-L(L+1)}{2J(J+1)}$.

Since solids are consisted of large amount of atoms, the total magnetic moment in a solid could then be summarized as the sum of magnetic moment over the entire volume of the solid sample. Mathematically, it is defined as follow:

$$M = \frac{1}{V}\sum_i \mu_i$$

where V is total volume of the solid, i is the number of atoms in the solid and μ_i is the atomic magnetic moment of ith atom.

2.3.2. Types of magnetic materials

When an external magnetic field H is introduced onto the magnetic materials, the response to this field is known as the magnetic flux density or magnetic induction B. In vacuum, B is related to H as

$$B = \mu_0 H$$

where μ_0 is the permeability in free space, which is equal to $4\pi \times 10^{-7}$ Hm^{-1}. If a magnetic material is present in the middle of this magnetic field, the response becomes

$$B = \mu_0(H + M).$$

B and *M* may not be linear functions of *H* depending on the type of material. This is because the material is consisted of different crystal domains having different magnetic moments along the direction of the applied magnetic field. For an isotropic material, the magnetization *M* is proportional to *H* and the ratio of *M/H* is known as magnetic suscepitibility. For non-isotropic materials, the susceptibility may not be a constant.

Thus, depending on the magnetic responses in an applied magnetic field, magnetic materials could be categorized into diamagnetic, paramagnetic, ferromagnetic, antiferromagnetic, ferrimagnetic, spin glass and cluster glass materials. A summary of these types of materials are shown in Figure 2.15. Each of these types of magnetic materials will be briefly explained in the following section.

Type	Magnetic Ordering	Magnetic behavior	M-H curves	Susceptibility curves
Diamagnetism	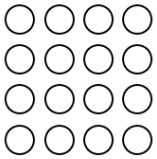	• No net magnetic moment	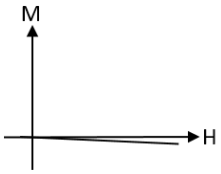	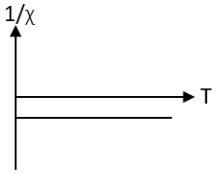
Paramagnetism	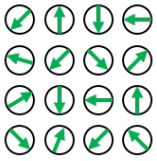	• Permanent magnetic moment • No interaction between neighboring atoms	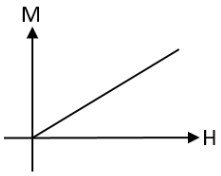	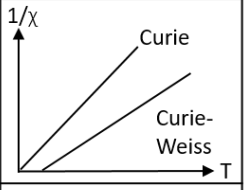
Ferromagnetism		• Permanent magnetic moment • Exchange interactions between atoms produces parallel spin alignment	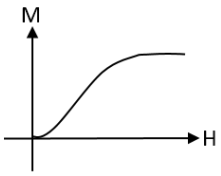	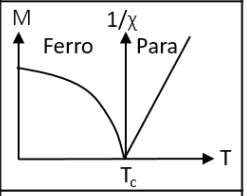
Antiferromagnetism	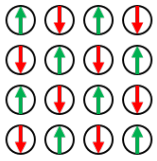	• Permanent magnetic moment • Exchange interactions between atoms produces antiparallel spin alignment	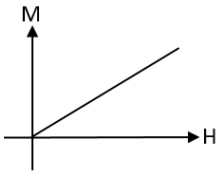	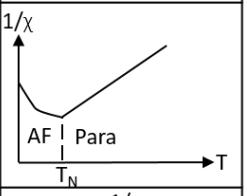
Ferrimagnetism		• Permanent magnetic moment • Exchange interactions between atoms produces unequal antiparallel spin alignment	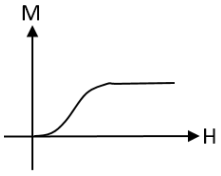	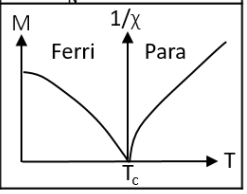

Figure 2.15: A summary of magnetic materials and their typical magnetic behaviors.

2.3.2.1. Diamagnetism

Diamagnetic materials have no net atomic magnetic moment when there is no applied magnetic field because the electron shells are fully filled. However, in an applied magnetic field, a negative magnetization is generated to oppose the applied magnetic field, therefore reducing the flux density within the material. The susceptibility of such materials is independent of temperature.

2.3.2.2. Paramagnetism

In this group of materials, some of the atoms may have net atomic magnetic moments due to unpaired electrons in partially filled shells. The atomic magnetic moments are randomly oriented and are non-interacting when there is no field. These moments will align slightly to the applied magnetic field, creating a low positive magnetization and susceptibility in the same direction as the applied field. However, when temperature is increased, it becomes harder for the atomic magnetic moment to be aligned due to thermal agitation and hence reduce the susceptibility. This behavior is known as the Curie law, with the equation as follow:

$$\chi = \frac{C}{T}$$

where C is a material constant and T is the temperature.

Curie law does not take into considerations the interaction between magnetic moments, which is not the usual case for most materials. The equation is then modified by adding a temperature constant θ using Weiss theory and the susceptibility equation becomes the Curie-Weiss law, and is represented as follow:

$$\chi = \frac{C}{T - \theta}$$

where θ could be positive, negative or zero. When θ is zero, it means that there is no interaction between neighboring magnetic moments and when θ is non-zero, it means that interaction between neighboring magnetic moments exists and the material will only behave like a paramagnetic material above the transition temperature. A positive θ indicates that the material is ferromagnetic below the transition temperature. This θ value corresponds to the Curie temperature T_c. A negative

θ indicates that the material is antiferromagnetic below the transition temperature and this transition temperature is known as the Neel temperature T_N.

2.3.2.3. Ferromagnetism

Ferromagnetic materials have atomic magnetic moments that can strongly interact with each other due to electronic exchange forces. The atomic magnetic moments are all aligned in the same direction, even in the absence of magnetic field. The saturation magnetization is normally used to compare ferromagnetic materials since it can be measured. It is the maximum magnetization that can be obtained under an applied magnetic field at which further increase of applied magnetic field will not cause a change in the magnetization value. When a magnetic field is applied, the material typically shows positive magnetization and susceptibilities since the magnetic moments will be aligned in the same direction in applied field. The susceptibility follows the Curie-Weiss law, but θ is replaced by T_c, as shown in the equation below:

$$\chi = \frac{C}{T - T_c}$$

Curie temperature is another important characteristic of ferromagnetic materials. As explained in the Paramagnetism section, due to thermal agitation, the thermal energy will overcome the exchange interaction of magnetic moments above T_c and cause the magnetic moments to be randomized and exhibit paramagnetic behavior.

In addition, ferromagnets exhibit hysteresis behavior. They can retain some remnant memories of the applied field, thus create a loop structure in the $M - H$ plot. An example of hysteresis curve is as shown below in Figure 2.16, which also shows how the small magnetic domains are affected

by the external magnetic field [17]. As the applied magnetic field is increased from zero, the randomly oriented magnetic domains start to be aligned in the direction of the applied field until all the domains are aligned to reach a saturated state. The magnetization value at this point is known as the saturation magnetization. As the magnetic field is removed, some of the domains are still left partially aligned, thereby leaving a remnant magnetization. A reverse magnetic field is needed to bring all domains back in random directions where magnetization is zero. The magnetic field needed to bring the magnetization back to zero is known as coercivity. As the reverse magnetic field is increased further, it will cause the alignment of magnetic domains in the direction of the reverse magnetic field. The area enclosed in the hysteresis loop indicates whether the magnetic material is soft or hard. A soft ferromagnet would have a smaller area as compared to a hard one. The larger the hysteresis area, the more memory it could retain and thus this kind of materials are normally used as storage devices.

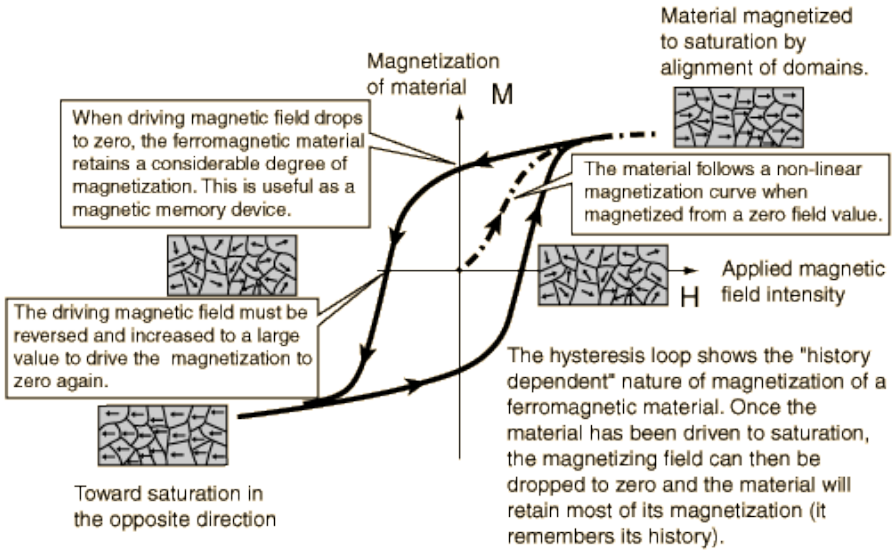

Figure 2.16: Typical hysteresis loop for ferromagnetic materials and the movement of magnetic domains under an applied magnetic field [17].

2.3.2.4. Antiferromagnetism

The atomic magnetic moments in antiferromagnetic materials have strong exchange interactions as well. However, these exchange interactions lead to anti-parallel alignment of moments. So, the magnetic field cancels out and the material appears to have a net magnetic moment of zero, similar to paramagnetic material. Antiferromagnetic materials can also be expressed using the Curie-Weiss law, where the transition temperature becomes the Neel temperature, T_N. Above T_N, the material behaves paramagnetically, and below T_N, susceptibility generally decreases with decreasing temperature.

2.3.2.5. Ferrimagnetism

Ferrimagnetism happens mostly in solids that have two sublattices with different magnetizations. For example, lattice A has a larger positive moment whereas lattice B has a lower negative moment. This results in a lower positive net moment in the solid. The exchange interactions between neighboring atoms in this kind of materials are normally mediated by oxygen anions and thus are more commonly known as indirect or superexchange interaction. Since the interactions result in a net magnetic moment, these materials behave quite similar to ferromagnetic materials, except that it has a lower saturation magnetization. Another difference is that their susceptibility temperature relation does not follow the Curie-Weiss law above T_c. Only at higher temperatures ($T > 2T_c$), the inverse susceptibility would approach linearity.

2.3.2.6. Spin glasses and cluster glasses

In spin glass, the magnetic moments at individual atomic sites appear to be frozen in random directions, as shown in Figure 2.17 [18]. The difference when compared to paramagnetic materials is that in paramagnets, the spin orientations are always fluctuating due to thermal agitation.

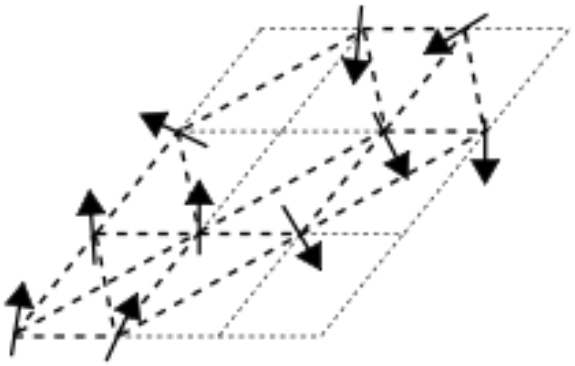

Figure 2.17: Random orientations of frozen spins in spin glasses [18].

This behavior is typically observed in disordered structures such as those with dilute concentrations of magnetic ions in crystalline alloys. It could also occur when the magnetic exchange interactions are frustrated when there are different magnetic states that have equal probabilities of occurrence. For example, the three atoms in an equilateral triangle with antiferromagnetic exchange interactions have three possible orientations of moments with the same energy. Only two out of the three spins can be coupled, leaving the third spin to be frustrated since it cannot determine a unique lowest energy state [19].

Experimentally, spin glass could be identified by the appearance of a cusp in the AC susceptibility measurements, whereby the cusp defines the transition temperature [20]. A zero-field cool (ZFC)/ field cool (FC) bifurcation in the temperature dependence measurements and

plateau of FC curve below the transition temperature [20] are also typical features of spin glass. They display hysteresis effects in magnetization measurements [21] as well.

Cluster glass contains cluster of spins with the same direction, thereby creating small domains which will interact with one another. This is similar to the interactions of single spins in spin glass. The difference between spin glass and cluster glass can be determined experimentally. In the temperature dependence magnetization measurements, cluster glass shows a broad peak as compared to a cusp for spin glass and beyond the spin freezing temperature, it shows a monotonic increase of FC with decreasing temperature while for simple spin glass, the susceptibility will not change much with decreasing temperature after the transition temperature [1].

2.3.3. Exchange Interactions of Magnetic Moments

The magnetic ordering in magnetic materials are known to depend on exchange interaction. Exchange interaction is a quantum mechanical effect that causes the magnetic moments to be aligned in an energetically favorable manner. There are several types of exchange interactions, namely direct exchange, superexchange and RKKY interactions.

2.3.3.1. Direct Exchange

The direct exchange interaction only happens when the magnetic moments are close enough such that their wave functions are overlapped and the corresponding electrons are localized on each atom. The interactions originate from the Coulomb interaction between *d* electrons on

adjacent atoms. It is normally used to explain the magnetism in metals. It can be described by the model of Heisenberg Hamiltonian [22]:

$$H_{ex} = -\sum_{ij} J_{ij} S_i \cdot S_j$$

where J is the exchange integral, S_i and S_j are the spins of atom ith and jth. If J is positive, the interaction is ferromagnetic and if J is negative, the interaction is antiferromagnetic. However, this mechanism cannot be used to explain most magnetically ordered materials. Some materials still display magnetic ordering, even if the distance between adjacent magnetic atoms is large.

2.3.3.2. Superexchange

In superexchange interaction, the magnetic interactions occur between non-neighboring magnetic ions, mediated by the non-magnetic intermediate anions. In this case, it is not necessary for the wave functions to overlap for magnetic interactions but the wave functions of the non-magnetic anions have to overlap with the wave functions of the electrons that are responsible for magnetism. The electron spins align with each other through the hybridization of anions with *p*-electron orbitals.

2.3.3.3. RKKY

Ruderman-Kittel-Kasuya-Yosida (RKKY) interaction describes the magnetic exchange between magnetic moments, mediated by mobile conduction electrons. A localized magnetic moment spin-polarizes the mobile conduction electrons and these conduction electrons then interact with

localized magnetic moment that could be adjacent or further away from the first localized magnetic moment. So, this interaction is long-range and exhibits oscillatory dependence on the distance between magnetic moments. This exchange interaction is the dominant interaction in metals.

CHAPTER 3

STEM Structural Analysis of Fe_xTiS_2

3.1. Introduction

As mentioned in Chapter 1, the properties exhibited by the Fe_xTiS_2 crystals are dependent on the Fe concentrations and the arrangement of guest atoms. Thus, it is important to study Fe ordering at different concentrations. There have been several structural studies performed. However, until now, there is still some controversy regarding the atomic structures of Fe_xTiS_2, especially at low Fe concentrations. X-ray studies of Fe_xTiS_2 revealed short-range ordering of $2a \times 2a \times 2c$ at x = 0.15, formation of $2\sqrt{3}a \times 2a \times 2c$ or $2a \times 2a \times 2c$ Fe ordering for x = 0.25 and $\sqrt{3}a \times \sqrt{3}a \times 2c$ Fe ordering for x = 0.33, where a and c are the lattice parameters of TiS_2 [4]. However, Rietveld refinement of the XRD results showed that the Fe atoms might not be perfectly ordered since the Fe occupancy at each site did not equal to one. These results were supported by Monte Carlo simulations that indicated that the interactions of Fe atoms within the layers must be repulsive and the interactions of Fe atoms between the layers must be attractive [23]. However, subsequent studies by other groups showed contradictory results. Gu et al. deduced 10 possible stable superstructures of intercalated TMD materials at different Fe concentrations in Fe_xTiS_2, where the 10 superstructures were consisted of $2a \times 2a \times 2c$ at x = 0.125, $\sqrt{3}a \times \sqrt{3}a \times 2c$ at x = 0.17, $2a \times 2a \times c$ or $\sqrt{3}a \times a \times 2c$ at x = 0.25, $\sqrt{3}a \times \sqrt{3}a \times c$ at x = 0.33 and 5 other superstructures consisting of different combinations of $\sqrt{3}a$ and $2a$ at x = 0.50. Their calculations were also based on the interaction potential of Fe atoms but using concentration wave theory in reciprocal space [24]. In addition, recent studies using TED and STEM imaging had shown different Fe ordering as well at the same concentrations. Choe et al. used electron diffraction and reported the finding

of only $\sqrt{3}a \times \sqrt{3}a$ superstructures in 1T- Fe_xTiS_2 for $0.086 \leq x \leq 0.703$ [5]. In contrast, Pawula et al. found inter-grown regions of $2a \times 2a$ and random Fe distribution, as well as planar defects for $0 \leq x \leq 0.20$ by scanning transmission electron microscopy (STEM) observation of the cross section [25].

So, in this study, the main aim was to combine both TED and STEM imaging to clarify the arrangement of Fe atoms in Fe_xTiS_2, especially at low Fe concentrations ($x \leq 0.20$) since there is still no consensus on the arrangement of Fe atoms at low concentrations. XRD and TED methods are convenient to identify periodic structures. At low Fe concentrations, short range Fe ordering may exist, and is expected to be identified by spherical aberration-corrected STEM imaging, which provides atomically resolved structure information. Both TED and STEM complement each other in the analysis of 2D materials.

3.2. Methodology

3.2.1. Synthesis of Fe_xTiS_2 single crystals

Fe_xTiS_2 single crystals at concentrations of x = 0, 0.05, 0.10, 0.15, 0.20, 0.25 and 0.33 were grown using chemical vapor transport method with iodine as transport agent. The amount of raw materials were calculated based on the assumption of Ti + S = 2g, following the work by Mizuta [26]. The details of the raw materials used are as shown in Table 3.1 and the amount of powder used for each specimen is listed in Table 3.2.

Table 3.1: Details of the raw materials used.

Chemical name	Manufacturer	Lot No.	Purity (%)
I_2	Wako Pure Chemical Corporation	096-03122	99.9
S	Kojundo Chemical Laboratory Co. Ltd.	293821	99.99
Ti	Soekawa Riken Co. Ltd.	34739A	99.99
Fe	Rare Metallic Co. Ltd.	90209-63-71	99.99

Table 3.2: Amount of powder used for each specimen.

Composition, x	Fe (mg)	Ti (mg)	S (mg)	I_2 (mg)
0.00	0	85.485	1145.21	72.66
0.05	49.88	854.80	1145.47	72.50
0.10	99.84	855.25	1145.51	77.73
0.15	149.91	855.02	1147.10	81.64
0.20	199.98	855.51	1145.49	75.37
0.25	249.83	855.26	1145.01	81.75
0.33	329.08	854.91	1145.90	87.89

The raw materials were introduced into quartz tubes in the order of I_2, S, Ti and Fe according to their sublimation temperature. Species with low sublimation temperatures (I_2 and S) are placed at the bottom of the quartz tube so that they are further away from the heat produced during the quartz tube sealing process. The quartz tube was then vacuumed down to a pressure of approximately 10^{-5} Pa before being sealed with an acetylene torch. To avoid the raw material from sublimating, the bottom parts of the quart tubes were wrapped with wet tissue and immersed in liquid nitrogen for a few minutes to ensure that the raw materials were kept at low temperatures

and would not sublimate during the high temperature sealing process. The sealed quartz tubes were then placed 13.5 cm from the right end of the tube furnace, so that the higher temperature end was at 950°C and the lower temperature end at 920°C, as shown in Figure 3.1(a). Two quartz tubes were placed side by side each run. The heating profile set for the tube furnace is as shown in Figure 3.1(b). A lower heating rate was applied for these specimens to avoid sudden rise of vapor pressure in the quartz tubes that could lead to explosions. They were then left at 950°C for one week before being left to cool down.

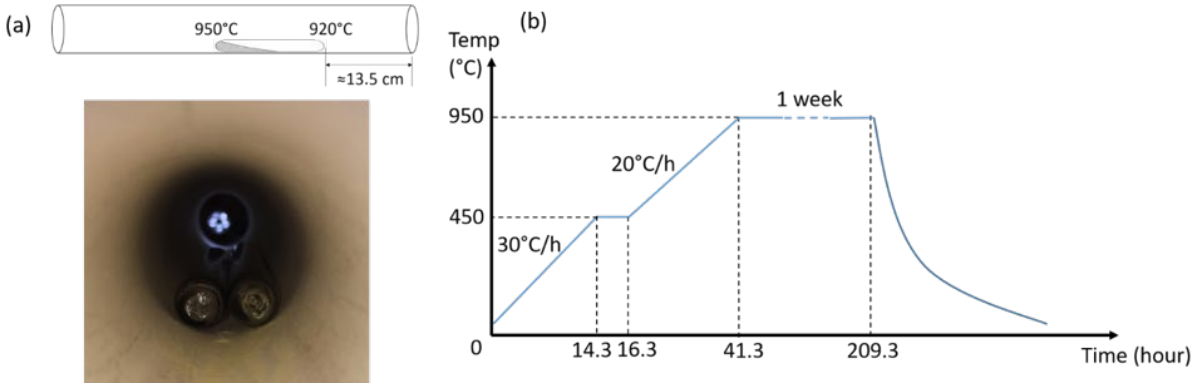

Figure 3.1(a): Setup of the quartz tubes inside the tube furnace. The quartz tubes were put at a distance of approximately 13.5 cm from the right side of the tube furnace, so that the powder region of the quartz tube was at the higher temperature end of 950°C and the crystal growth region was at the lower temperature end of 920°C. Photo shows the position of two quartz tubes placed in the furnace. (b) Heating profile for the quartz tubes in the tube furnace.

3.2.2. XRD Characterization

Powder X-ray diffraction (XRD) characterization was performed using Rigaku Smartlab Fully Automated Modular XRD system to confirm the structures of the specimens. The fine fragments of the specimens were ground in agate mortar to ensure random crystal orientation was achieved

for each specimen. The X-ray source used was Cu-Kα (λ = 1.54059 Å) and two scanning ranges were used, 0° to 10° at a step size of 0.2°/min and 10° to 120° at a step size of 2°/min.

3.2.3. STEM Characterization

Since the specimens grown here were large in size, one piece of specimen could be used to prepare both the plan view and cross sectional view specimens for TEM observation, as shown in Figure 3.2. The plan view specimens were prepared by breaking parts of the specimen using tweezers and ultrasonicating in ethanol before dripping a few drops of the solution onto a 7 nm thick carbon-coated copper grid. Whereas the two cross-sectional view specimens (along and perpendicular to the hexagonal edges of the crystal flake) were prepared using a focused ion beam (FIB).

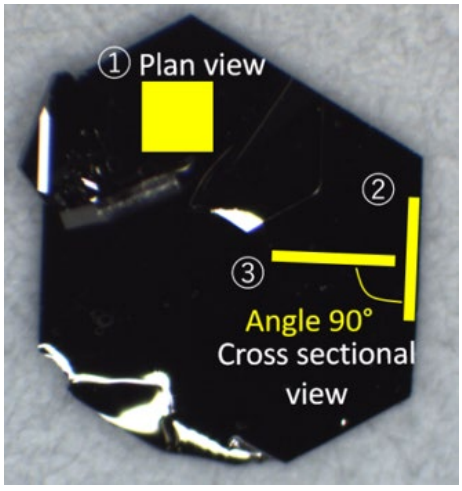

Figure 3.2: Photograph of the hexagonal-shaped Fe_xTiS_2 samples grown by the chemical vapor transport technique. Three TEM samples were prepared from each piece of crystal to observe the plan view and two cross-sectional views.

STEM images were acquired with a spherical aberration-corrected TEM (JEOL JEM ARM200F) operated at 120 kV. An accelerating voltage of 120 kV was used here because Fe_xTiS_2 was found to be highly sensitive to electron beam. Specimens suffered from beam damage at 200 kV and this was even more apparent in STEM mode due to converged electron beam. The high dose of electron beam focused on the observation region caused the ordering of Fe atoms to be disrupted. ABF images were obtained with inner and outer collection angles of 12 mrad to 24 mrad, respectively.

The thickness of each observation area was determined from low-loss EELS spectra using log-ratio method [11], [27], as shown in the equation below:

$$\frac{t}{\lambda} = \ln\left(\frac{I_t}{I_0}\right)$$

where λ is the total mean free path for all inelastic scattering, I_t is the area under the whole spectrum corresponding to the total number of transmitted electrons and I_0 is the area under zero-loss peak corresponding to the number of elastically-scattered electrons. This equation indicates the number of elastically-scattered electrons reduced exponentially with increasing thickness. The total mean free path or effective mean free path, taking into considerations the collection angles, could be determined using the equation by Iakoubovskii et al. [28], as shown below:

$$\lambda = \frac{200FE_0}{11\rho^{0.3}} / \ln\left\{\frac{\alpha^2 + \beta^2 + 2{\theta_E}^2 + \delta^2}{\alpha^2 + \beta^2 + 2{\theta_C}^2 + \delta^2} \times \frac{{\theta_C}^2}{{\theta_E}^2}\right\}$$

where E_0 is the incident energy. α is the incident convergence semi-angle, which in this setup, is equal to 37 mrad. β is the collection semi-angle, which in this system is equal to 25 mrad at an aperture size of 5 mm. ρ is the density of specimen in g/cm^3. For TiS_2, the density is equal to 3.22

g/cm^3. θ_E is the characteristic angle, defined as $\theta_E = 5.5\rho^{0.3}/(FE_0)$. θ_c is equal to 20 mrad and $\delta^2 = |\alpha^2 - \beta^2|$. The relativistic factor, F is defined as

$$F = \frac{1 + E_0/1022\ keV}{(1 + E_0/511\ keV)^2}$$

Replacing all the known parameters into the equation, the effective mean free path was found to be 107.3 nm.

EDX mapping was performed on each sample after taking STEM images to confirm the compositions of that specimen. A dwell time of 0.1 ms/pixel and a total sweep count of 50 were used during the mapping process.

3.2.4. STEM Simulation

STEM simulations were performed using HREM^{TM} software. The simulations were based on the multislice approach to recreate the ABF images under the same STEM operating conditions, as well as specimen thickness. The simulations were conducted using the parameters of Cs = 0.001 mm, C_5 = 0 mm, as well as inner and outer annular detector angles of 12 mrad and 24 mrad to emulate the ABF detecting system. In the calculation, the reciprocal-space resolution was 0.20 nm^{-1} and the cut-off scattering vector (= sin θ_B/λ) was set at 20 nm^{-1} (scattering angle of 142 mrad). The absorptive potential approximation was also taken into consideration using the Weikenmeier-Kohl scattering factor. The atomic displacement parameters of Ti, S and Fe atoms used for the simulations were 6.5074 × 10^{-4} nm^2, 5.041 × 10^{-5} nm^2 and 7.0634 × 10^{-3} nm^2, respectively [29].

3.3. Results and Discussion

3.3.1. Photographic Images of the Fe_xTiS_2 Crystals

Figure 3.3 shows the photographic images of Fe_xTiS_2 at different concentrations. At low concentrations (x = 0.05, 0.1 and 0.15), the product consisted of mainly powder form with few pieces of hexagonal flakes with diameters of approximately 1 mm to 2 mm. As the concentration increased ($x \geq 0.20$), the size of the hexagonal flakes increased. Average sizes of the hexagonal flakes at higher concentrations ($x \geq 0.20$) were in the range of 2 mm to 4 mm. This suggested that the binding forces between the elements in Fe_xTiS_2 were weaker at low concentration (x = 0.05, 0.1 and 0.15) than at high concentration ($x \geq 0.20$).

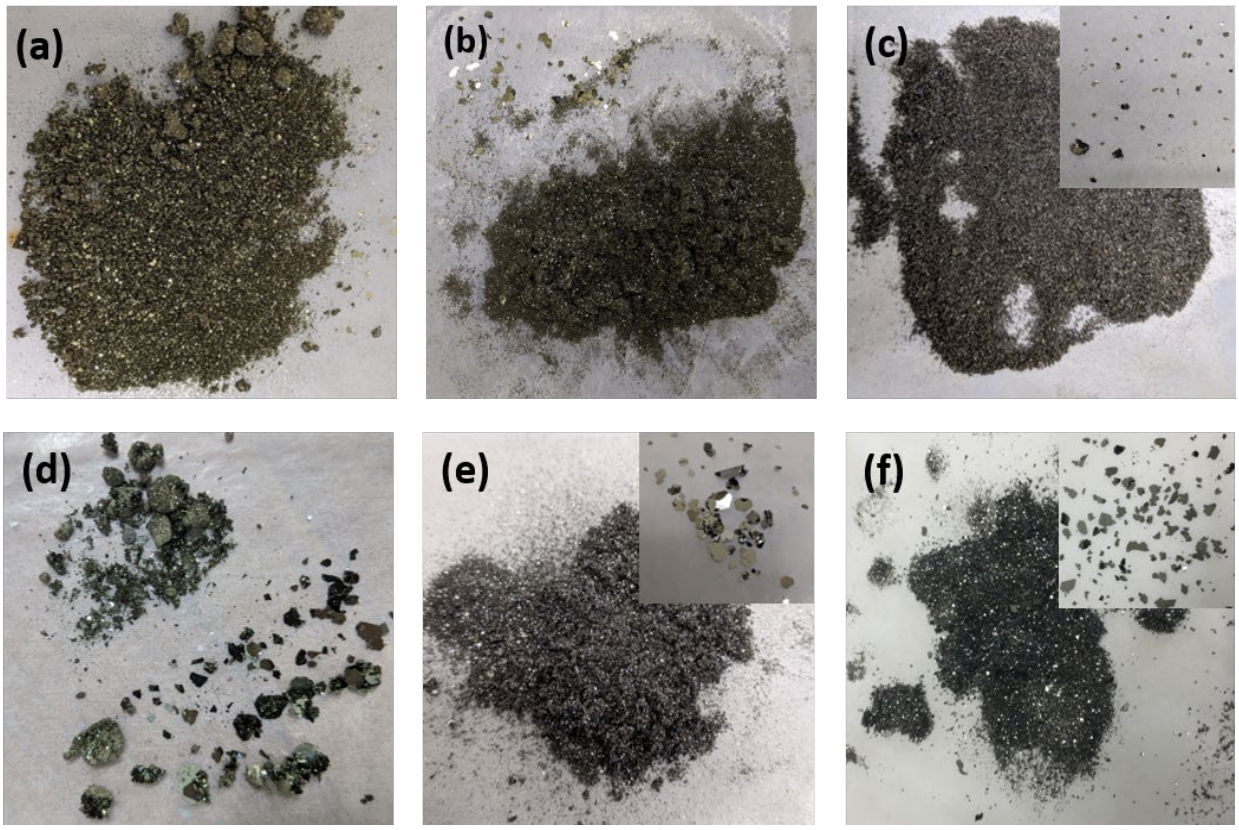

Figure 3.3: XRD spectrum at the scanning range of 10° to 120° for FexTiS2 ($0 \leq x \leq 0.33$).

3.3.2. XRD Structural Analysis

Figure 3.4 shows the XRD spectrums from the scanning range of 10° to 120° for Fe_xTiS_2 at Fe concentrations of x = 0, 0.05, 0.10, 0.15, 0.20, 0.25 and 0.33. All peaks matched the host structure TiS_2 and no superstructure peaks could be identified. It could be seen that [*00l*] peaks were dominant. This was normal since the crystals were consisted of hexagonal flakes. Specimens would have preferentially oriented in the [*00l*] directions, even though the specimens were ground with agate mortar. Thus, even weak reflections such as [*005*] peaks could still be detected.

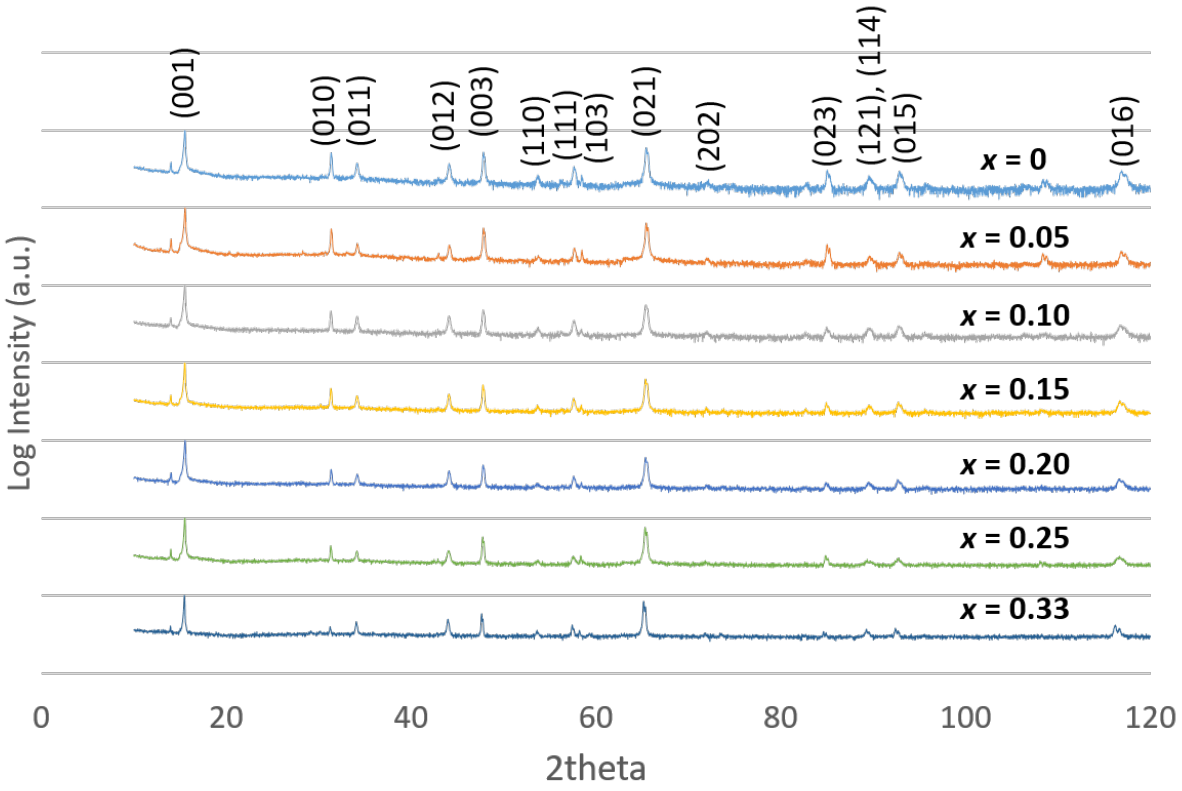

Figure 3.4: XRD spectrum at the scanning range of 10° to 120° for Fe_xTiS_2 ($0 \leq x \leq 0.33$).

A XRD scan at low scanning range of 0° to 10° was also performed to check the periodicity along the *c*-axis. [001] peak was observed at approximately 15.6° in the high scanning range from

10° to 120°. If 2*c* ordering existed along the *c*-axis, then a peak should appear at approximately 7°. However, no peaks could be detected at the low scanning range, as shown in Figure 3.5. One possible reason as to why no superstructure peaks were detected in the XRD spectrum might be due to limited minimum wavelength and intensity of the X-ray source. So the effective maximum dynamic range of weak vs strong reflections is limited, which means that weak superstructure reflections might be not be in the detectable range. In previous structural studies of Fe_xTiS_2, the X-ray source used was synchrotron with a higher brilliance and energy, which allows a deeper penetration into the sample and thus reduces surface effects.

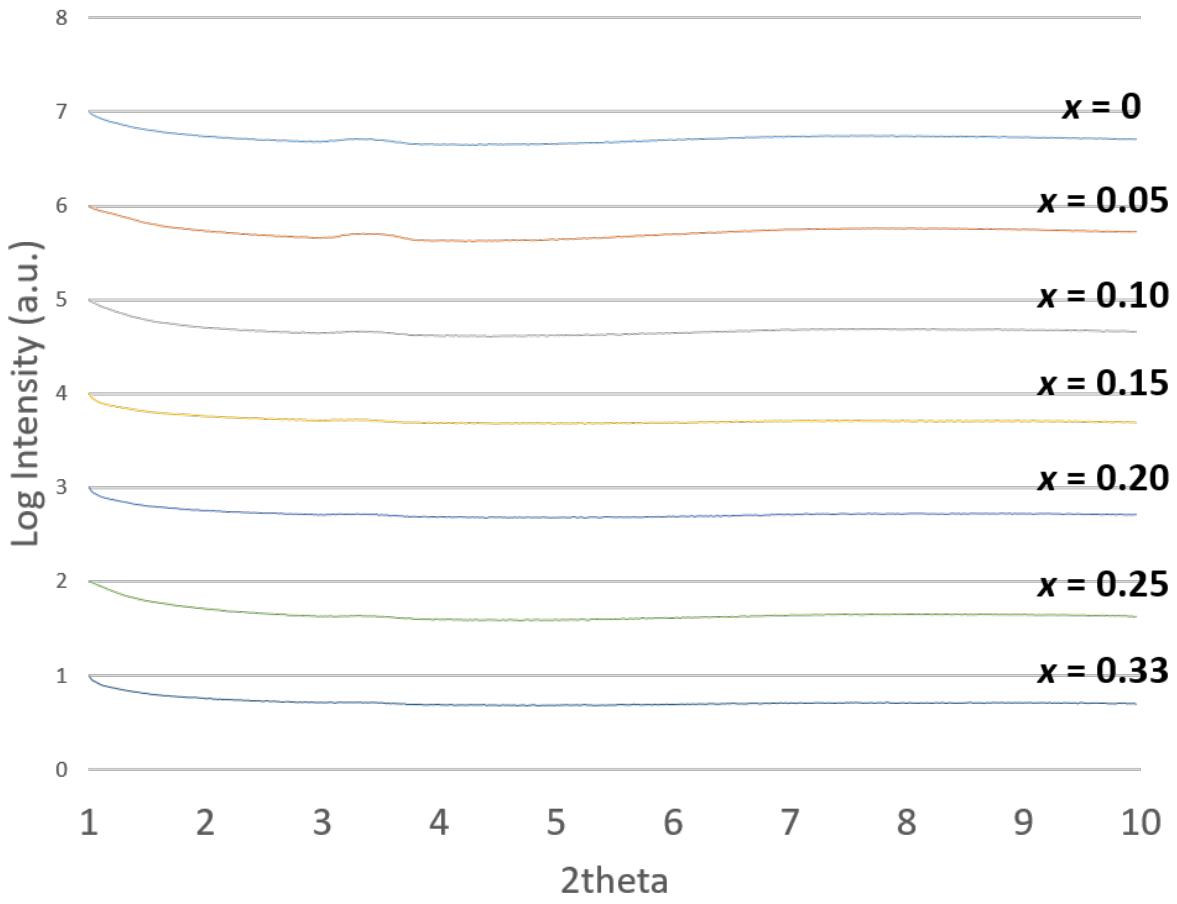

Figure 3.5: XRD spectrums from the scanning range of 0° to 10° for Fe_xTiS_2 ($0 \leq x \leq 0.33$) at different Fe concentrations.

The lattice parameters of each specimen was estimated using CellCalc software using TiS_2 as the reference basis. The lattice parameters of TiS_2 were obtained from crystallographic database with a = 3.397 Å and c = 5.691 Å [30]. Figure 3.6 shows the composition dependence of lattice parameters a and c. A slight expansion of the structure in both a and c could be observed when the Fe content was increased, as indicated by the percentage of increment. The slight expansion matched previous reports stating that introduction of guest atoms in the van der Waals gaps would cause a slight expansion of the lattice [9]. When Fe atoms are introduced into the gaps, they formed bonding with the surrounding S atoms. The Fe-S bonds caused a readjustment of the gap distance and in the end expanded the structure slightly along the c-axis. Thus, when more Fe atoms were added at higher concentrations, more Fe-S bonds were formed, which in turn increased the gap distance further.

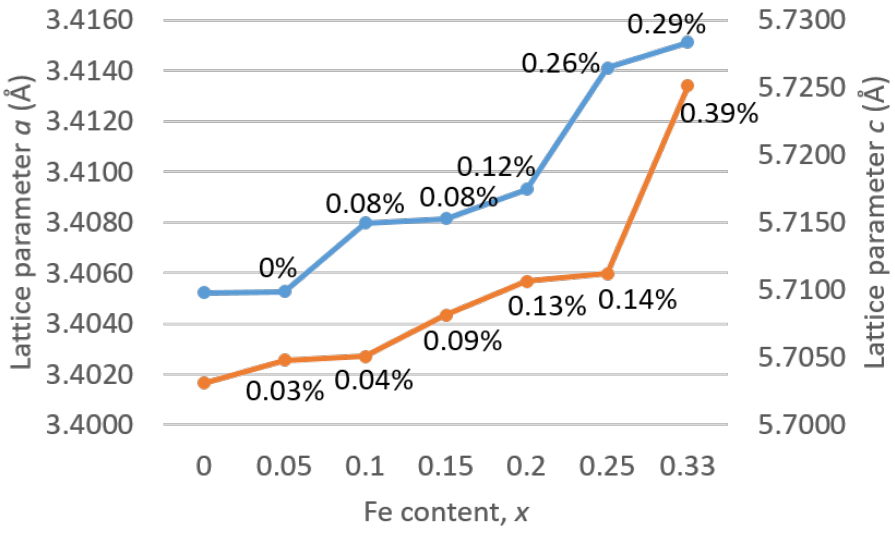

Figure 3.6: Composition dependence of lattice parameters a and c for Fe_xTiS_2 ($0 \leq x \leq 0.33$). Blue line indicates the lattice parameter a and orange line indicates the lattice parameter c.

3.3.3. TEM Structural Analysis of Fe_xTiS_2

3.3.3.1. $x = 0$ (TiS_2)

The $x = 0$ specimen was prepared for reference purposes. Figure 3.7(a) shows the TED pattern and ABF image at [001] zone axis. The TED pattern obtained at the region of a single crystalline phase showed a hexagonal reciprocal lattice pattern. In the ABF image (Figure 3.7(b)), the spots with darker contrast correspond to the Ti atomic columns due to heavier element whereas the spots with light contrast correspond to the S atomic columns, as indicated by the blue and yellow circles. The Ti and S atomic columns formed hexagonal structures as shown in the inset of Fig. 3.7(b). It is also important to note that the contrast of every Ti atomic column in the image appeared consistent.

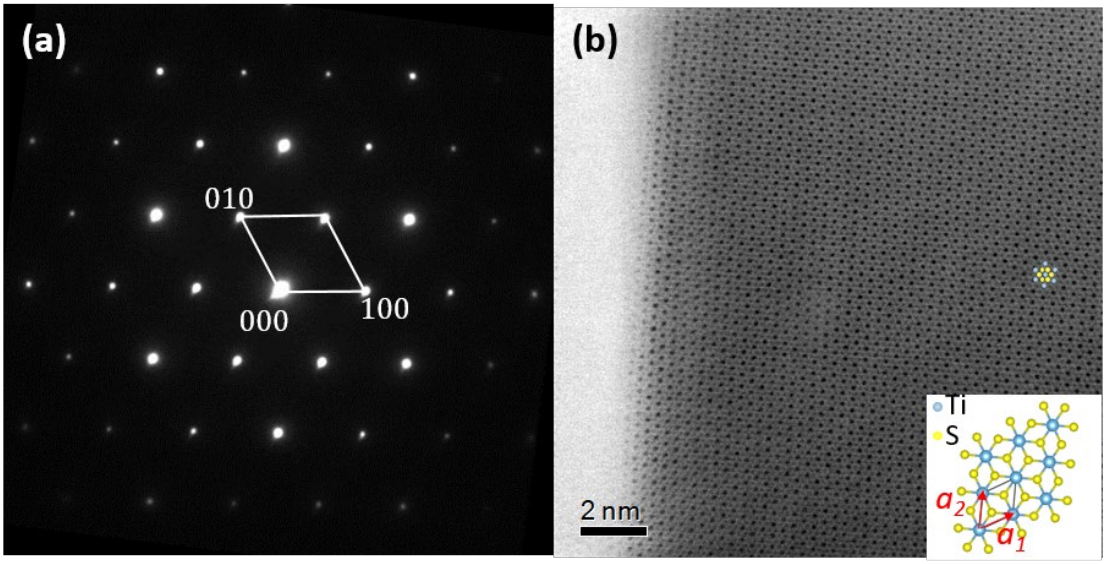

Figure 3.7: (a) TED pattern showing only fundamental reflections of TiS_2 and (b) ABF image of TiS_2 in the [001] zone axis, which shows the hexagonal atomic structure. The inset shows the structural model of TiS_2 crystal.

EDS mapping in Figure 3.8 shows that the single crystals grown had uniform distribution of Ti and S, with Ti:S ratio equal to 0.5, matching the TiS_2 structure.

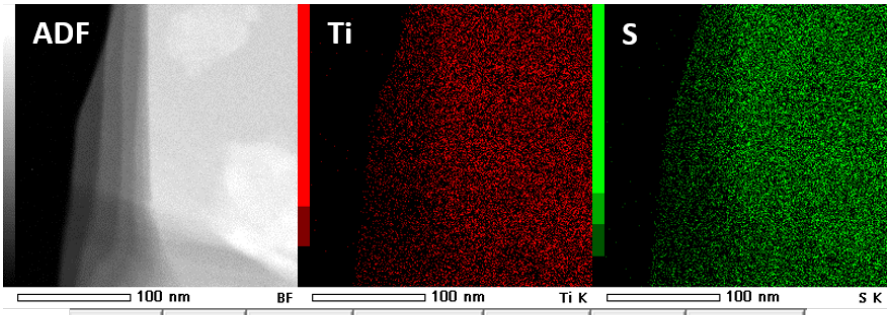

Ele...	Cl...	(keV)	Counts	Mass%	Sigma	Atom%
S K	Ref.	2.307	39136.45	57.22	0.38	66.63
Ti K		4.508	24118.81	42.78	0.38	33.37
Total				100.00		100.00

Figure 3.8: EDS mapping of TiS_2.

3.3.3.2. $x = 0.05$

Figure 3.9 shows the TED pattern and ABF image for $x = 0.05$ in the [001] zone axis. The TED shows only fundamental reflections of host TiS_2 structure, suggesting the concentration of Fe was too low to cause any long-range periodicity in the host structure. Whereas for the ABF images, different contrasts were observed at the Ti atomic sites especially in the thinner region (the left region in ABF image of Fig. 3.9(b)). Since Fe atoms have been reported to preferentially occupy the same sites as Ti atomic columns in the van der Waals gap (between two neighboring TiS_2 layers), the darker contrasts at Ti atomic sites suggest the possibility of Fe intercalation along the corresponding atomic columns. The intensity of the atomic column is almost proportional to the numbers of Ti and Fe atoms at the Ti atomic columns in the ABF image, when the sample is thin enough. Therefore, the distribution of Fe atoms can be identified in the van der Waals gap when the thickness is double TiS_2 layers. If the thickness is triple TiS_2 layers, Fe atoms existing in the two van der Waals gaps can be identified but it is not possible to identify which gap the Fe atoms

occupy. When the specimen is thick, the intensity is no longer proportional to the numbers of Ti and Fe atoms because of the multiple scattering effect. To identify the Fe distribution in the van der Waals gap, thickness of double TiS_2 layers is required.

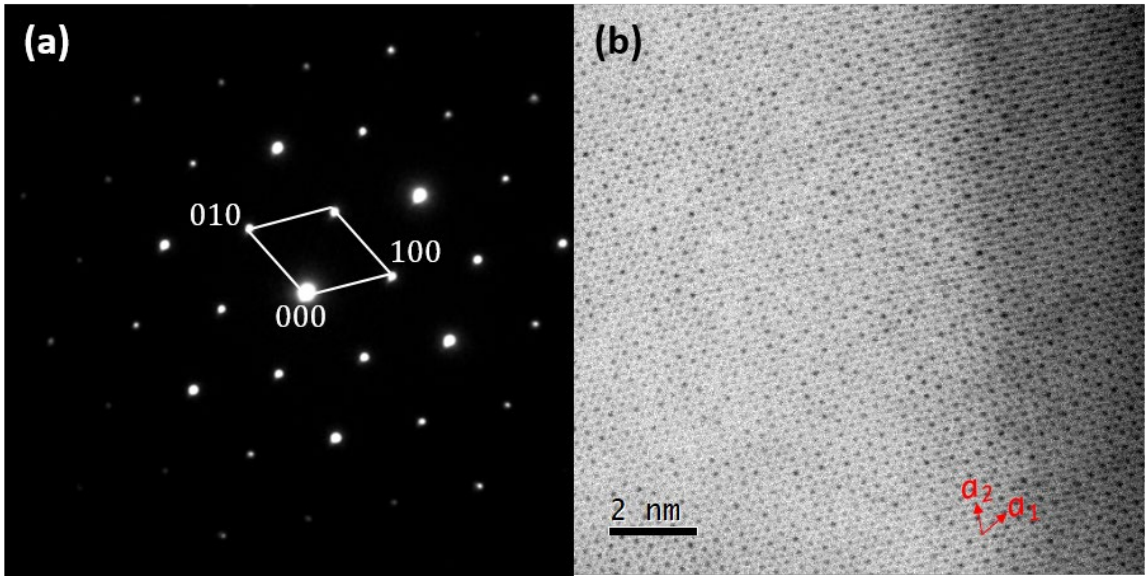

Figure 3.9: (a) TED pattern and (b) ABF image for $x = 0.05$ in the [001] zone axis. White diamond in the TED pattern indicates the reciprocal unit cell. Red arrows in the ABF image indicate the two basic lattice vectors.

The relative thickness was measured by EELS in the rectangle region that included the observation area (Figure 3.10(a)). The profile of the relative thickness was obtained by averaging along the short side of the rectangle region (Figure 3.10(b)). The relative thickness of the observation area corresponds to the range between two dashed lines in the profile of Fig. 3.10(b) and its thickness was estimated to be about 0.65 nm, which was slightly larger than the lattice parameter of TiS_2 along the *c*-axis (0.5691 nm) [30]. So, in this region, there was only one van der Waals gap in which the intercalated Fe atoms could occupy.

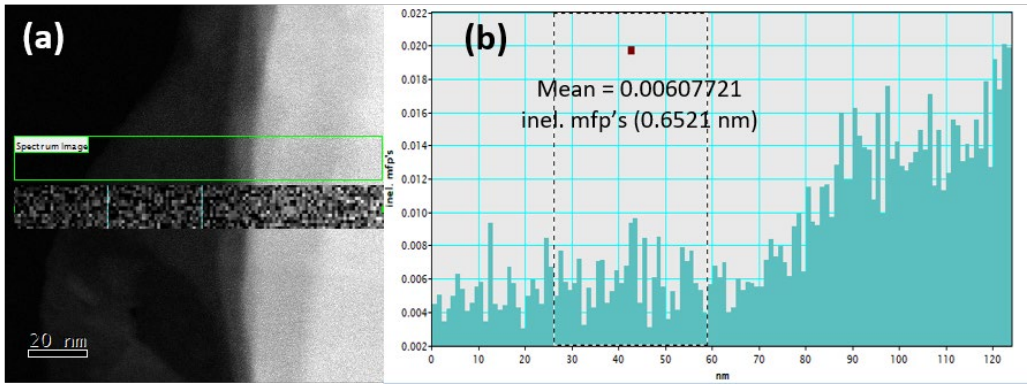

Figure 3.10: (a) Low magnification ADF image. EELS signals were obtained at each pixel in the green rectangle region for thickness measurement. (b) Relative thickness profile obtained by averaging along the short side of the rectangle region for $x = 0.05$.

Since there was only a layer of van der Waals gap in this region, the in-plane distribution of Fe atoms could be determined directly in this region. Figure 3.11(a) shows the analysis area, where the blue triangles indicate the Ti sites and red circles indicate the possible intercalated Fe sites due to the darker contrast. In this plot, there are 55 Fe and 1197 Ti sites. The Fe:Ti ratio, which equal to 0.046, matched well the nominal growth concentration of $x = 0.05$. Using this Fe distribution plot, the atomic correlations between the Fe atoms were then determined using radial distribution function. From the radial distribution plot in Figure 3.11(b), the 3 peaks were identified at atomic distances of 0.33 nm, 0.61 nm and 0.69 nm, corresponding to the bond distances of a, $\sqrt{3}a$ and $2a$, respectively. $\sqrt{3}a$ and $2a$ are the typical separation distances reported for Fe atoms in Fe_xTiS_2 at higher concentrations. Among these three peaks, Fe atoms at a distance of a have the highest intensity, suggesting that some Fe atoms might aggregate to form clusters. The peak intensity for $\sqrt{3}a$ ordering was observed to be higher than that of $2a$ ordering, with a $\sqrt{3}a$: $2a$ ratio of 2.36. Considering that Fe atomic pairs at distances of a would also contribute to the $2a$ peak intensity, the $\sqrt{3}a$ bonding appeared to be more dominant at low concentrations of Fe atoms. This result

differs from the previous report by Choe et al.[5], where clusters of 2*a* Fe atomic pairs were reported.

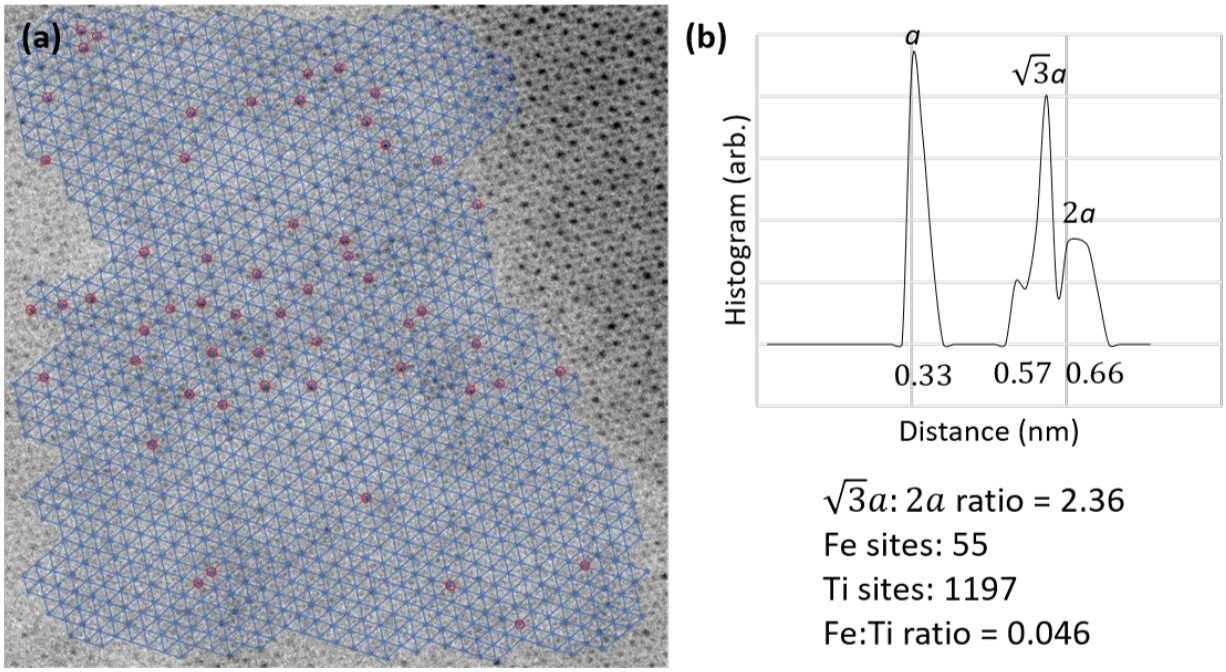

Figure 3.11: (a) Distribution of Fe atoms at the observation area and (b) Radial distribution plot of intercalated Fe atoms for $x = 0.05$.

EDS mapping in Figure 3.12 further confirm that the Fe atoms were uniformly distributed in the specimen and the atomic ratio Fe:Ti of 0.06, matched well the intended growth concentration.

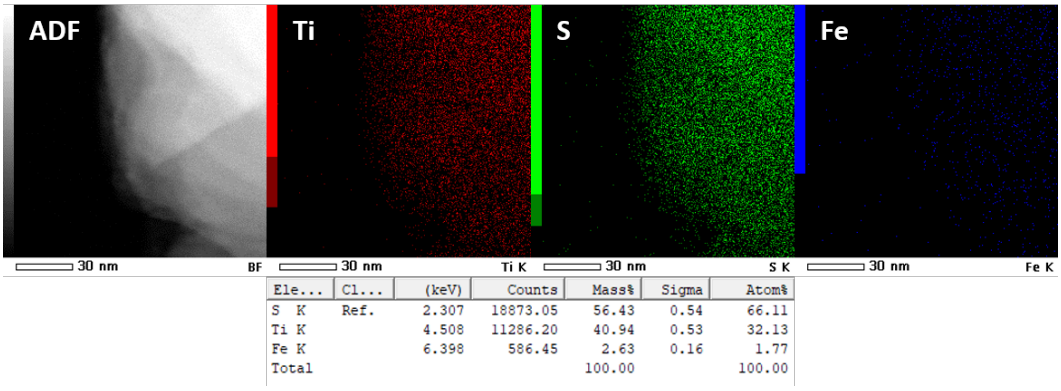

Ele...	Cl...	(keV)	Counts	Mass%	Sigma	Atom%
S K	Ref.	2.307	18873.05	56.43	0.54	66.11
Ti K		4.508	11286.20	40.94	0.53	32.13
Fe K		6.398	586.45	2.63	0.16	1.77
Total				100.00		100.00

Figure 3.12: EDS mapping of the $x = 0.05$ specimen.

Figure 3.13 shows the cross-sectional TED patterns and ABF images. The two TED patterns in (a) and (b) were identified to be in the [010] and $[\bar{1}20]$ zone axes. The rectangles in the TED shows the basic unit in reciprocal space and the corresponding planes. The ABF image viewing from [010] direction shows that the S-Ti-S layers are arranged in tilted arrangement, as shown in the inset, with the presence of van der Waals gaps in between. Whereas, the ABF image viewing from $[\bar{1}20]$ direction shows that the S-Ti-S layers are arranged vertically, separated by the van der Waals gaps, as indicated in the inset. In these van der Waals gaps, some faint contrast could be observed. These spots, indicated by orange arrows, seem to correspond to intercalated Fe atoms. No specific ordering could be observed for the Fe atoms, even though Fe atoms appear only with faint contrasts in both ABF images of Fig. 3.13(c) and (d). Because Fe atoms were not intercalated in every site along the atomic columns due to low concentrations, whereas Ti and S atoms occupied every site in these atomic columns, respectively. Thus, the contrast of the Fe atomic column was much lower than one of Ti or S atomic columns, especially when the sample was relatively thick (about 10 nm). The samples could not be thinned down further since it experienced damage during the thinning process. For example, the TiS_2 layers sometimes became distorted as shown in the upper region of Figure 3.13(d).

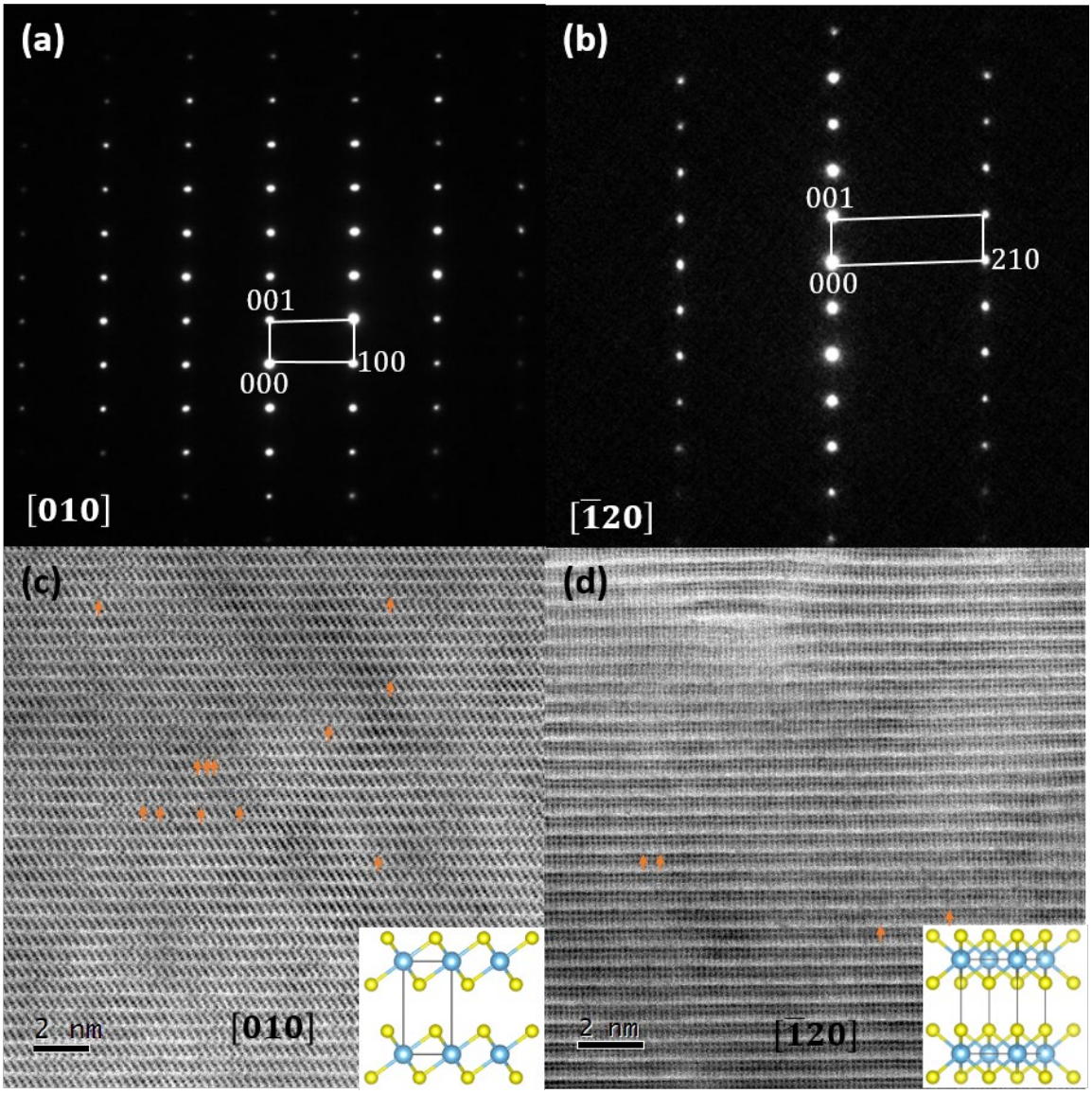

Figure 3.13: TED patterns obtained from the directions of (a) [010] and (b) [$\bar{1}$20]. (c) and (d) show the corresponding ABF images.

3.3.3.3. $x = 0.10$

Figure 3.14 shows the TED pattern and ABF image at x = 0.10 viewed from the [001] zone axis. The TED shows only fundamental reflections of host TiS_2 structure, similar to TiS_2. It indicates no long range ordering of Fe atoms for x=0.10. Similar to x = 0.05, darker contrast at

some of the Ti sites at the thin region corresponded to the intercalation of Fe atoms(at the bottom half in the ABF image of Figure 3.14(b)). The thickness at this region was estimated to be 0.69 nm by EELS thickness measurement, as shown in Figure 3.15, which meant only one layer of van der Waals gap existed in this region.

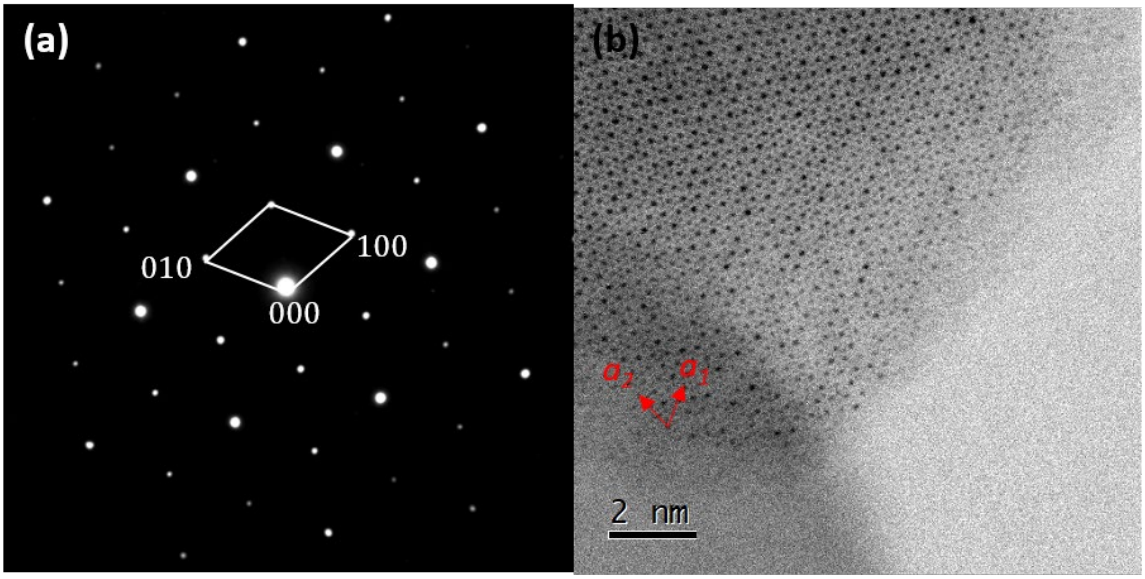

Figure 3.14: (a) TED pattern and (b) STEM Imaging for $x = 0.10$ in the [001] zone axis.

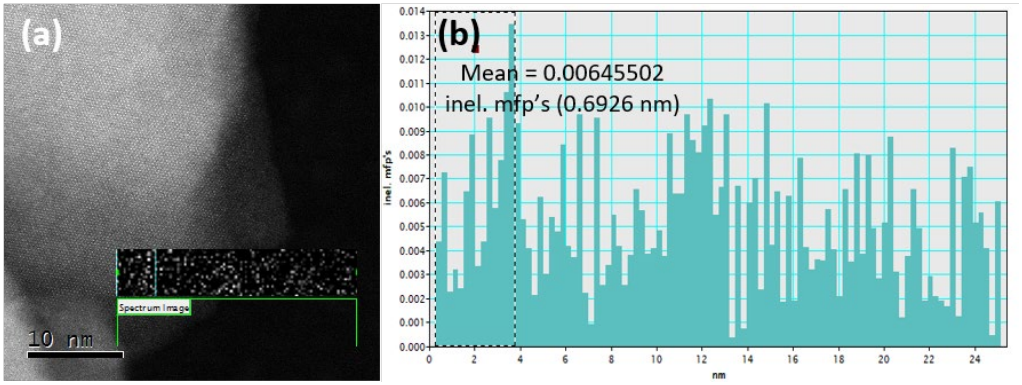

Figure 3.15: (a) Low magnification ADF image of thinner region. Green rectangle area shows the EELS measurement area and the corresponding EELS signal collected at each pixel for thickness measurement. (b) Relative thickness profile obtained by averaging along the short side of the rectangle for $x = 0.10$.

The in-plane Fe distribution could be determined at this region as shown in Figure 3.16. A total of 40 Fe sites and 361 Ti sites were identified, and this corresponded to a Fe:Ti ratio of 0.111, matching the intended growth content of x = 0.10. The radial distribution plot in Figure 3.16(b) also shows that the intercalated Fe atoms were preferentially distanced at a $\sqrt{3}a$ bond distance as well, with some $2a$ Fe atomic pairs and Fe atomic clusters. The $\sqrt{3}a$: $2a$ ratio was found to be 1.32, lower than the x = 0.05 specimen.

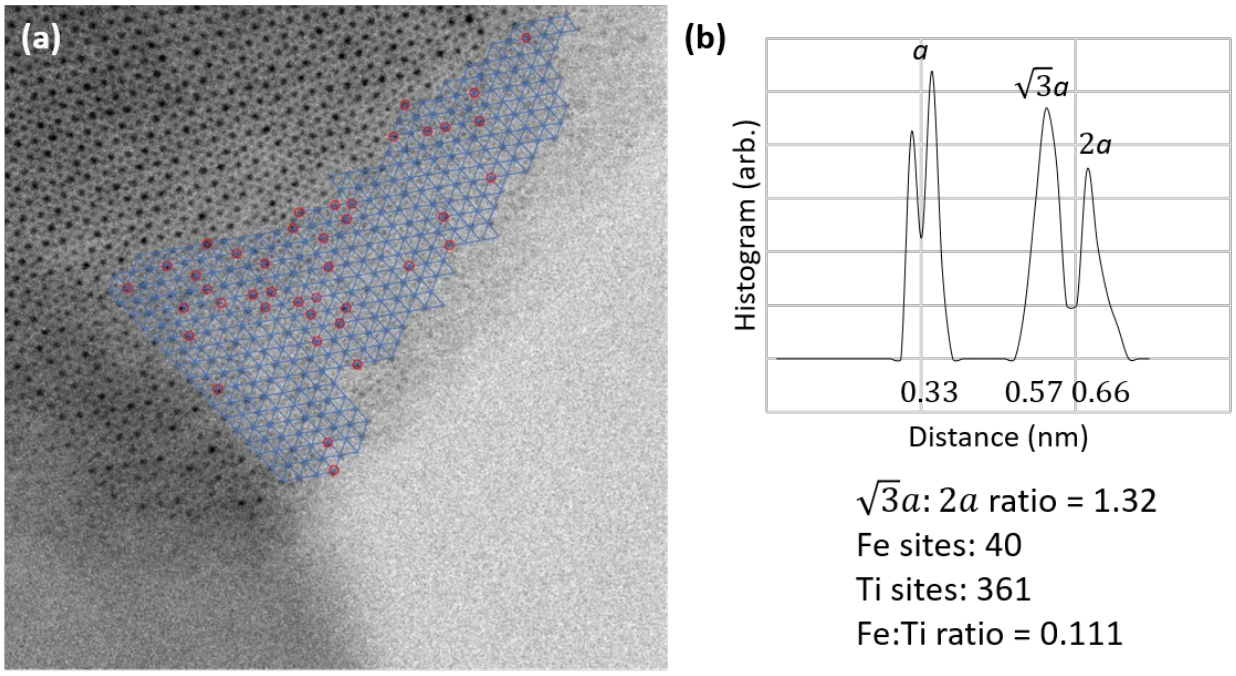

Figure 3.16: (a) Distribution of Fe atoms at the observation area and (b) Radial distribution function of the intercalated Fe atoms for x = 0.10.

The EDS mapping in Figure 3.17 further confirmed the composition at an Fe:Ti atomic ratio of 0.09, which matched the nominal concentration x = 0.10.

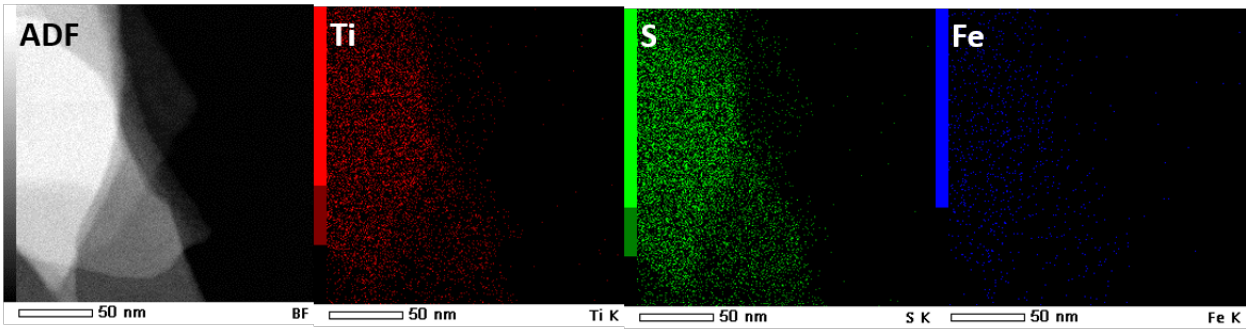

Ele...	Cl...	(keV)	Counts	Mass%	Sigma	Atom%
S K	Ref.	2.307	12518.45	54.50	0.64	64.45
Ti K		4.508	7796.71	41.18	0.64	32.62
Fe K		6.398	662.43	4.32	0.24	2.93
Total				100.00		100.00

Figure 3.17: EDS mapping of the $x = 0.10$ specimen.

The TED patterns and ABF images were taken from the [010] and $[\bar{1}20]$ directions as shown in Figure 3.18. The TED patterns were similar to the TED patterns for TiS_2 host structure, indicating the intercalated Fe atoms did not have any specific ordering. The ABF images in Figure 3.18(c) and (d) do show more Fe atoms in between the van der Waals gaps, as indicated by the orange arrows. However, it was difficult to observe the Fe atoms in the $[\bar{1}20]$ direction. The sample was relatively thicker.

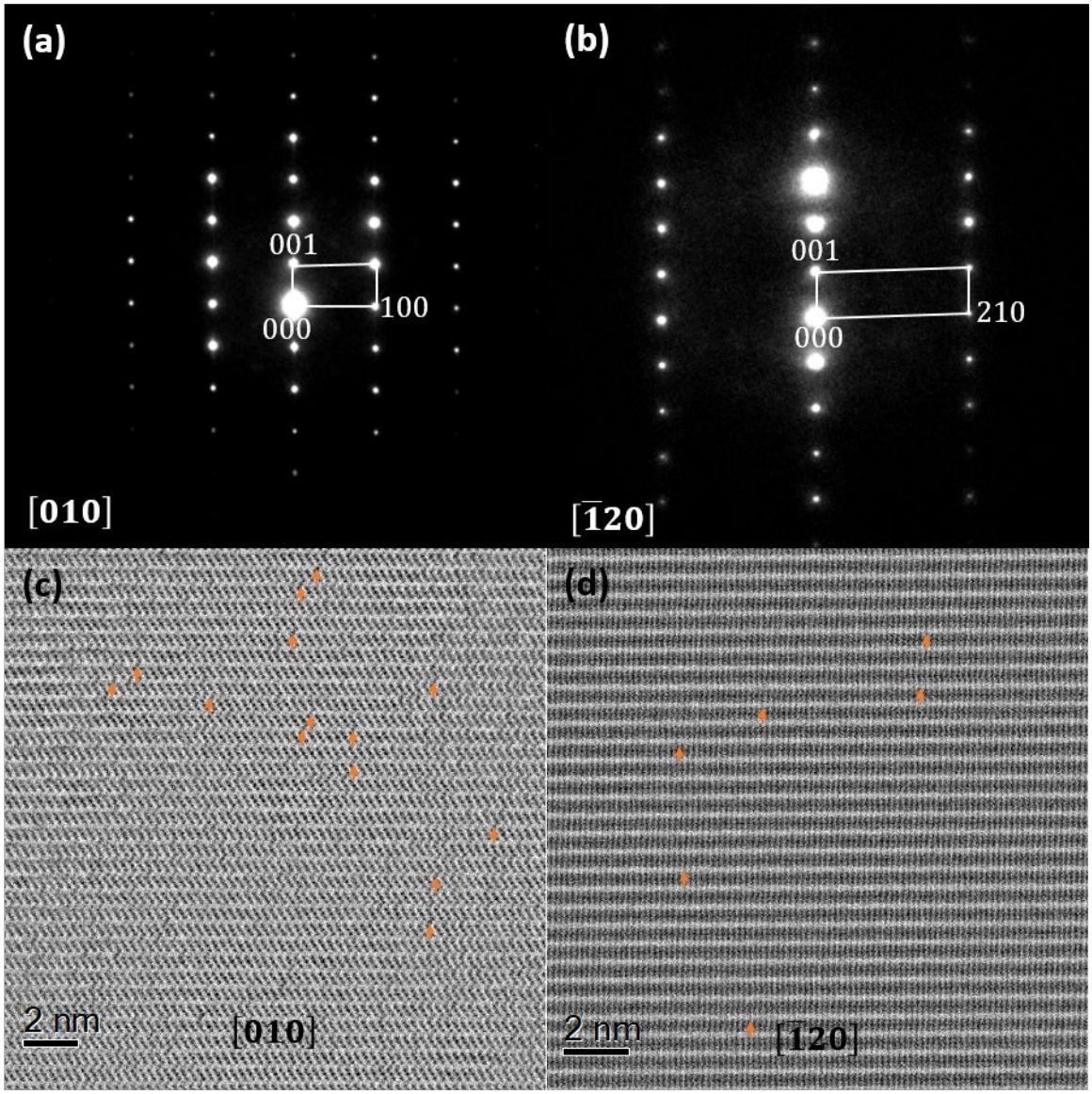

Figure 3.18: TED patterns in cross sectional views of (a) [010] and (b) [$\bar{1}$20] directions. (c) and (d) shows the ABF images taken from these directions, respectively.

3.3.3.4. $x = 0.15$

Figure 3.19 shows the TED pattern and ABF image at x = 0.15 viewed from the [001] zone axis. The TED shows only fundamental reflections of host TiS_2 structure, which is the same pattern with Fe_xTiS_2 structure of x=0, 0.05 and 0.1. It indicates no long range ordering of Fe atoms for

x=0.15. Similar to the ABF images of x=0.05 and 0.10, the ABF image in Figure 3.19(b) showed darker contrast at some Ti sites in thin region, indicating the intercalation of Fe atoms. Here, more Fe sites were observed as compared to x = 0.05 and 0.10.

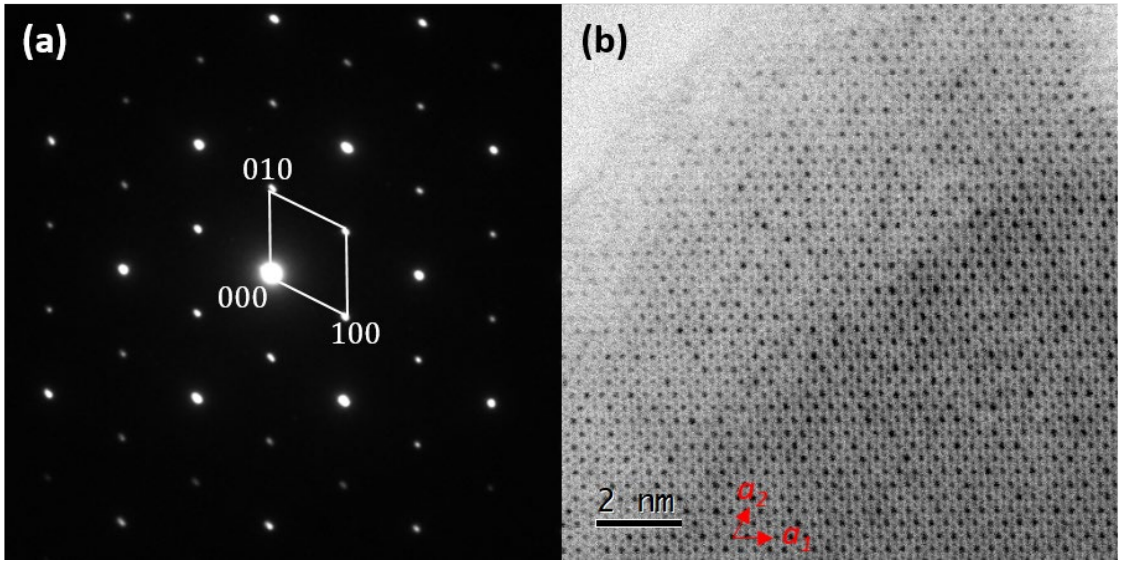

Figure 3.19: (a) TED pattern and (b) STEM Imaging for x = 0.15 in the [001] zone axis.

EELS thickness measurement in Figure 3.20 shows that the thickness at this area was approximately 0.71 nm, which was slightly larger than the lattice parameter along the c-axis of TiS_2 host structure (0.5691 nm), thus confirming the presence of only a layer of Fe atoms in this region. The in-plane Fe distribution analysis in Figure 3.21 also shows that the Fe atoms were preferentially arranged at a distance of $\sqrt{3}a$, with ratio = 1.31. The Fe:Ti ratio of 0.133 in this region also matched well the intended concentration. The composition was further confirmed by the results in EDS mapping in Figure 3.22, showing the Fe:Ti ratio of 0.154.

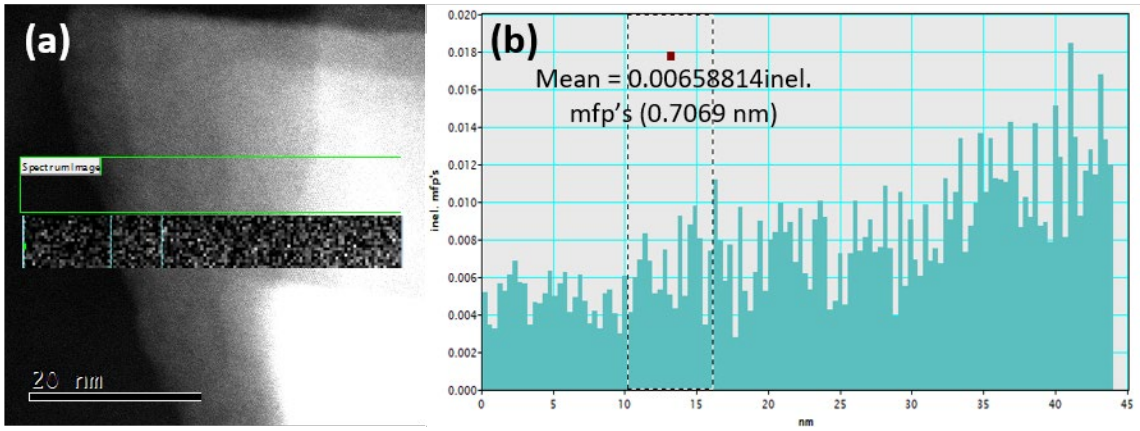

Figure 3.20: (a) Low magnification ADF image of thinner region. Green rectangle area shows the measurement area with the EELS signal obtained at each pixel for thickness measurement. (b) Relative thickness profile obtained by averaging along the short side of the rectangle for x = 0.15.

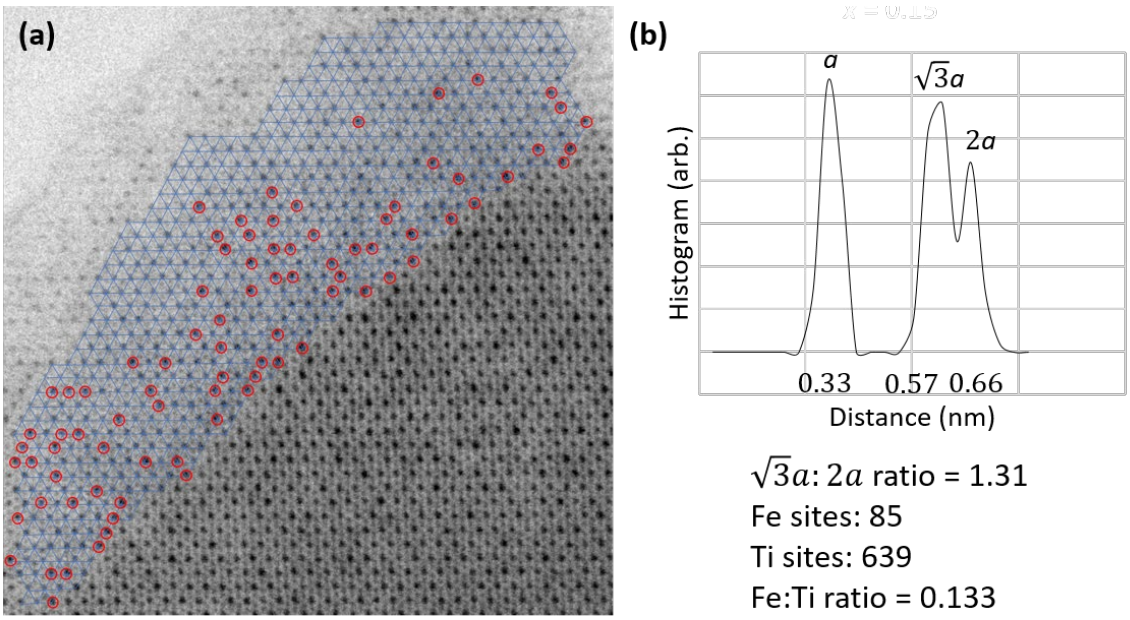

Figure 3.21: (a) Distribution of Fe atoms at the observation area and (b) Radial distribution function of the intercalated Fe atoms for x = 0.15.

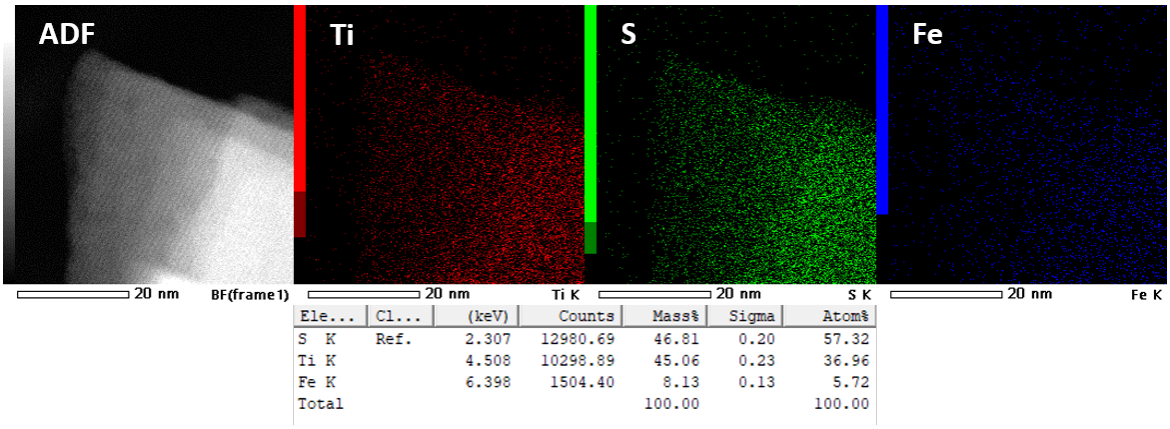

Ele...	Cl...	(keV)	Counts	Mass%	Sigma	Atom%
S K	Ref.	2.307	12980.69	46.81	0.20	57.32
Ti K		4.508	10298.89	45.06	0.23	36.96
Fe K		6.398	1504.40	8.13	0.13	5.72
Total				100.00		100.00

Figure 3.22: EDS mapping of the $x = 0.15$ specimen.

Figure 3.23 shows the TED patterns and ABF images viewed from the directions of [010] and $[\bar{1}20]$ for $x = 0.15$, with some of the Fe atoms indicated by the orange arrows. The specimen still showed only fundamental reflections of TiS_2 but the Fe contrast in the ABF images became more apparent due to the higher concentration. However, still no Fe ordering could be observed between the layers.

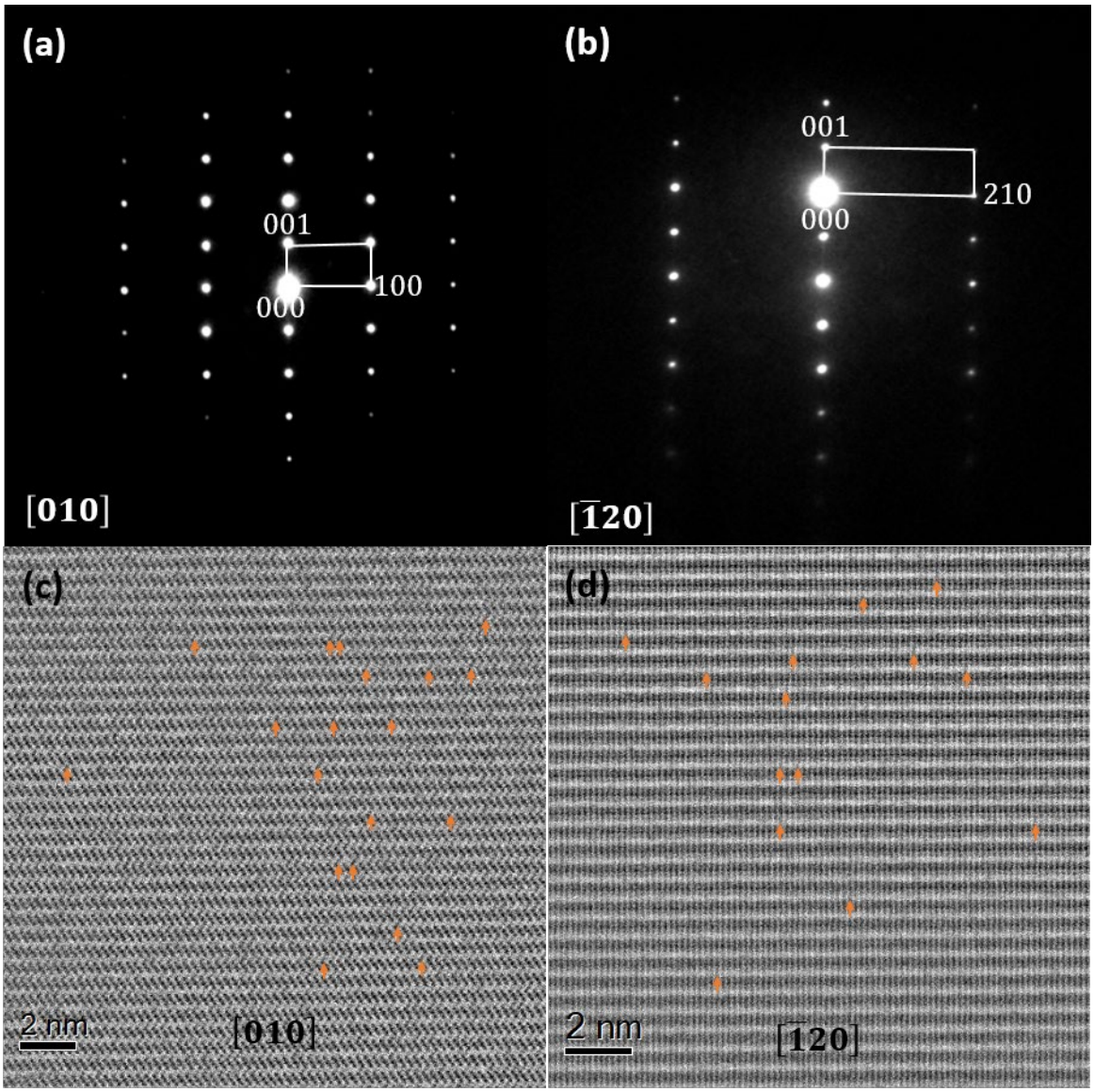

Figure 3.23: TED patterns viewing from (a) [010] and (b) [$\bar{1}$20] directions. (c) and (d) show the corresponding ABF images, respectively.

3.3.3.5. $x = 0.20$

When the Fe content was further increased to $x = 0.20$, some areas displayed TED patterns like the one in Figure 3.24(a), with weak reflections at (1/2, 0), (0, 1/2) and (1/2, 1/2), suggesting short-range ordering of $2a \times 2a \times 2c$. Whereas some areas still displayed only fundamental spots of

TiS_2. The ABF image (Figure 3.24(b)) showed the presence of Fe atoms but no specific long-range ordering was observed. The thickness at this region was estimated to be 0.86 nm by thickness measurement of EELS as shown in Figure 3.25, which meant only one layer of van der Waals gap. The observations suggest that at higher Fe concentration, the Fe atoms started to form short-range ordering of $2a \times 2a \times 2c$.

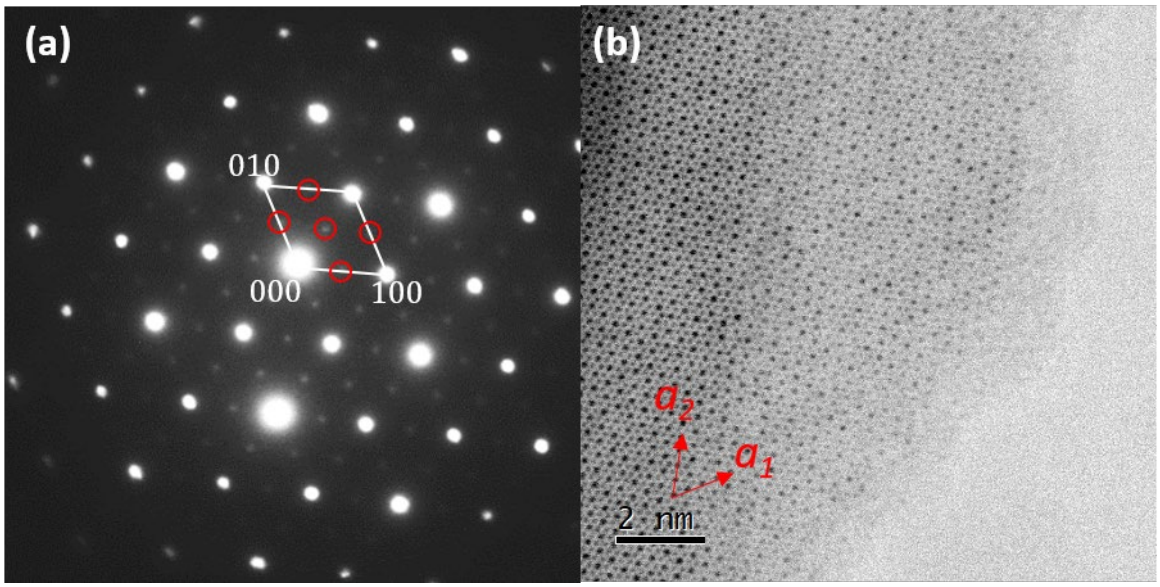

Figure 3.24: (a) TED pattern and (b) ABF Imaging for x = 0.20 in the [001] zone axis.

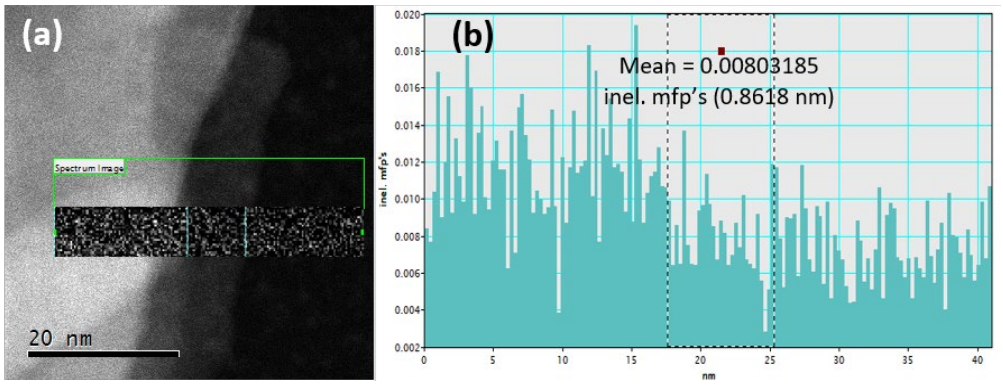

Figure 3.25: (a) Low magnification ADF image of thinner region. Green rectangle area shows the measurement area with the EELS signal obtained at each pixel for thickness measurement. (b) Relative thickness profile obtained by averaging along the short side of the rectangle for x = 0.20.

A total of 114 Fe sites and 639 Ti sites were identified (Figure 3.26(a)), which corresponded to a Fe:Ti ratio of 0.179, which almost matched the nominal Fe concentration. The radial distribution plot in Figure 3.26(b) showed that the ratio of $\sqrt{3}a$: $2a$ was 1.08, which was lower than those at x=0.05, 0.10 and 0.15. It seemed that as the concentration of Fe got higher, the Fe atoms started to rearrange themselves in a manner where a bond distance of $2a$ became higher. The EDS mapping in Figure 3.27 confirmed the composition at an Fe:Ti atomic ratio of 0.21, which matched the nominal concentration x = 0.20.

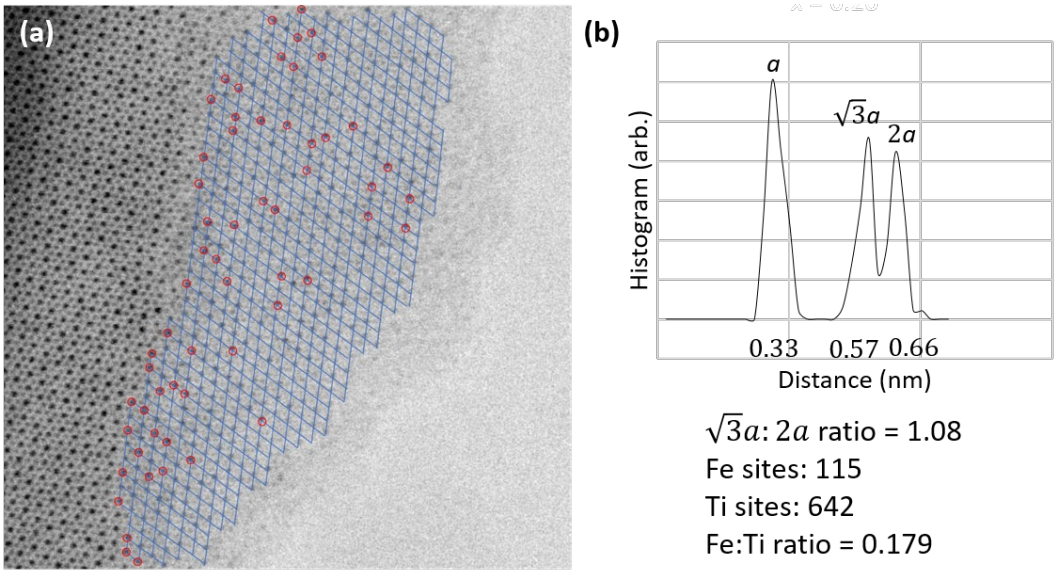

Figure 3.26: (a) Distribution of Fe atoms at the observation area and (b) Radial distribution function of the intercalated Fe atoms for x = 0.20.

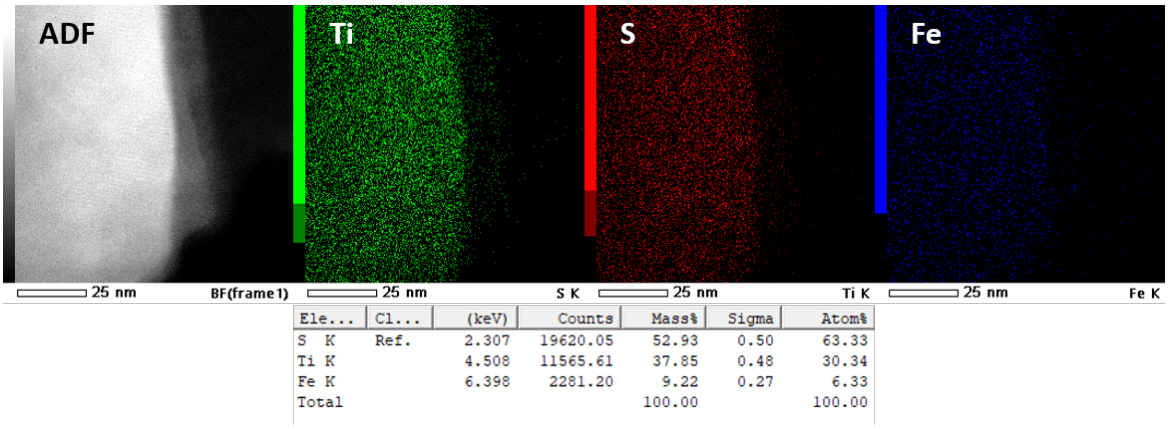

Ele...	Cl...	(keV)	Counts	Mass%	Sigma	Atom%
S K	Ref.	2.307	19620.05	52.93	0.50	63.33
Ti K		4.508	11565.61	37.85	0.48	30.34
Fe K		6.398	2281.20	9.22	0.27	6.33
Total				100.00		100.00

Figure 3.27: EDS mapping of the $x = 0.20$ specimen.

In the cross-sectional TED patterns (Figure 3.28(a-b)), weak superstructure reflections were observed in the reciprocal unit cells of TiS_2 host structure in the [010] and $[\bar{1}20]$ zone axes. The presence of these weak superstructure reflections suggested some short-range Fe ordering in the TiS_2 host structure along both the *a* and *c*-axes. The weak superstructure reflections appeared at the center of the reciprocal unit cells, at the positions of (1/2, 1/2, 0) and (1, 1/2, 0), respectively. It suggests 2*c* ordering along the *c*-axis and also 2*a* ordering along the *a* or *b*-axis.

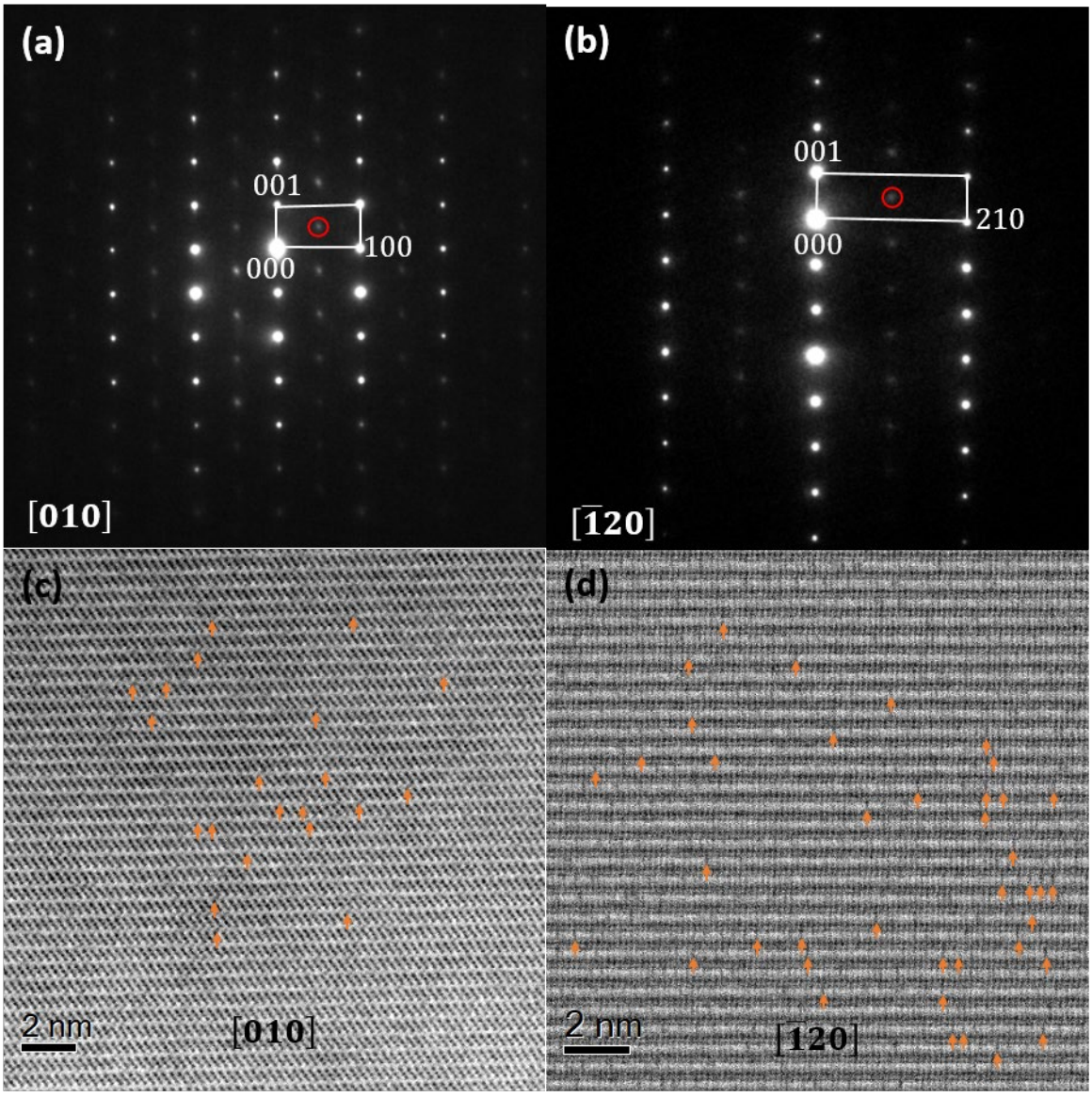

Figure 3.28: TED patterns in cross sectional views of (a) [010] and (b) [$\bar{1}$20]. (c) and (d) show the corresponding ABF images, respectively.

3.3.3.6. $x = 0.25$

When the concentration of Fe atoms increased to $x = 0.25$, two types of TED patterns were captured as well. One showed only fundamental reflections of TiS_2 while the second type was as shown in Figure 3.29(a). In this TED pattern, clear superstructure reflections could be observed at

the positions of (1/2, 0, 0) and (1/2, 1/2, 0) in the reciprocal unit cell. The positions of these reflections in reciprocal unit cell suggested 2*a* ordering in the a_1 direction, *a* ordering in the a_2 direction. The intercalated Fe atoms, as indicated by the orange circles in the ABF image of Figure 3.29(b), could be seen to be aligned in lines, creating a basic unit of $2a \times a$, which is consistent with the result of the TED pattern. This was different from what was expected from previous studies, which reported the formation of $2a \times 2a$ at $x = 0.25$ [4], [31]. In addition, the Fe:Ti atomic ratio for $2a \times a$ superstructure do not match the intended concentration of $x = 0.25$. If the Fe atoms exist in the same atomic plane, then the superstructure would have a Fe concentration of 0.5. So, the only possibility is that the Fe atoms may not be in the same plane along the [001] direction. This idea is supported by the EDS mapping results in Figure 3.30, confirming that the Fe:Ti atomic ratio is 0.27.

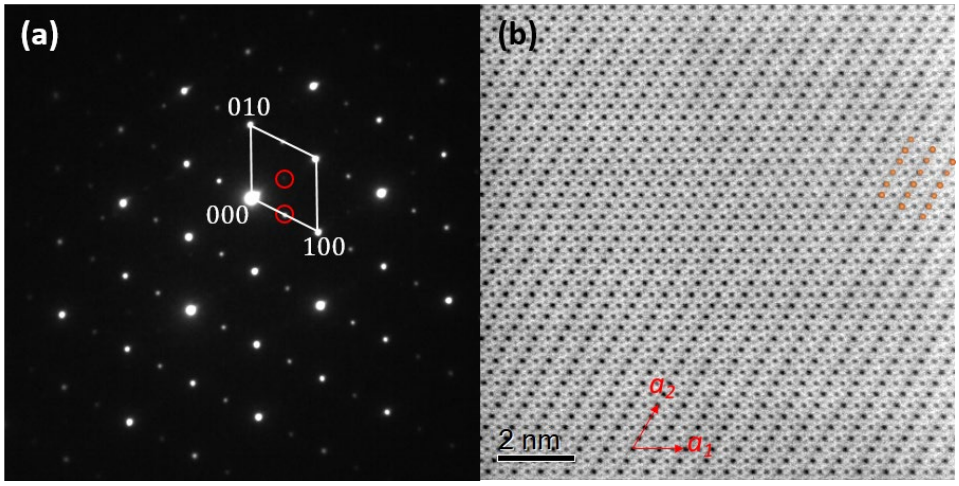

Figure 3.29: (a) TED pattern and (b) ABF Imaging for $x = 0.25$ in the [001] zone axis.

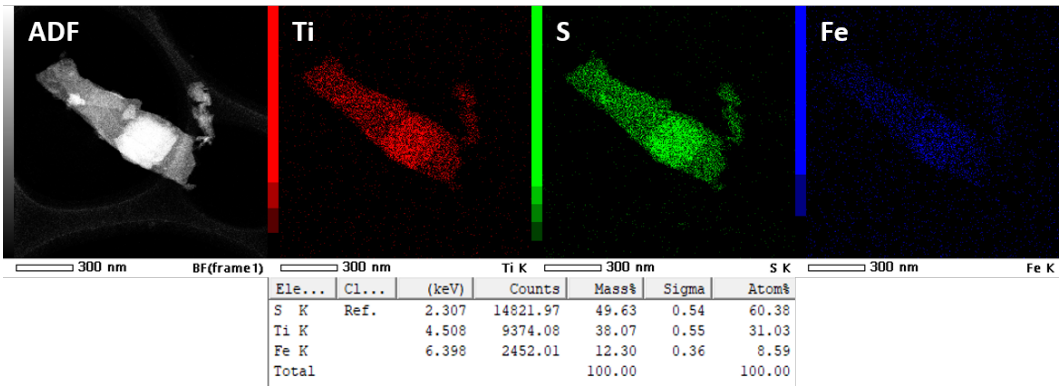

Ele...	Cl...	(keV)	Counts	Mass%	Sigma	Atom%
S K	Ref.	2.307	14821.97	49.63	0.54	60.38
Ti K		4.508	9374.08	38.07	0.55	31.03
Fe K		6.398	2452.01	12.30	0.36	8.59
Total				100.00		100.00

Figure 3.30: EDS mapping of the $x = 0.25$ specimen.

It is further supported by the thickness measurement from EELS log-ratio method in Figure 3.31. The thickness was estimated to be 2.30 nm, which was almost four times thicker than the lattice unit of TiS_2. It meant that there were four layers of van der Waals gaps. In the ABF image, the contrast (difference between background and peak intensity) of the Ti atomic columns with and without Fe atoms intercalated were roughly measured to be 120 and 80, respectively. Since the atomic numbers of Fe (26) and Ti (22) are close, these atoms can be assumed to have the same contribution to the ABF image intensity. Based on this assumption, when there are four Ti atoms in the atomic column without Fe atoms, there should be another two Fe atoms in the atomic column with Fe atoms. This suggests that Fe atoms may be alternately arranged at the same site as Ti atomic positions adjacent to each other along the *c*-axis.

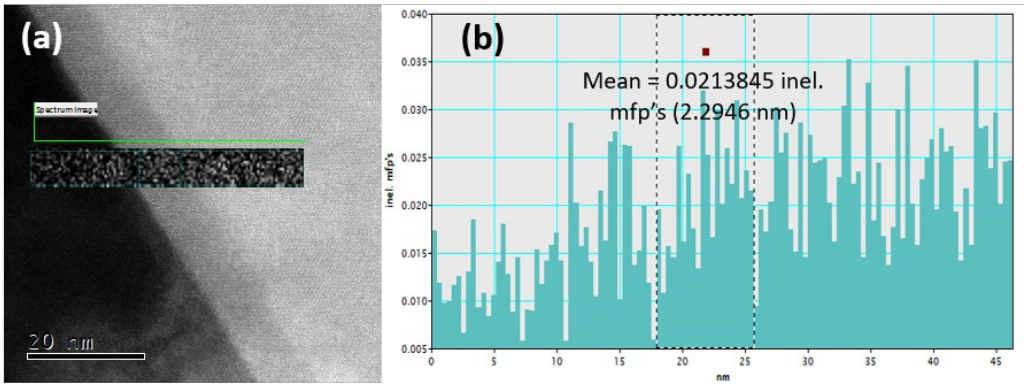

Figure 3.31: (a) Low magnification view of ADF image showing the thickness measurement region. (b) EELS relative thickness plot of the observation area for $x = 0.25$.

The cross sectional TED patterns and ABF images in the [010] and $[\bar{1}20]$ directions are shown in Figure 3.32. Clear superstructure reflections could be seen at the (1/2, 0, 1/2) position of the reciprocal unit cell in the TED pattern viewing from the [010] direction and at the (1, 0, 1/2) position of the reciprocal unit cell in the TED pattern viewing from the $[\bar{1}20]$ direction. They suggested 2*c* ordering along the *c*-axis and also 2*a* ordering along the *a* or *b*-axis. The ABF observations in these directions shows 2*c* ordering clearly. The Fe atoms, as indicated by the orange circles, could be seen shifted one site, between layers, creating an ABAB layer structure. Along the *a*-axis, the Fe atoms could be seen alternating at every 2*a* distance as well, which matched the results of ABF and TED observation in the [001] direction.

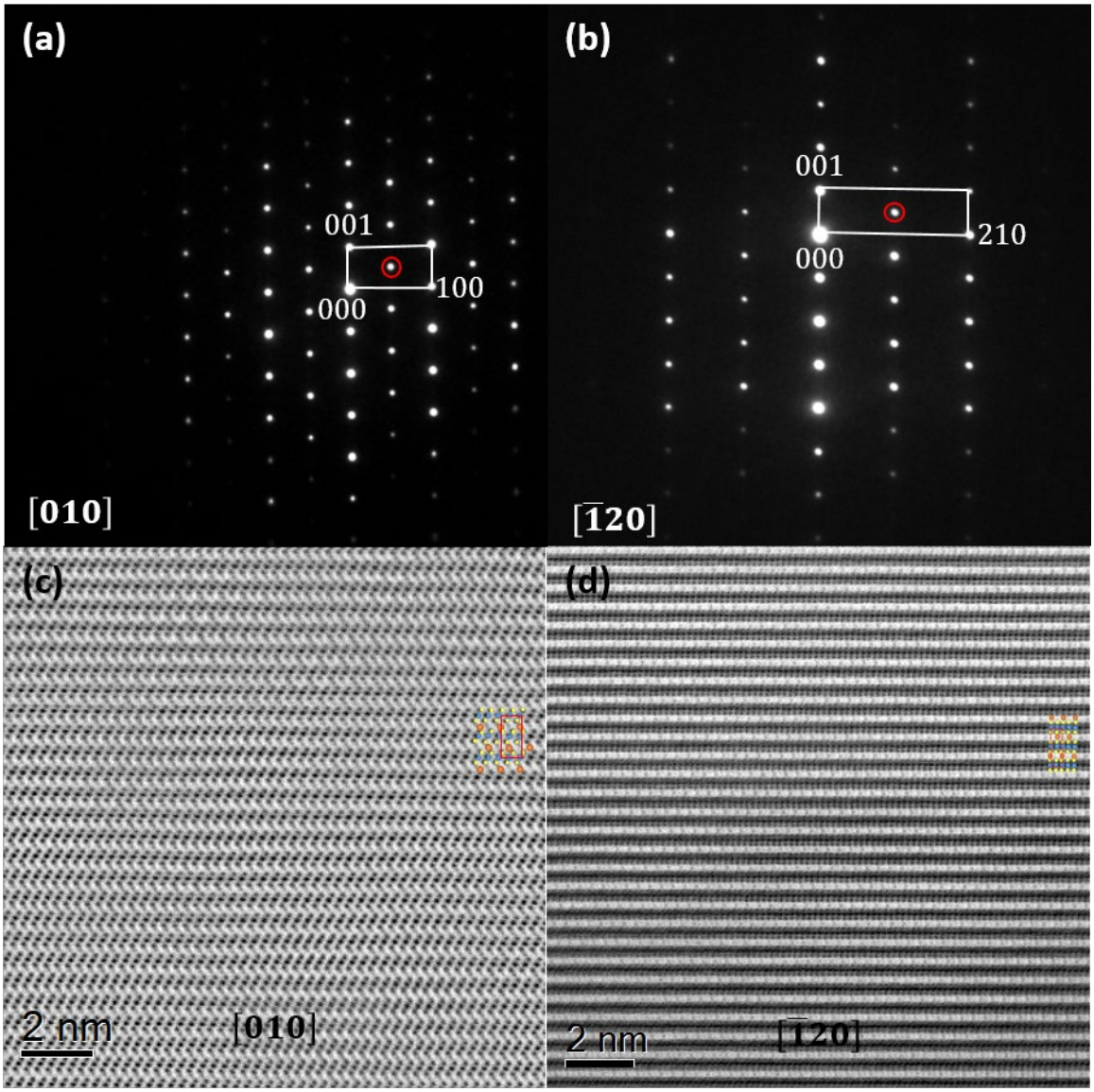

Figure 3.32: TED patterns in cross sectional views of (a) [010] and (b) [$\bar{1}$20]. (c) and (d) show the ABF images of the cross-sectional views.

Combining the experimental TED patterns and ABF images taken from three perpendicular directions, Fe ordering is clarified for the $Fe_{0.25}TiS_2$ structure as shown in Figure 3.33(a). Figure 3.33(b) is a bird's-eye view of three-dimensional atomic model. The blue circles represent Ti atoms,

yellow circles represent S atoms, orange and golden circles represent Fe atoms at the layers of 1/4 and 3/4, respectively in the van der Waals gaps.

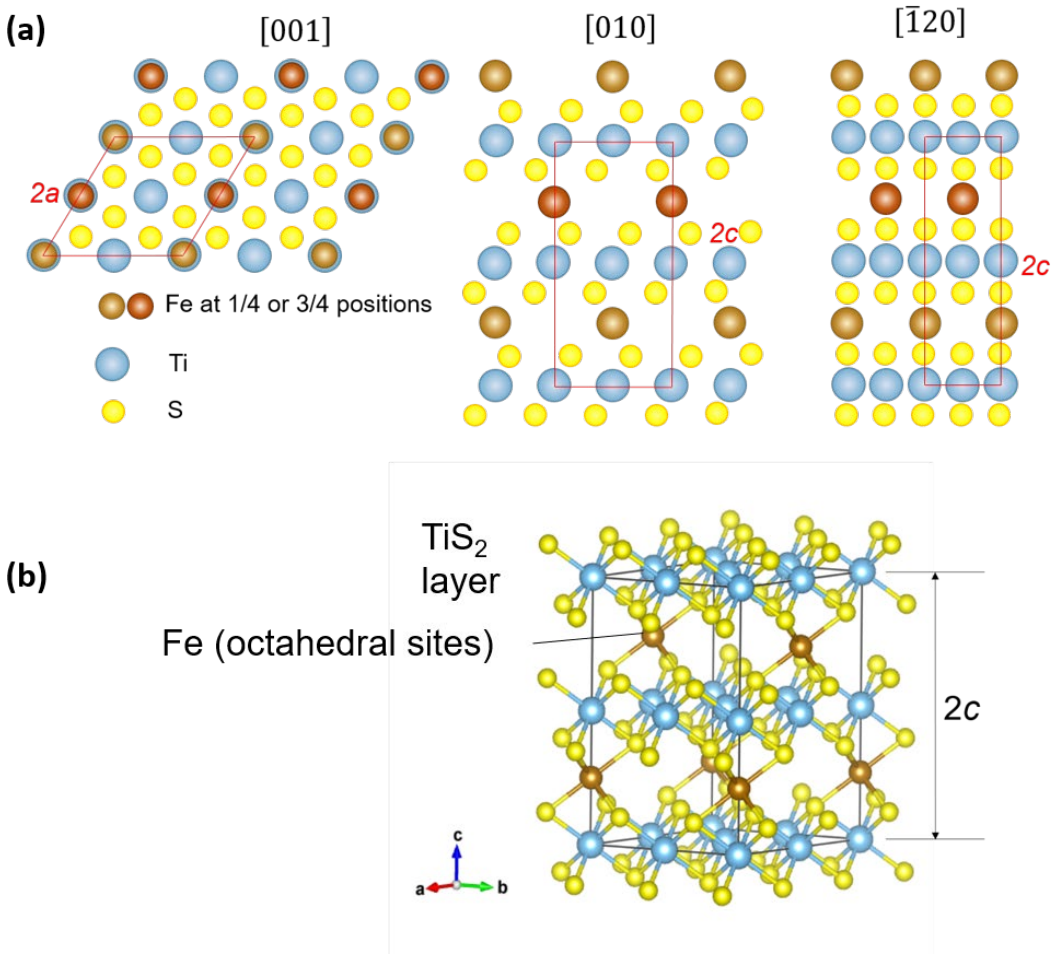

Figure 3.33: (a) Fe distribution, as observed in STEM from the directions of [001], [010] and [$\bar{1}$20]. (b) 3-dimensional model of the atomic structure for $x = 0.25$.

Simulated ABF images viewing from the zone axes of [001], [010] and [$\bar{1}$20] direction (Figure 3.34) confirm the validity of the proposed atomic model. Intensities of individual atomic columns in simulated ABF images reproduce the experimental results. Thus, we conclude that Fe_xTiS_2 at $x = 0.25$ has a superstructure structure of $2a \times 2a \times 2c$.

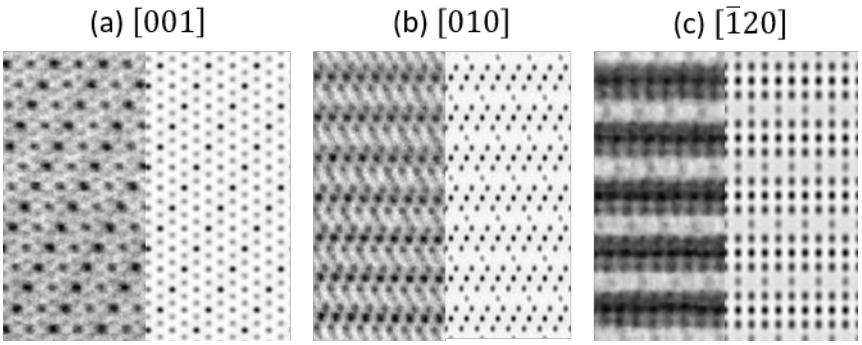

Figure 3.34: Comparison of STEM simulations with actual observations to validate the atomic model.

3.3.3.7. $x = 0.33$

Similar to $x = 0.25$, the Fe_xTiS_2 structure of $x = 0.33$ showed two types of TED patterns when viewing from the [001] direction. One only showed the fundamental reflections of TiS_2 structure, while another showed the superstructure reflections at the positions of (1/3, 2/3, 0) and (2/3, 1/3, 0) in the reciprocal unit cell (Figure 3.35(a)). These positions correspond to the $\sqrt{3}a \times \sqrt{3}a$ superstructure, which is the same result with the previous studies [4], [31]. ABF image in Figure 3.35(b) shows that the Fe atoms form honeycomb pattern, as indicated by orange circles. However, at thinner regions on the left near the edge of the specimen, a $\sqrt{3}a \times \sqrt{3}a$ Fe arrangement could be observed, as indicated by open orange circles. So, the honeycomb pattern could be a result of two $\sqrt{3}a \times \sqrt{3}a$ layers stacked in different positions whereas the area on the left consisted of only a layer of $\sqrt{3}a \times \sqrt{3}a$. The EDS mapping in Figure 3.36 confirmed that the Fe:Ti matched the intended growth concentration of $x = 0.33$.

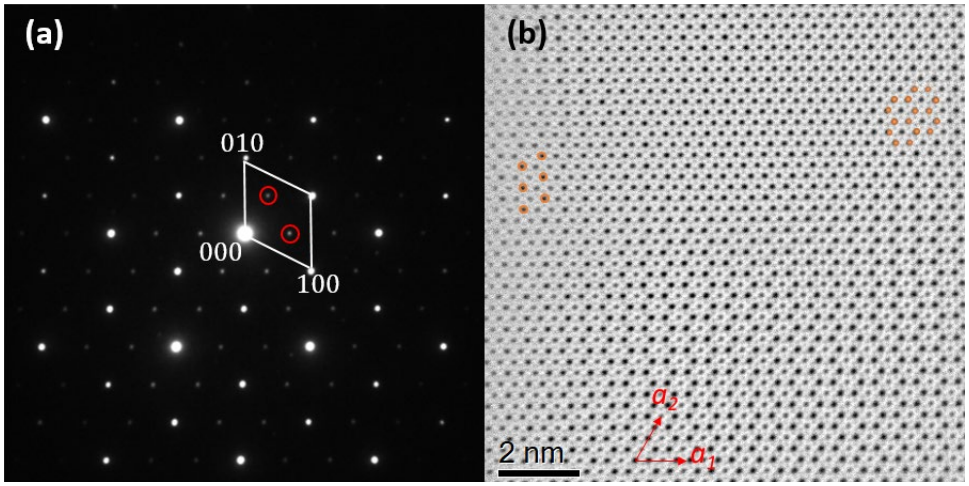

Figure 3.35: (a) TED pattern and (b) ABF Imaging for $x = 0.33$ in the [001] zone axis.

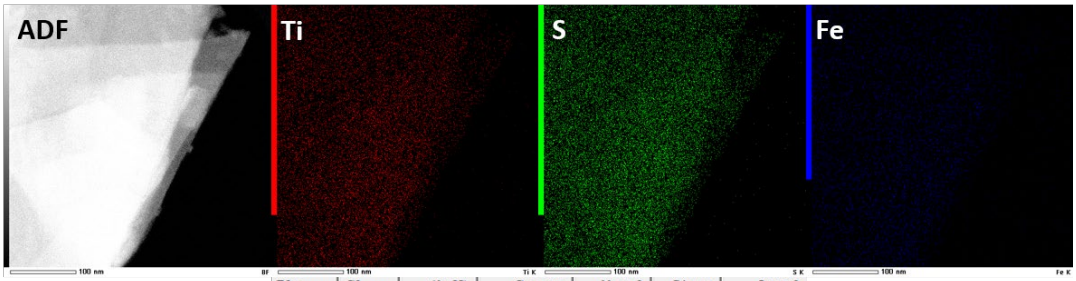

Ele...	Cl...	(keV)	Counts	Mass%	Sigma	Atom%
S K	Ref.	2.307	28538.17	49.26	0.38	60.15
Ti K		4.508	18198.27	36.50	0.37	29.86
Fe K		6.398	5918.02	14.24	0.26	9.98
Total				100.00		100.00

Figure 3.36: EDS mapping of the $x = 0.33$ specimen.

The EELS log-ratio method showed that the honeycomb area had an estimated thickness of 1.03 nm (Figure 3.37). This thickness was approximately two times the lattice unit of TiS_2 and so, two layers of van der Waals gaps were available for intercalation.

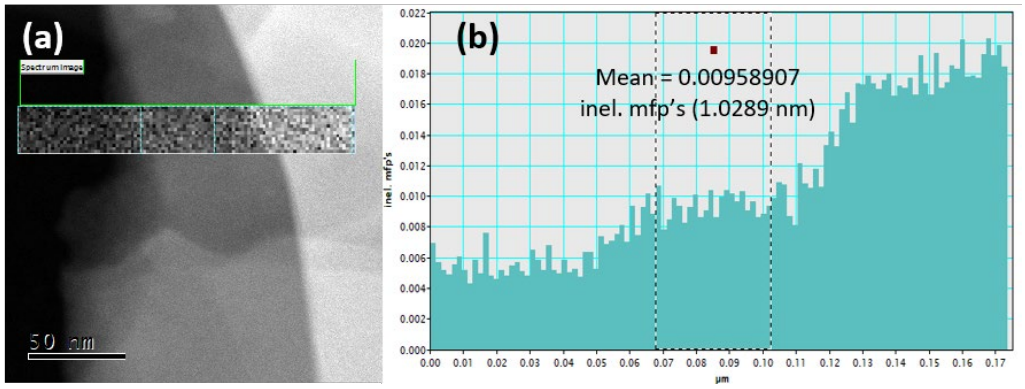

Figure 3.37: (a) Low magnification view of ADF image showing the thickness measurement region. (b) EELS relative thickness plot of the observation area for $x = 0.33$.

When viewing from the [010] direction, the TED pattern of Figure 3.38(a) only showed the fundamental reflections of TiS_2 host structure. The ABF image of Figure 3.38(c) showed that Fe atoms were intercalated at all sites under Ti atomic sites in van der Waals gap. On the other hand, when viewing from the $[\bar{1}20]$ direction, two superstructure reflections were observed at the positions of (2/3, 0, 1/2) and (4/3, 0, 1/2) in the reciprocal unit cell (Figure 3.38(b)). The superstructure reflections at (*h*, *k*, 1/2) indicates a 2*c* ordering along the *c*-axis. The equidistant superstructure reflection along the *210* line suggests an atomic ordering at every three atomic positions. It matched the results in ABF image from Figure 3.38(d) where the Fe atoms were repeated under every three TiS_2 atomic columns in plane and the Fe atoms were shifted one site between two neighboring TiS_2 layers, forming 2*c* ordering along the c-axis.

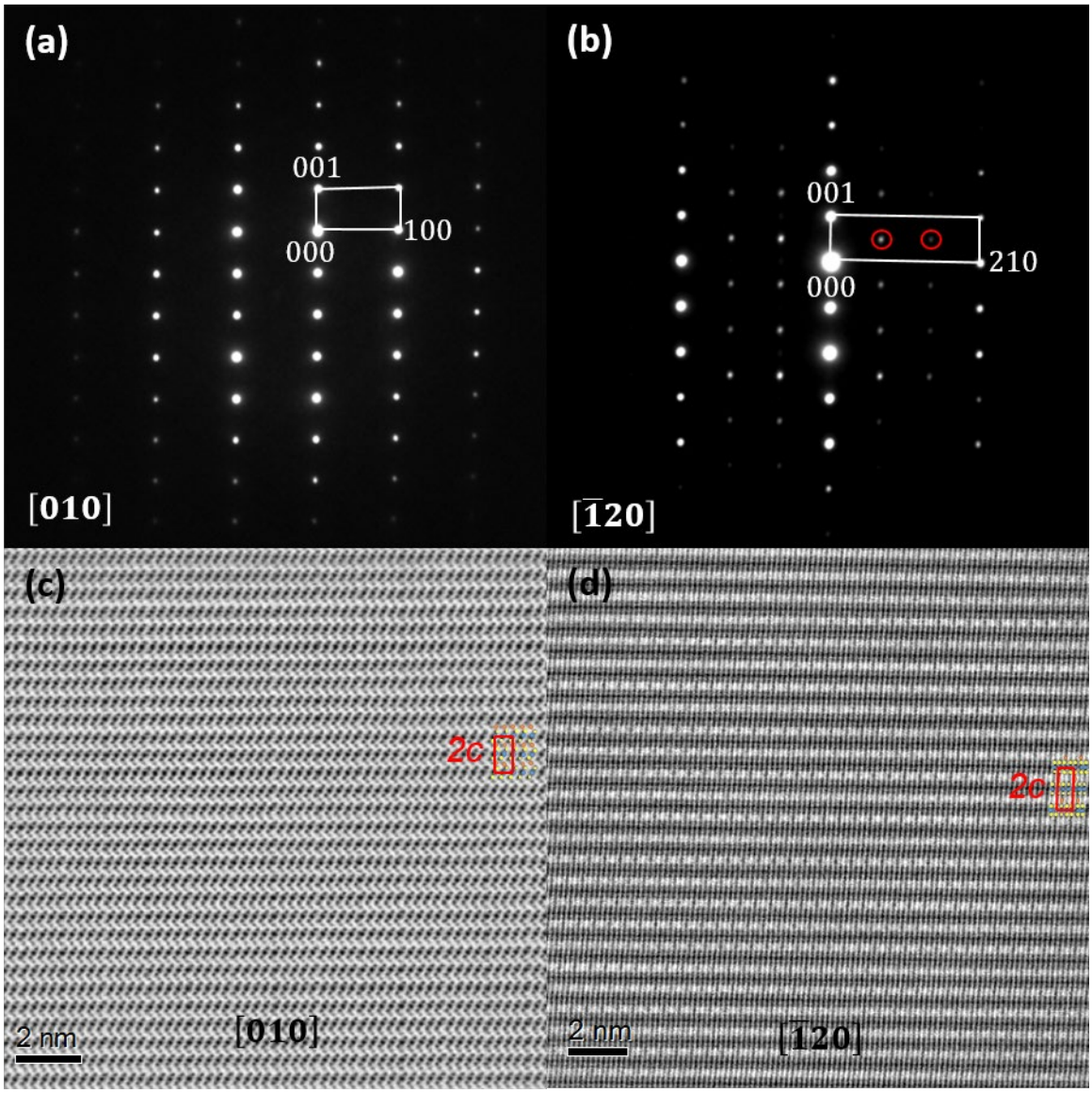

Figure 3.38: TED patterns in cross sectional views of (a) [010] and (b) [$\bar{1}$20]. (c) and (d) show the ABF images of the cross-sectional views.

Based on the Fe distribution as observed in the three perpendicular directions as shown in Figure 3.39(a), the atomic model of $\sqrt{3}a \times \sqrt{3}a \times 2c$ superstructure in Figure 3.39(b) is proposed.

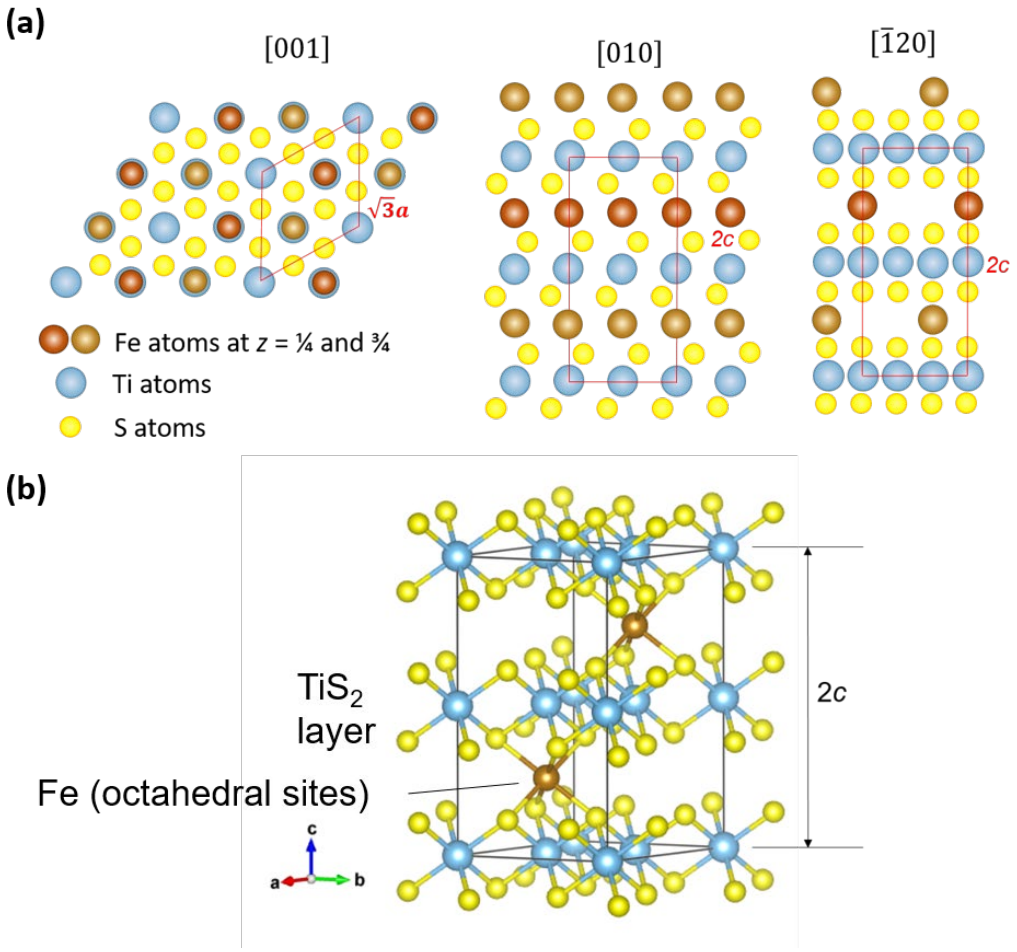

Figure 3.39: (a) Fe distribution, as observed in STEM from the directions of [001], [010] and [$\bar{1}$20]. (b) 3-dimensional model of the atomic structure for x = 0.33.

The simulated ABF images of the proposed atomic model in Figure 3.40 reproduce well the experimental ABF images, which were viewed from the [001], [010] and [$\bar{1}$20] directions, respectively.

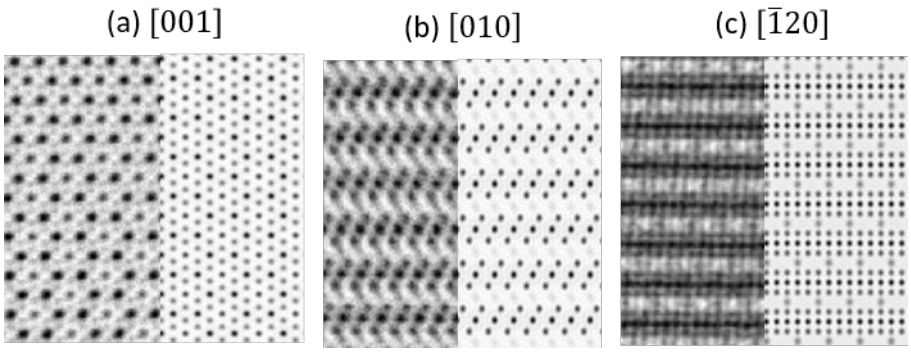

Figure 3.40: STEM simulations to validate the atomic model.

3.4. Discussion

3.4.1. Proposed Growth Mechanism

Chemical vapor transport reaction could be divided into three processes, which include sublimation, transportation and deposition. So, when the reactant powder of Ti, Fe, I_2 and S_2 was heated at high temperature, I_2 and S_2, which had lower sublimation temperature of approximately 184.3°C and 444.6°C respectively, started to form gaseous species first. The S vapor species sulfurized some of Ti powder, forming TiS_2 particles. Whereas the I vapor species acted as transfer agent by reacting with Ti, TiS_2 and Fe powder to form TiI_2 and FeI_2 vapor species, as shown below.

$$Ti(s) + 2S(g) \rightarrow TiS_2(s)$$

$$Ti(s) + 2I(g) \rightleftharpoons TiI_2(g)$$

$$TiS_2(s) + 2I(g) \rightleftharpoons TiI_2(g) + 2S(g)$$

$$Fe(s) + 2I(g) \rightleftharpoons FeI_2(g)$$

The increase in vapor pressure at the reactant region resulted in the TiI_2, FeI_2 and S vapor species to be diffused to the lower temperature end with lower vapor pressure and subsequently recrystallized at this region due to the temperature difference to form nucleus of TiS_2, as shown in Figure 3.41. The released iodine gas increased the partial pressure of iodine at the deposition area and thus they were transported back to the reactant region for further reaction. As more vapor species were transported to the deposition region, these Ti, S and TiS_2 species were adsorbed to the edges of the TiS_2 and caused the growth of TiS_2 along the six edges to form a hexagonal crystal.

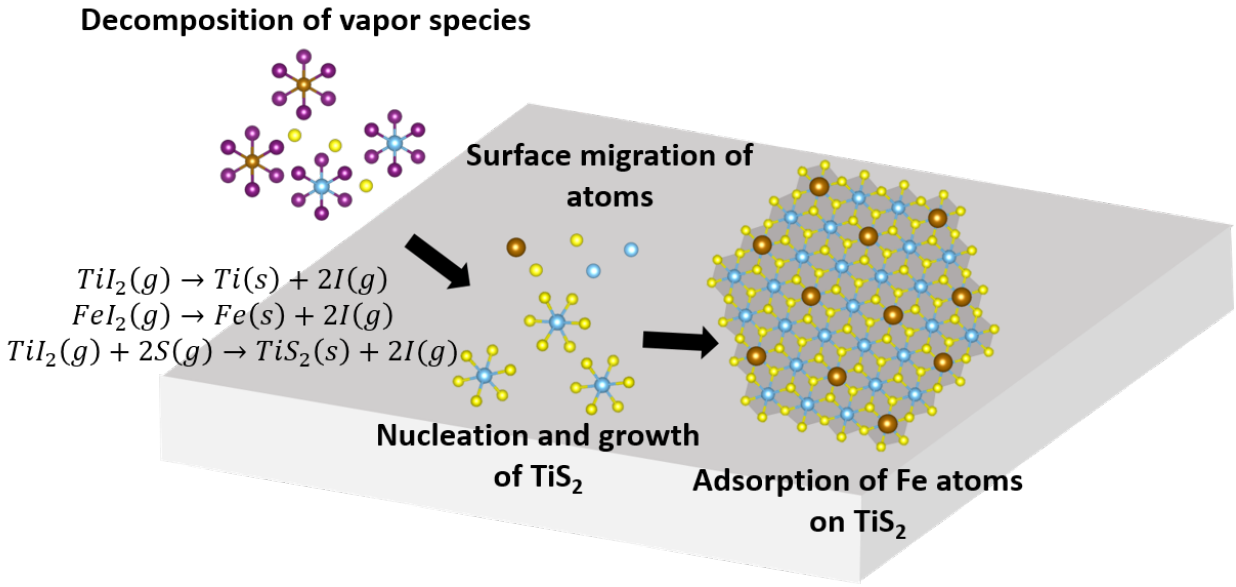

Figure 3.41: Reactions at the deposition site in the quartz ampoule.

As for the Fe atoms, they were preferentially adsorbed onto the octahedral sites at the TiS_2 surface. These Fe atoms then acted as adsorption sites for TiS_2 species to form the next layer of TiS_2. Furthermore, they enhanced the growth of TiS_2 laterally, since the Fe atoms at the edges of the crystals would attract S species. Thus, the size of crystals increased with increasing Fe concentration in Fe_xTiS_2.

Depending on the concentration of Fe atoms available and the attractive-repulsive interatomic interactions between the Fe atoms in-plane, the Fe atoms started to redistribute themselves to appropriate distances. Referring to the work by Negishi et al. [23], the arrangement of Fe atoms in Fe_xTiS_2 was attributed to the multiple pair-interaction potential of the intralayer first nearest neighbor (a_1) and second nearest neighbor (a_2), as well as interlayer interactions of first nearest neighbor (c_1), second nearest neighbor (c_2) and $2c$ interactions, as shown in Figure 3.42. By considering the total of these interactions potentials, they managed to use Monte Carlo method recreate models that had matched well with the XRD results at concentrations of x = 0.15, 0.25 and 0.33 which showed short-range $2a \times 2a \times 2c$, long-range $2a \times 2a \times 2c$ and $\sqrt{3}a \times \sqrt{3}a \times 2c$ ordering, respectively, as shown in Figure 3.43. So, using their model as reference, the Fe arrangement at x = 0.25 and x = 0.33 could be explained for our case as well.

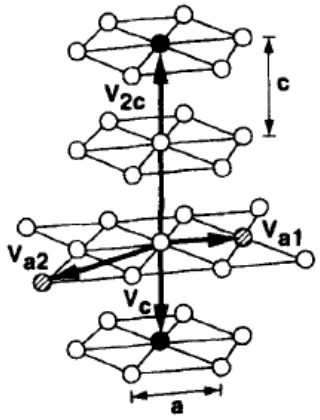

Figure 3.42: Schematic illustration of the interaction of Fe atoms in the layers (v_{a1} and v_{a2}) and between the layers (v_c and v_{2c}). v_{a1} and v_{a2} indicate the interaction between two atoms with distance a and $\sqrt{3}a$ in the layer, respectively. V_c and V_{2c} indicate the interaction between two atoms with distance c and $2c$ between the layers, respectively.

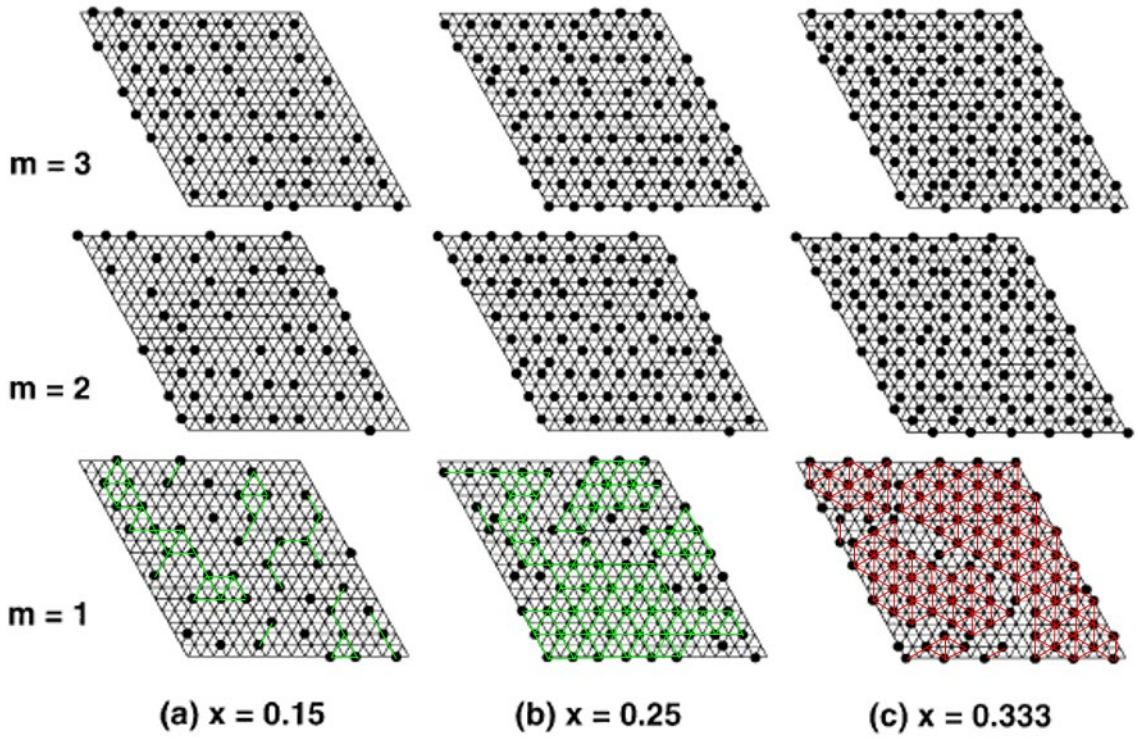

Figure 3.43: Results of Monte Carlo simulations of Fe atomic distribution, assuming both interactions in the layer and between the layers for Fe concentrations of (a) 0.15, (b) 0.25 and (c) 0.33. The results matched the XRD results of short-range $2a \times 2a \times 2c$, long-range $2a \times 2a \times 2c$ and $\sqrt{3}a \times \sqrt{3}a \times 2c$ ordering at x = 0.15, 0.25 and 0.33, respectively. Green line indicates Fe atomic pairs at $2a$ distance and red lines indicate Fe atomic pairs at $\sqrt{3}a$ distance.

However, for the case of low concentration at x = 0.15, they assumed that even at low concentrations of x = 0.15, there were strong interactions between layers and thus because of this attractive $2c$ interatomic interaction, their model showed short-range ordering of $2a \times 2a \times 2c$. However, from the cross-sectional ABF images at low Fe concentrations, there was no ordering of Fe atoms observed between the layers. It suggests that the interaction between layers should be very weak at low Fe concentrations. Furthermore, Negishi et al. made some models by considering only intralayer pair interactions (v_{a1} and v_{a2}) and showed that the Fe atoms would distance

themselves at short-range ordering of $\sqrt{3}a$ and $2a$ ordering (Figure 3.44) with higher preference of $\sqrt{3}a$ ordering at x = 0.15. In our study, the radial distribution studies of the ABF images at very thin region showed that the ratios of $\sqrt{3}a$: $2a$ were 2.36, 1.32, 1.31 and 1.08, respectively, for Fe_xTiS_2 structure at x=0.05, 0.10, 0.15 and 0.20. It indicates that $\sqrt{3}a$ ordering becomes more dominant with decreasing the Fe concentration and interlayer interactions can be ignored at low Fe concentrations.

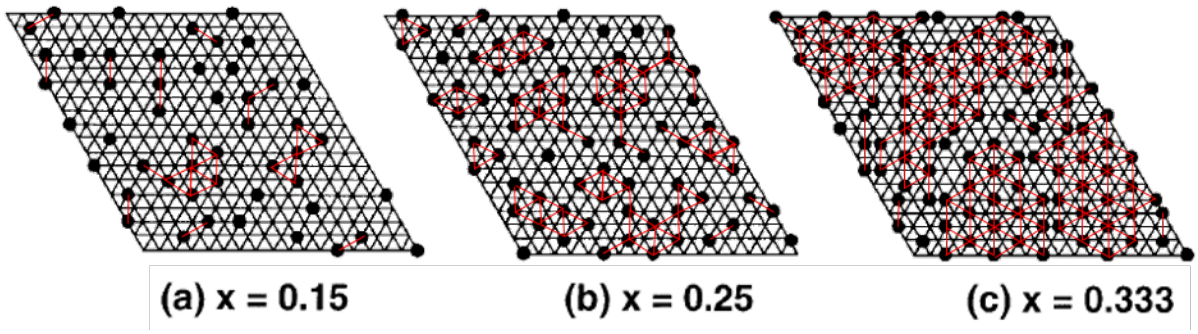

Figure 3.44: Atomic distribution at 3 different layers of Fe_xTiS_2, calculated with only repulsive intralayer interactions at concentrations of (a) x = 0.15, (b) x = 0.25 and (c) x = 0.33, which showed preferential ordering at $\sqrt{3}a$ ordering [23].

So, at low Fe concentrations, it is assumed that the interaction between layers must be relatively weak and the intralayer Fe distribution is determined by the interactions of Fe atoms within the layers only. However, when the Fe concentration was increased to $x \geq .020$, the interlayer interactions might play an important role in the arrangement of Fe atoms. As more atoms were added between the layers, the interlayer interactions would affect the distance between Fe atoms in-plane as well, distancing the Fe atoms further apart to create the $2a \times 2a \times 2c$ superstructure at x = 0.25. When the concentration was further increased to x = 0.33, the Fe atoms had to

rearranged so that they could accommodate more Fe atoms within the layer and thus $\sqrt{3}a \times \sqrt{3}a \times 2c$ superstructure was formed. The redistribution of Fe atoms after adsorption onto the surface at different Fe concentrations is shown in Figure 3.45.

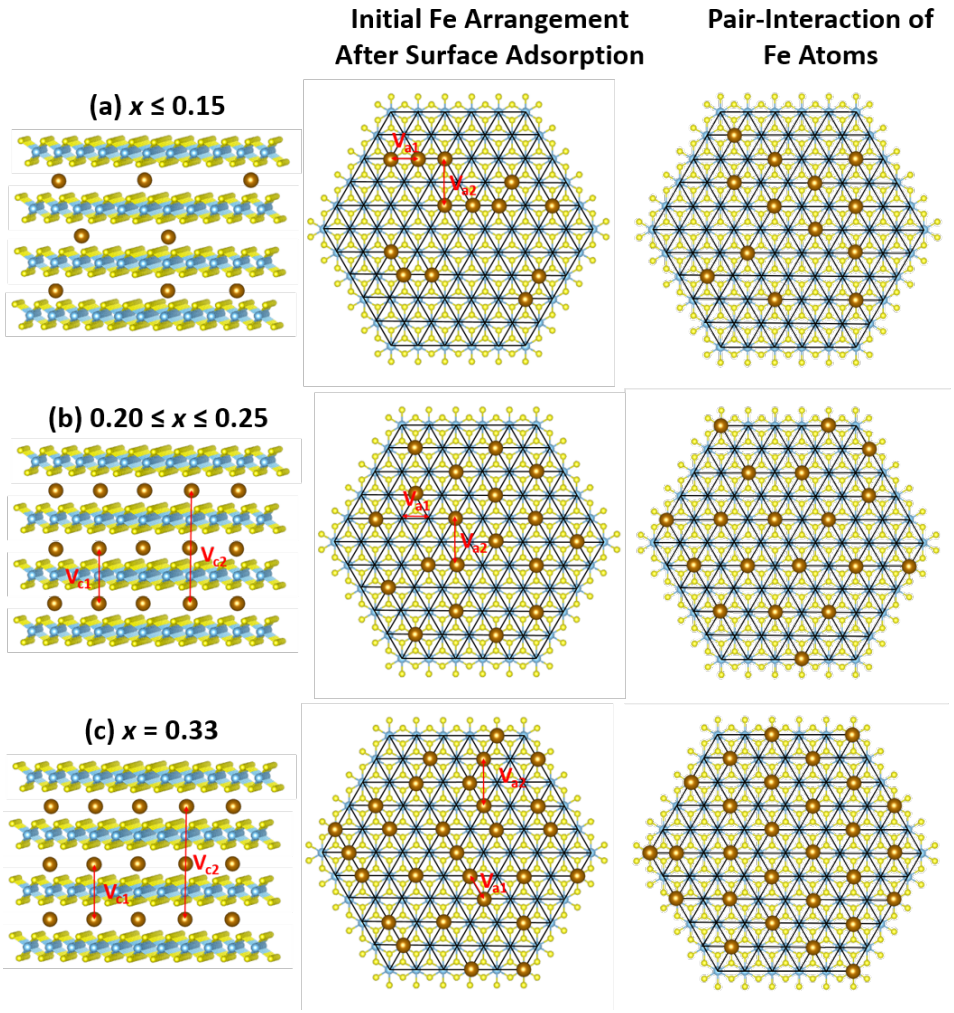

Figure 3.45: Redistribution of Fe atoms after adsorption onto the surface due to the attractive-repulsive pair-interactions of Fe atoms at different concentrations of (a) $x \leq 0.15$, whereby the distribution was only affected by the intralayer repulsive interactions and showed preferential short-range ordering of $\sqrt{3}a$. (b) At $0.20 \leq x \leq 0.25$, both intralayer and interlayer interactions caused the Fe atoms to be distributed further apart at $2a$ distance. (c) As the concentration was increased to $x = 0.33$, both intralayer and interlayer interactions influenced the arrangement but to accommodate the higher Fe content, the atoms were distanced nearer at $\sqrt{3}a$.

3.5. Conclusion

A detailed structural characterization was performed on Fe_xTiS_2 grown at concentrations of x = 0, 0.05, 0.10, 0.15, 0.20, 0.25 and 0.33. XRD results did not show any superstructure peaks. The lack of superstructure peaks might be due to several reasons. One is the low energy and intensity of the X-ray source, which means lower depth penetration and thus might have missed out some important crystal information. Another reason is the interference effect of several phase boundaries that exist in the crystals. But, XRD results showed that the lattice parameters of the TiS_2 host structure slightly expand in both a and c axes as the Fe concentration increased. The bonds of Fe atoms with the surrounding S atoms must be readjusted depending on the Fe concentration. The higher the number of Fe atoms, more bonds will be formed, resulting in expansion of the van der Waals gap distance.

On the other hand, TEM studies seem to be effective in identifying the ordering of intercalated Fe atoms in Fe_xTiS_2 structure, even though they provide only local structure information. By preparing very thin TEM samples of the Fe_xTiS_2 structure, we can obtain the distribution of Fe atoms in one layer to confirm what kind of short range ordering of Fe atoms exist depending on the Fe concentration. Also, by observing the Fe_xTiS_2 structure from three different directions of $[001]$, $[010]$ and $[\bar{1}20]$directions, we confirm the superstructure of the Fe_xTiS_2 structure three-dimensionally.

At low concentrations of Fe ($x \leq 0.15$), the intercalated Fe atoms were not totally random and they could be seen arranged at distances of $\sqrt{3}a$ and $2a$. However, the distribution functions showed that more Fe atoms were distanced at $\sqrt{3}a$. x = 0.20 was the starting point at which the Fe atoms started to be arranged along the c-axis as well, forming short-range ordering of $2a \times 2a \times$

$2c$. At higher concentrations, long-range ordering of Fe atoms were observed within the *ab*-plane and along the *c*-axis, forming 3D superstructures of $2a \times 2a \times 2c$ and $\sqrt{3}a \times \sqrt{3}a \times 2c$ at concentrations of x = 0.25 and 0.33, respectively. Figure 3.46 shows the summary on Fe ordering at different Fe concentrations.

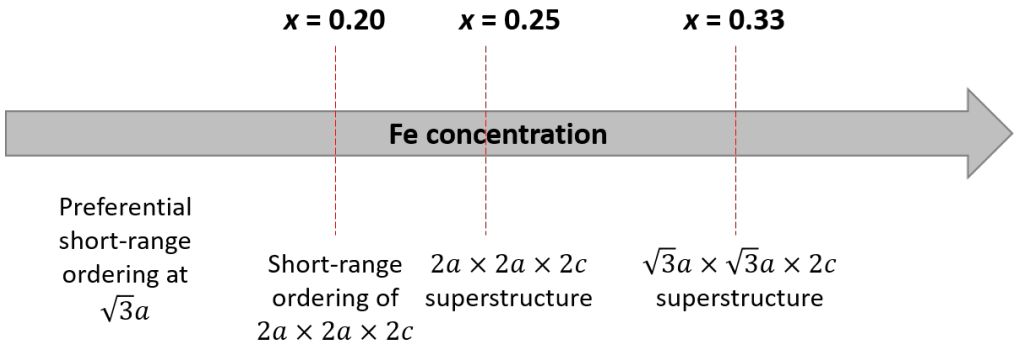

Figure 3.46: Summary on the Fe ordering in Fe_xTiS_2 from the STEM observations.

We think that the Fe ordering in Fe_xTiS_2 can be explained by the Fe interactions within the layers (*ab*-plane) and between the layers (along the *c*-axis). Since the samples were grown using chemical vapor transport method at high temperatures, crystals were grown from bottom-up approach. The vapor species of TiS_2 nucleated on the glass surface and grew in size as more Ti and S species got adsorbed onto the six hexagonal edges of TiS_2 nucleus, forming hexagonal flakes. Fe atoms were then preferentially adsorbed onto the octahedral sites at TiS_2 surface, forming layers of TiS_2 and Fe alternately. In addition, because of the high temperature growth process, Fe atoms could still have sufficient energy to diffuse across the interstitial sites in the structure until the end of the heating cycle and the Fe atoms would rearrange themselves to reach the most energetically stable structure. Thus, at low Fe concentrations ($x \leq 0.15$), the ordering of $\sqrt{3}a$ can be formed preferentially due to the repulsive Fe interaction in the layers alone. In this case, there seems to be

no interlayer Fe interaction, since Fe atom was observed randomly along the c-axis in the cross-sectional ABF images. As the Fe concentration got higher, the attractive Fe interactions between two neighboring layers seems to influence the arrangement of Fe atoms, resulting in $2a \times 2a \times 2c$ superstructure at x = 0.20 and 0.25. At x = 0.33, the Fe atoms had to be closer to each other, resulting in $\sqrt{3}a \times \sqrt{3}a \times 2c$ superstructure

.

CHAPTER 4

Analysis of Superstructure of Fe_xTiS_2 using Transmission Electron Diffraction

4.1. Introduction

During the TEM observation, we also managed to obtain some diffraction patterns showing unique patterns other than the $2a \times 2a \times 2c$ and $\sqrt{3}a \times \sqrt{3}a \times 2c$ superstructure. Single-crystal superstructure patterns are formed by the ordering of the intercalants in the host structure [7]. Previous reports had shown the possibility of the formation of other forms of superstructures during intercalation, aside from the typical $2a \times 2a \times 2c$ and $\sqrt{3}a \times \sqrt{3}a \times 2c$ superstructures. Intercalation of zerovalent metals into Bi_2Se_3 created various forms of superstructures, such as $\sqrt{43}a \times \sqrt{43}a$ for Co intercalates at x = 0.20, $7a \times 7a$ for Ag intercalates at x > 0.50 and $2a \times 2a \times a$ for Cu at x = 0.60 [32].

In this study, transmission electron diffraction (TED) was used to study the ordering of Fe atoms in the observation region. TED is a powerful method that can be used to clarify two-dimensionally periodical structures since the wavelengths of electron are much smaller than those of X-rays. It means that the Ewald sphere for electron diffraction would intersect more reciprocal lattice points in the plane perpendicular to the direction of the incident electron beam, which in turn would give more information on the local structure. Previous studies have shown that the use of TED combined with scanning transmission electron microscopy (STEM) have only reported the finding of $\sqrt{3}a \times \sqrt{3}a$ superstructure reflections in the TED pattern for $0.086 \leq x \leq 0.703$ [5] and intergrowth regions of $2a \times 2a$ at $0 \leq x \leq 0.20$ [25].

The present work reported the capture of a new superstructure for Fe_xTiS_2 using TED and its analysis in determining the planar distribution of intercalated Fe atoms. The projected reflections in the TED were analyzed using Patterson method. Patterson method was first proposed by Arthur Lindo Patterson to replace the structural factors in the electron density function with squared amplitudes whose values are proportional to the diffracted intensities [33]. This would create a map of position vectors between atomic pairs in the structure. This method is more commonly coupled with X-ray diffraction data to identify the positions of atoms. For example, it was used to solve the 3-dimensional structure of the adduct zinc dicyanide-bis(2,9-dimethyl-1,10-phenanthroline) trihydrate [$Zn(CN)_2$.DMP] [34]. The positions of the Zn atoms were determined by applying Patterson method to the XRD data. This method had also been used in combination with TED to identify the atomic configuration of Si(111) 7 × 7 reconstructed surface [35]. In this work, Fourier transformation of the TED patterns were performed to create the Patterson maps. The atomic correlations in this map were then used to reconstruct the surface structure of Si(111). Thus, using similar approach, we used Patterson function to create position vector maps from the TED pattern of Fe_xTiS_2. From that, we then proposed possible atomic arrangements for the intercalated Fe atoms in the van der Waals gap. Lastly, we fitted this Fe atomic arrangement into the TiS_2 host structure and proposed a new local ordering for Fe_xTiS_2, whereby they had units of $\sqrt{43}a \times \sqrt{43}a$, $\sqrt{31}a \times \sqrt{31}a$ and $\sqrt{7}a \times \sqrt{7}a$.

4.2. Methodology

4.2.1. Synthesis of Fe_xTiS_2 crystals

Credits given to Abe Satoshi from Koyano lab in preparing the Fe_xTiS_2 crystals at $x = 0.33$ using a lower amount of raw materials for this experiment. The crystals were grown using chemical vapor transport technique with iodine (I_2) as transport gas. The raw materials used are in powder form and the information of each material used is as shown in Table 4.1. The amount of powder used was based on the assumptions that Fe + Ti + S = 2g and the I_2 flow was 10 mg/cm^3 in the sealed quartz tube.

Table 4.1: Information of the raw materials used.

Chemical Name	Purity / %	Manufacture	Lot No.
I_2	99.9	Wako	096-03122
S	99.99	Kojundo Chemical	4084561
Ti	99.99	Rare Metallic	10221-70
Fe	99.99	Rare Metallic	90209-63-71

These powdered raw materials were put in the order of I_2, S, Fe and Ti into the quartz tube before being sealed under a vacuum of 2.5×10^{-6} Torr using oxy-fuel torch. Once the quartz tube cooled off, the powders were shaken well to ensure uniform mixing and tilted slightly to make a powder slope. The higher slope side was then placed first into a tube furnace (Koyo KTF040N1), 13.3 cm from the right side of tube furnace, such that it was under the higher temperature region of 950°C and the lower slope side was at the lower temperature region of 920°C, as shown in Figure 4.1.

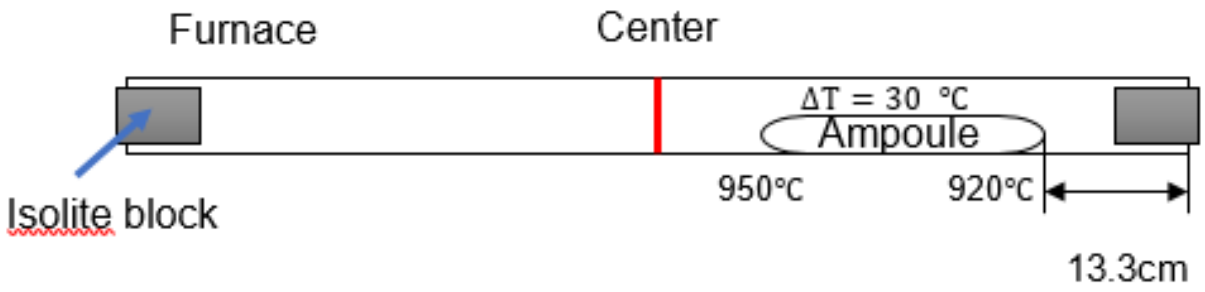

Figure 4.1: Setup in tube furnace.

The heating profile of the tube furnace is as shown in Figure 4.2. The quartz tube was heated slowly up to 950°C and maintained for one week. Lastly, the samples were collected after the one-week heating period.

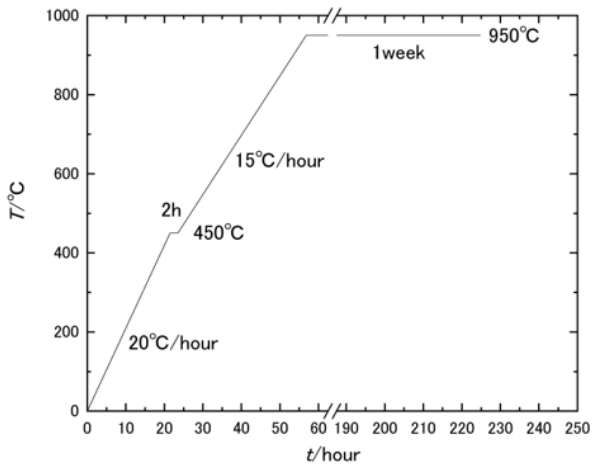

Figure 4.2: Heating profile of quartz tube in tube furnace.

4.2.2. TEM Characterization

The Fe_xTiS_2 single crystals grown had hexagonal shapes with average sizes of 1 mm in diameter. Each crystal was then crushed using tweezers to break into smaller pieces and immersed

in absolute ethanol solution. The solution was then subjected to ultrasonication for 10 minutes to further breakdown the size of specimens. The ultrasonicated solution was then left for one minute to ensure all the big pieces of specimen were deposited at the bottom of the solution bottle. A few drops of the solution near the solution surface were then dripped onto a 7nm-carbon coated copper TEM grid. The TEM grid was then left to dry and kept in vacuum storage before TEM observation.

TEM observation was performed using JEOL JEM-ARM200F at 120 kV and 200 kV. This TEM system is equipped with energy-dispersive spectroscopy (EDX) detector, which was used in this experiment to identify the composition of Fe_xTiS_2. In this experiment, imaging modes of bright field TEM and selected area electron diffraction (SAED) were used to capture the bright field images and transmission electron diffraction pattern of the observed areas..

4.2.3. Construction of Patterson map to determine Fe distribution

As mentioned in Introduction, phase information is missing in any diffraction experiment. Diffraction spots only provide amplitude of the corresponding structure factor but not its phase, which provides information on the atomic positions. However, the Patterson function remedies this by replacing the amplitude in the electron density function with a squared amplitude and assume all the phases are 0. This will remove the unknown phase information from the electron density function and provide the Patterson function, as defined below:

$$\mathrm{P}(x, y) = \sum_{h,k} I_{h,k} \exp(-2\pi i(hx + ky))$$

where x and y are the atomic coordinates of the atoms, h and k are the Miller indices in reciprocal space.

This function is basically the Fourier transform of the intensities, rather than the structure factors, giving maximum peaks that correspond to positional vectors between atomic pairs in the structure. The intensities of these maximum peaks are proportional to the product of atomic numbers. The heavier the atoms in the atomic pair, the higher the intensities. So, this makes Patterson function useful in the identification of the position of heavy atoms and subsequently the positions of other lighter atoms, provided that a basic structural knowledge is known about the structure. The atomic arrangement is deduced based on this basic structural knowledge. For example, information on the space group will be useful in identifying the structure. However, Patterson method assumes that electrons and X-rays is only scattered once within the sample (kinematical approximation). In fact, it is necessary to pay attention to the fact that the intensity of each index changes depending on the thickness because electrons will experience multiple scattering within the sample at larger sample thickness (dynamical theory). Therefore, we need to verify the effectiveness of this method and then apply it to the experimental results.

4.2.4. TED Simulations

Based on kinematical approximation, simulated TED pattern can be obtained for the squared values of the structure factor function, which is obtained by the proposed atomic structure model. The structure factor is expressed by

$$\mathrm{F}_{hkl} = \sum_{j=1}^{N} f_{j,(hkl)} exp\{-2\pi i(hx_j + ky_j + lz_j\}$$

where x_j, y_j and z_j are the atomic coordinates of the j-th atom and f_j is the scattering factor of the j-th atom. However, when the sample thickness increases, the intensity at each index in the TED pattern changes depending on the thickness due to multiple scattering within the sample.

4.3. Results and Discussion

4.3.1. Patterson Analysis of TED Pattern with $\sqrt{43}a \times \sqrt{43}a$ Superstructure

Figure 4.3(a) shows a bright field TEM image of a fragment of the Fe_xTiS_2 structure. At different regions of this specimen, different TED patterns were observed. At region A, the specimen was only observed with fundamental reflections of TiS_2, with b_1 and b_2 as the reciprocal lattice vectors (Figure 4.3(b)). However, at other regions of B, C and D, the TED patterns (Figure 4.3(c)-(e)) showed fractional order reflections with the fundamental reflections of TiS_2. The additional reflections could not have been caused by overlapping of multiple crystals since the bright field TEM image showed only one fragment. In addition, the TED patterns showed that six fractional order reflections formed hexagonal pattern around the origin as indicated by the light blue hexagon. Therefore, the fractional order reflections correspond to the superstructure reflections were observed to be rotated from the fundamental TiS_2 reflections at an angle of approximately 8°. We found that such hexagonal patterns were observed around some fundamental reflections in the TED patterns at regions B, C and D. These TED patterns are so similar that they showed pronounced fractional order reflections at almost the same positons.

The TED patterns obtained at regions A, B, C and D are hereinafter named as TED A, TED B, TED C and TED D, respectively. The incident beam appears to be slightly tilted in different directions from the [001] direction, since the intensity distributions of the six equivalent {120}

reflections are slightly different from each other among TED B, C and D. Also, due to the thicker region at B, stronger fundamental reflections were observed, as compared to TED C and D. Comparing just the superstructure reflections, all TED patterns have similar positions, thus indicating that the superstructure is intrinsically formed.

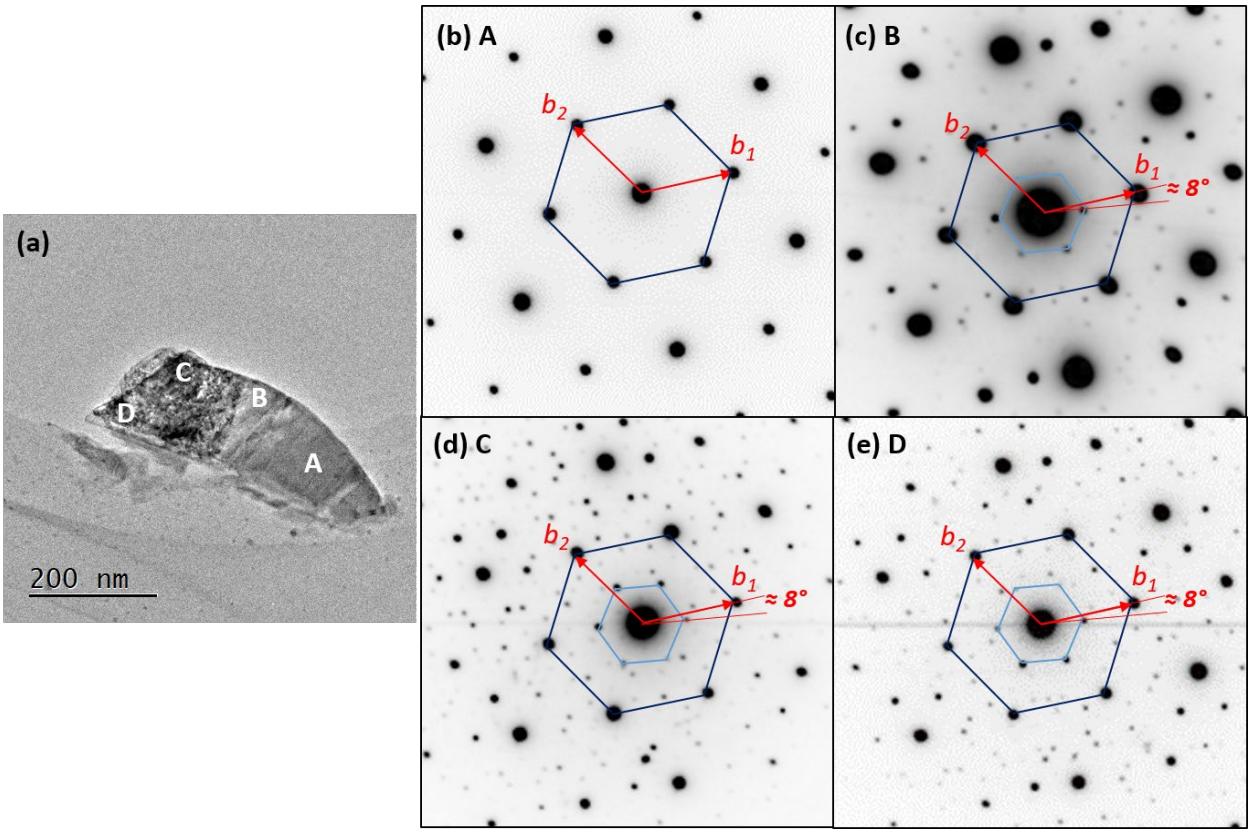

Figure 4.3: (a) Bright field TEM image of a fragment of the Fe_xTiS_2 specimen. (b) – (e) show the corresponding TED patterns at regions A, B, C and D. The dark blue hexagon indicates the fundamental reflections of host structure TiS_2 and the light blue hexagon are formed by additional reflections. At region A, only fundamental reflections of TiS_2 host structure were observed. At regions B, C and D, additional reflections were observed, forming smaller partial hexagons that are rotated at an angle of about 8°. The partial hexagon had different intensities due to different tilting angles of the beam, as indicated by the uneven intensities of the six equivalent {120} reflections along the edges of the dark blue hexagon.

EDX analysis was also performed on parts of this specimen. The resulting EDX mapping and its quantification results are as shown in Figure 4.4. Fe atoms are shown to be distributed uniformly in the observed region. The Fe to Ti atomic ratio was 0.26, which was lower than the growth nominal content of 0.33. It suggests that Fe atoms may be distributed non-uniform and Fe concertation may be fluctuated among fragments.

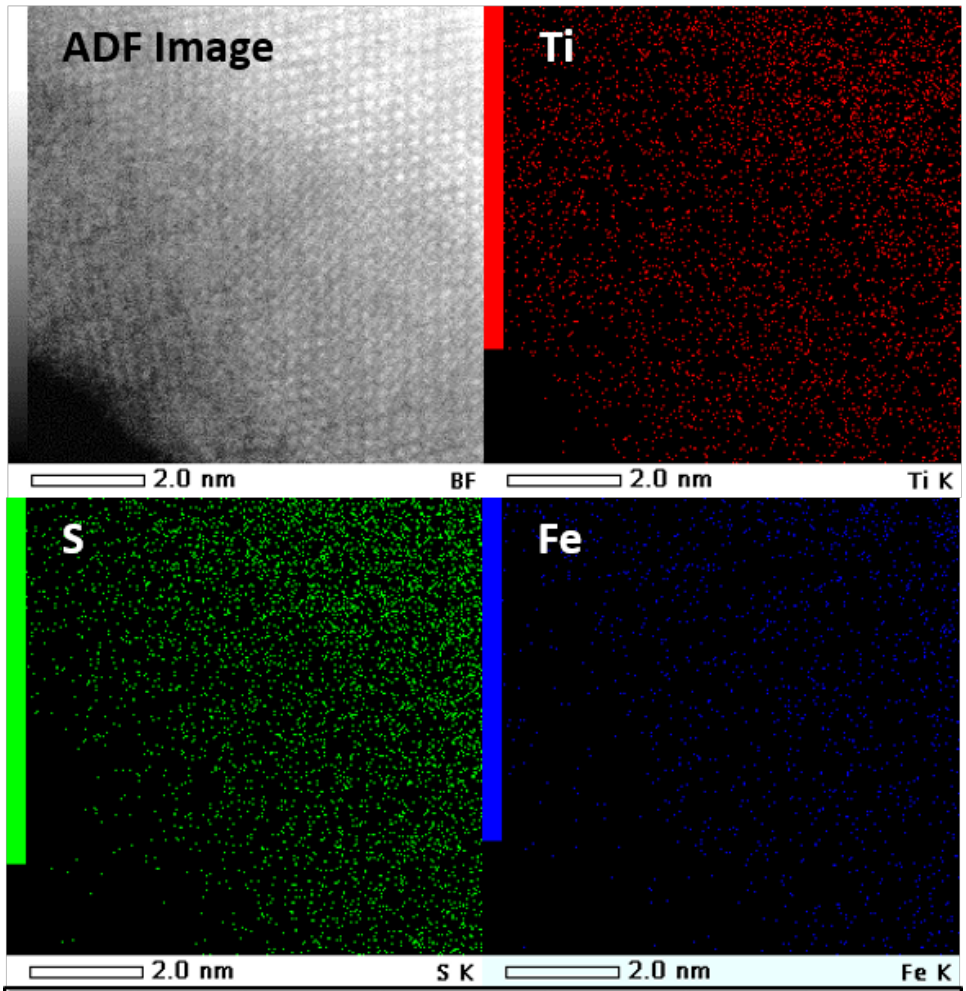

Ele...	Cl...	(keV)	Counts	Mass%	Sigma	Atom%
S K	Ref.	2.307	4590.75	40.07	0.28	50.80
Ti K		4.508	4529.04	45.94	0.34	39.02
Fe K		6.398	1149.63	13.99	0.22	10.18
Total				100.00		100.00

Figure 4.4: EDS mapping and quantification of the specimen at region D.

Figure 4.5 shows (full) Patterson maps for TED C and D. The vectors from the origin to each dark peak in the Patterson maps correspond to the atomic correlation between Ti-Ti, Ti-S, Fe-Fe, Fe-S or Fe-Ti atoms. The unit vector of TiS_2 is labelled as a_1 and a_2. The Patterson maps had six-fold symmetry such that six blue triangles showed the same pattern as shown in Figs. 4.5(a) and 4.5(b). The dark blue hexagon corresponds to the TiS_2 structure, while the light blue hexagon corresponds to the superstructure. This superstructure was found to have the unit vector of $7a_1 - a_2$ or $a_1 + 6a_2$ which directions were tilted by about 8° from the unit vector of the TiS_2 unit cell. The calculated unit length for the superstructure was $\sqrt{43}a \times \sqrt{43}a$, where a is the length of the unit vector in the TiS_2 host structure. The Patterson map for TED B is not shown here because no useful information could be obtained from it due to the strong intensities of the fundamental spots in TED B. The atomic correlations between the atoms in the host structure would predominate.

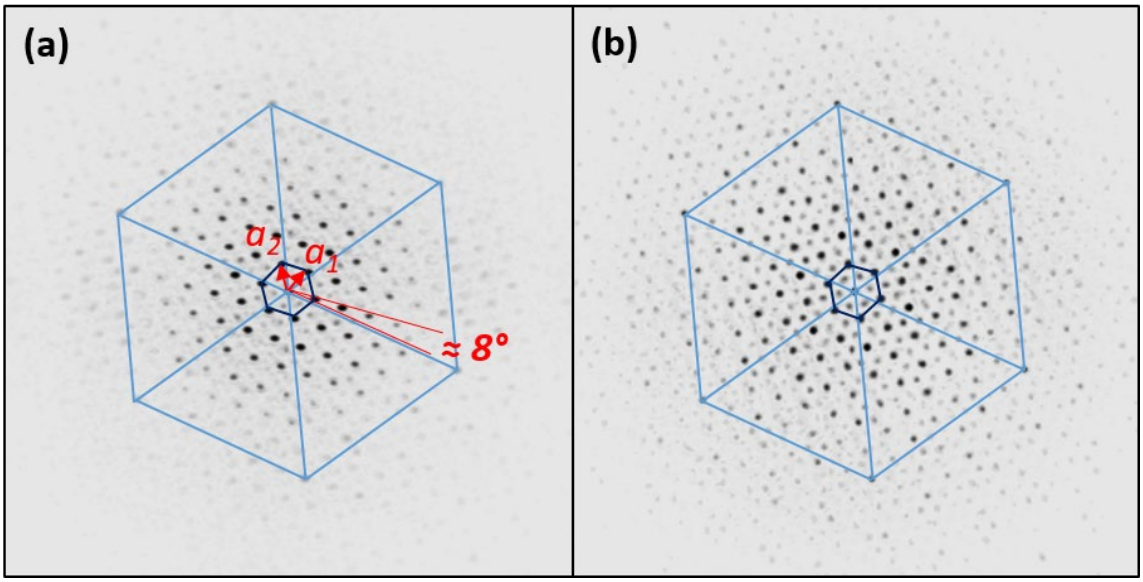

Figure 4.5: Patterson maps of (a) TED C and (b) TED D.

Since the superstructure reflections correspond to the periodicity caused by intercalated Fe atoms, they are extracted (Figure 4.6) and used to construct the partial Patterson map (Figure 4.7). The atomic correlations in the partial Patterson map then show the Fe-Fe relationship. However, the atomic correlations are not limited to the same layer, the map shows those projected along the *c*-axis direction. It means that there is a possibility that the corresponding superstructure is composed of multiple layers.

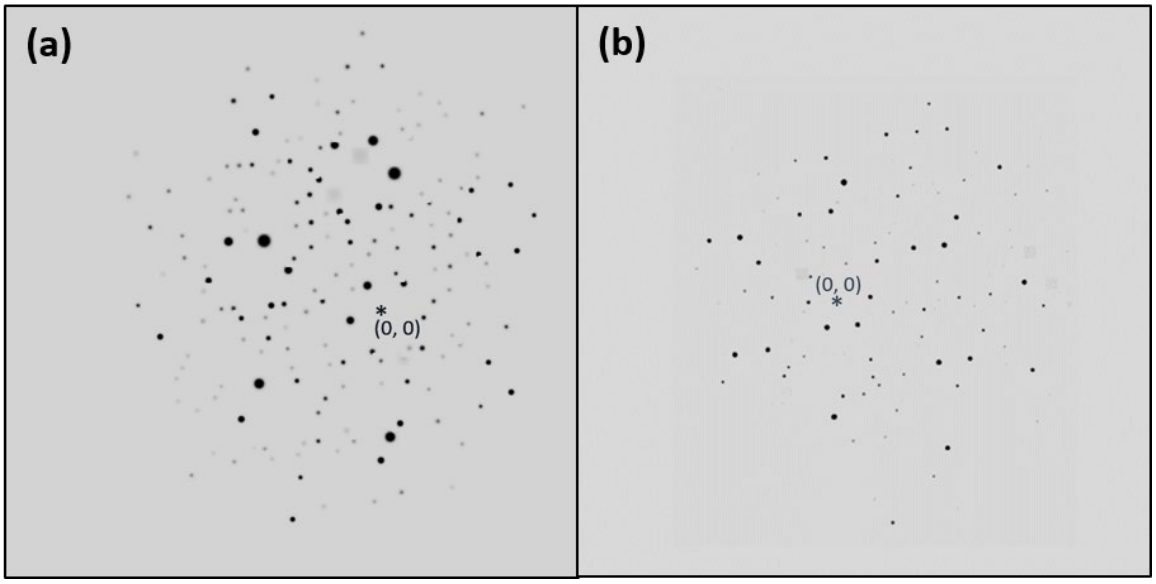

Figure 4.6: Extracted superstructure reflections from (a) TED C and (b) TED D. The center of the beam is indicated by the asterisk sign.

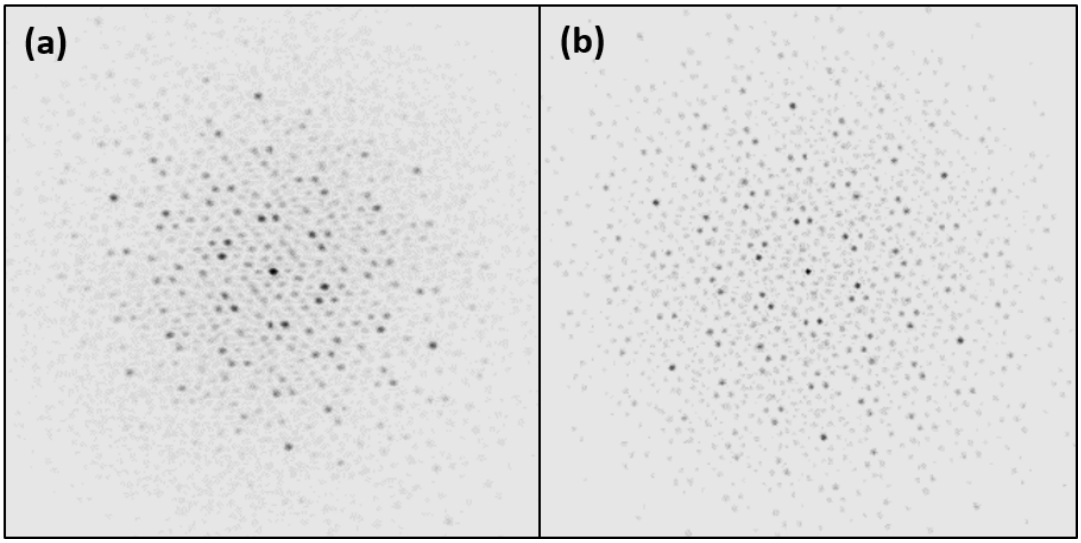

Figure 4.7: (a) Partial Patterson map of the extracted superstructure reflections of TED C and (b) partial Patterson map for extracted superstructure reflections of TED D.

Both partial Patterson maps from TED C and D showed the same peaks. It suggests that both regions have the same superstructure constructed by intercalated Fe atoms. So, in subsequent sections, we focus on one Patterson map.

The 6-fold symmetry in the Patterson map meant that the atomic structure would belong to the space group family of P3 or P6. And, in one of six equivalent triangle indicated by blue line, 12 peaks corresponding to 12 atomic correlations were found as shown in Figure 4.8(b), which enabled us to deduce the atomic arrangement of Fe atoms. The atomic correlations of 12 peaks are summarized in Table 4.2. Taking symmetry into account, these 12 peaks have another two equivalent correlations.

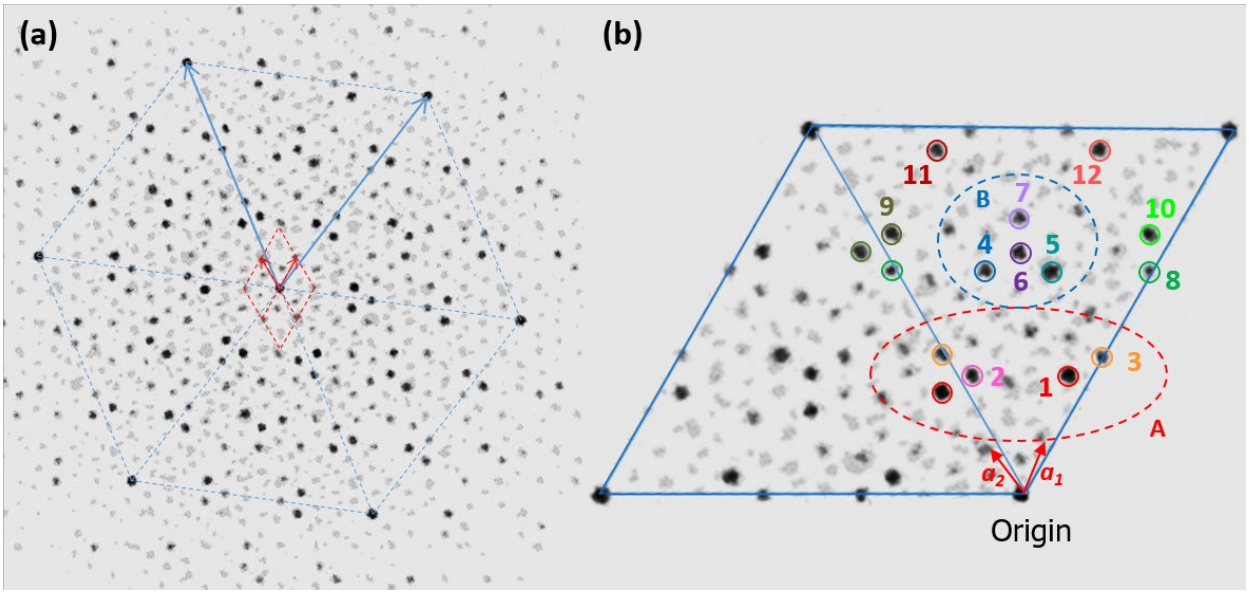

Figure 4.8: (a) The Patterson map shows 6-fold symmetry, as indicated by the triangular sections in the hexagon and (b) The main Patterson peaks in the enlarged Patterson map.

Table 4.2: Patterson peak positions and atomic correlations between peaks in Patterson map.

Peak	**position [u, v]**	**Other equivalent positions [-v, u+v] [-(u+v), u]**	**Length (× a)**
1	[2,0]	[0, 2], [-2, 2]	2
2	[2/3, 5/3]	[-5/3, 7/3], [-7/3, 2/3]	2.08
3	[8/3, -1/3]	[1/3, 7/3], [-7/3, 8/3]	2.52
4	[2, 2]	[-2, 4], [-4, 2]	$2\sqrt{3}$ (=3.46)
5	[3, 1]	[-1, 4], [-4, 3]	$\sqrt{13}$ (=3.61)
6	[8/3, 5/3]	[-5/3, 13/3], [-13/3, 8/3]	3.79
7	[3, 2]	[-2, 5], [-5, 3]	$\sqrt{19}$ (=4.36)
8	[13/3, -2/3]	[2/3, 11/3], [-11/3, 13/3]	4.04
9	[14/3, -1/3]	[1/3, 13/3], [-13/3, 14/3]	4.51
10	[1, 4]	[-4, 5], [-5, 1]	$\sqrt{21}$ (=4.58)
11	[8/3, 11/3]	[-11/3, 19/3], [-19/3, 8/3]	5.51
12	[5, 1]	[-1, 5], [-6, 5]	$\sqrt{31}$ (=5.57)

By taking these 12 atomic correlations into account, a suitable arrangement of intercalated Fe atoms was constructed, as shown in Figure 4.9. Black bold diamond corresponds to the unit cell of the superstructure. In this configuration, the Fe atoms at the edges of the superstructure unit cell has six-fold symmetry with the surrounding 6 Fe atoms, as indicated by P6 symmetry in Patterson map. Next, we considered the first nearest Patterson peaks 1, 2 and 3 indicated by group A in Fig. 4.8. These vectors matched well the atomic pairs in Figure 4.10(a), with red lines corresponding to peak 1 in the Patterson map of Figure 4.8(b), pink lines to peak 2 and orange lines to peak 3. The Patterson peaks 4, 5, 6 and 7 indicated by group B could be explained by the atomic pairs in Figure 4.10(b), (c) and (d), where blue lines correspond to peak 4, green lines to peak 5, dark purple lines to peak 6 and light purple lines to peak 7. It means that the proposed arrangement of Fe atoms matched well with the 12 peaks in Patterson map. However, it is unknown if each atom is in the same layer because the TED patterns provide only two-dimensional information that is a projection of the arrangement of Fe atoms perpendicular to the electron incident direction. It means that the number of inserted Fe layers needed to form the three-dimensional superstructure is unknown.

To confirm the number of Fe layers, the proposed model was also compared with the nominal content and EDS content. So, for this model, we identified that there were 9 Fe atoms in the $\sqrt{43}a \times \sqrt{43}a$ superstructure. If the superstructure is consisted of only a layer of Fe atoms, the calculated Fe concentration is then 0.21, which is lower than nominal growth content of $x = 0.33$. If there were two layers, the Fe concentration becomes even lower and this seems less probable. Thus, we decided that the superstructure consists of a single intercalated Fe layer.

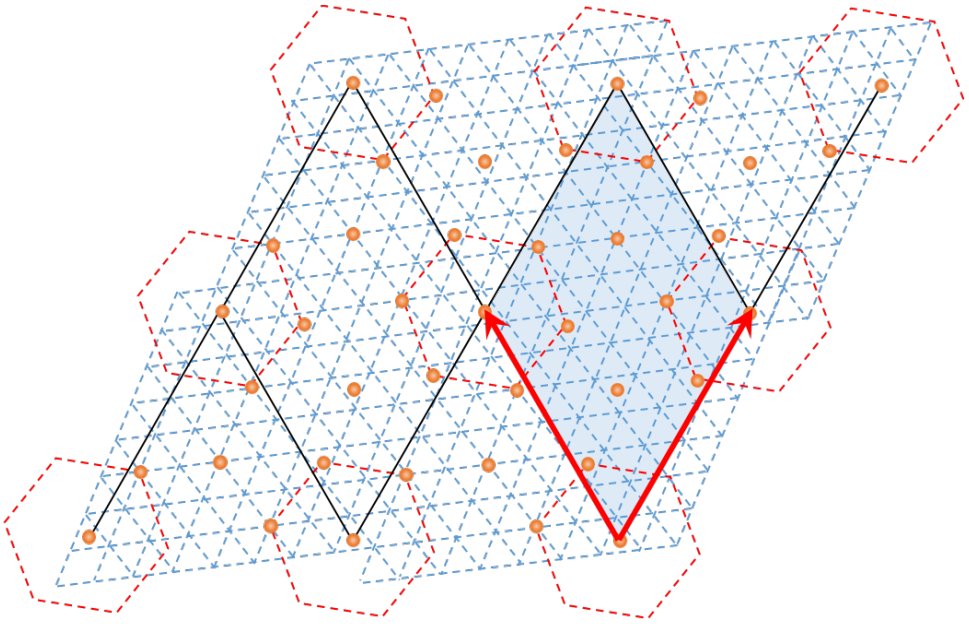

Figure 4.9: Structural model of superstructure formed by intercalated Fe atoms constructed with the basic lattice vectors of $7a_1 - a_2$ and $a_1 + 6a_2$.

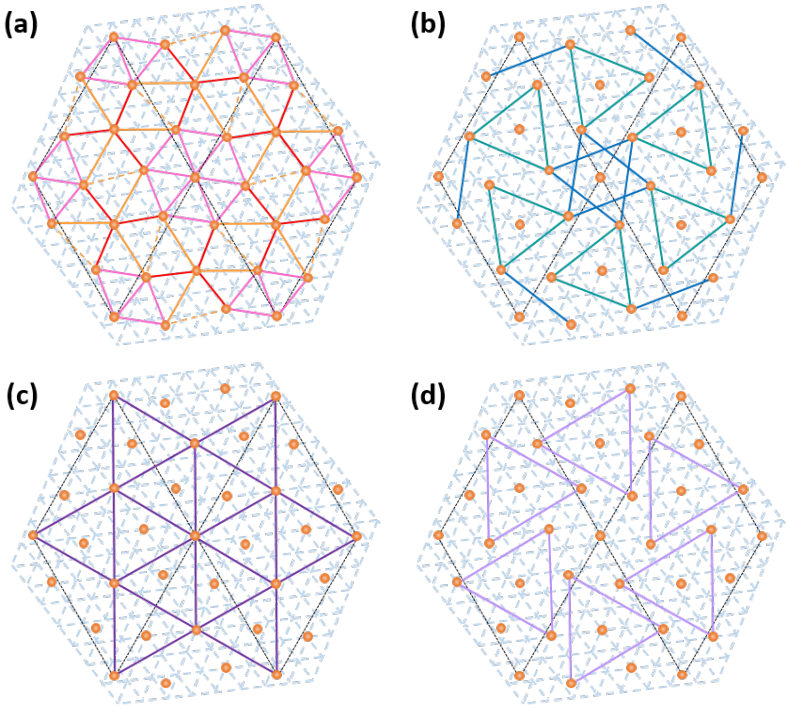

Figure 4.10: (a) Fe atomic correlations that fit the Patterson peaks 1, 2, 3 in group A, (b) Fe correlations that fit the Patterson peaks 4 and 5, (c) Fe correlations that fit the Patterson peak 6 and (d) Fe correlations that fit the Patterson peak 7.

The Fe layer was then overlapped with the TiS_2 host structure. There are three possibilities for the arrangement of 9 Fe atoms and the host structure. The 9 Fe atoms can be at the site of Ti or S site. The most possible site was then determined based on the assumption that most Fe atoms would occupy octahedral sites at Ti sites, as shown in Figure 4.11. Fe atoms at the edges of the superstructure cell are located at the (1/3, 1/3) S sites. In this stacking sequence, 9 Fe atoms are located at both Ti sites and S sites. Fe atoms at Ti sites form octahedral coordination with six surrounding S atoms, whereas Fe atoms at S sites form tetrahedral coordination with four S surrounding atoms. This is different from previous studies, which reported that intercalates would always preferentially occupy octahedral sites in TiS_2 [36]. However, during STEM observation, we sometimes observed darker contrast at the S sites in the ABF image as shown in Figure 4.11(b), suggesting the presence of Fe atoms at the S atomic columns.

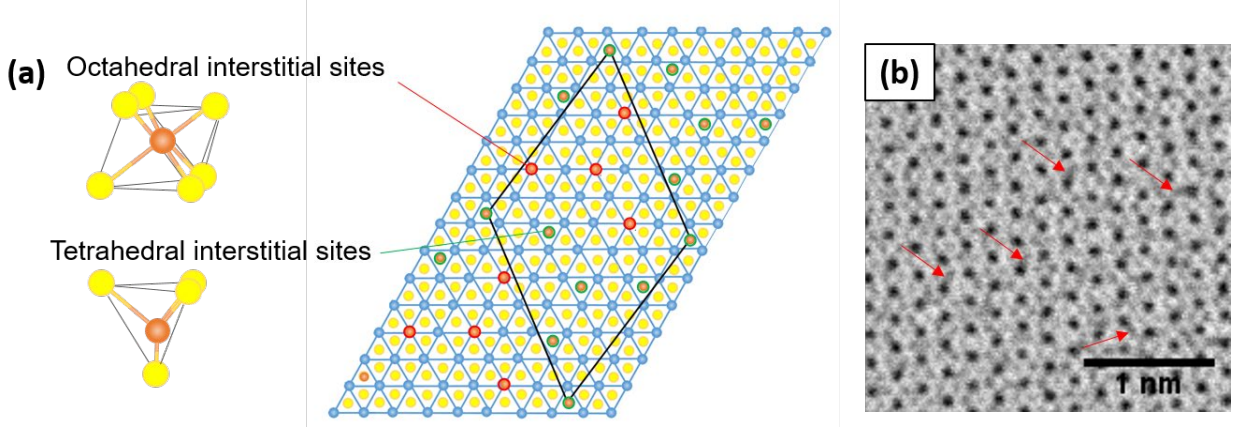

Figure 4.11: (a) Fe-TiS_2 layers configuration with Fe occupying both tetrahedral (green circles) and octahedral (red circles) coordinated sites. (b) STEM imaging showing the presence of Fe atoms at S sites, confirming occupation of Fe atoms at tetrahedral sites.

The experimental TED pattern was then compared with the simulated one obtained using the proposed superstructure based on kinematical approximation (the incident electron is scattered

only once by the sample) to confirm the reliability of our analysis. In the experimental TED pattern of Fig. 4.12(b), we found two repeating patterns of hexagon and triangle, as indicated by blue and green dashed-lines, respectively, appearing around the fundamental reflections of the host TiS_2 structure. Also, the intensities of these 6 and 3 equivalent reflections were not uniform with one spot always showing stronger intensity. The simulated TED pattern as shown in Figure 4.12(a) shows similar intensity distribution of the superstructure reflections with the experimental one, although some reflections had different intensities due to dynamical scattering in actual specimen.

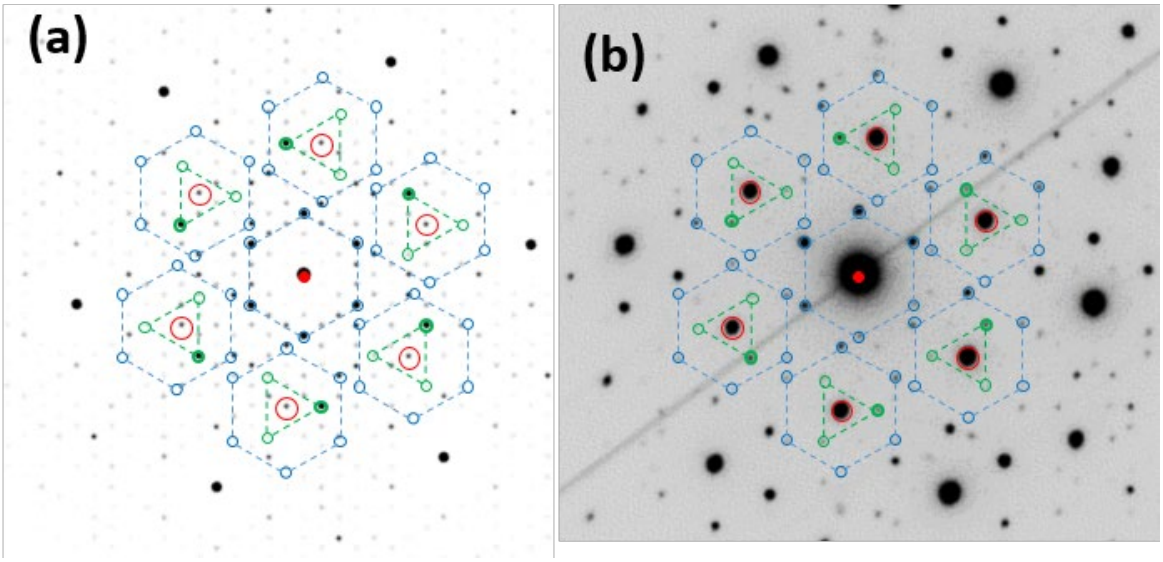

Figure 4.12: Comparison of (a) Experimental TED pattern and the simulated TED pattern.

4.3.2. Patterson Analysis of TED Pattern with $\sqrt{31}a \times \sqrt{31}a$ Superstructure

While getting the STEM imaging of the crystals at different Fe concentrations, some unique TED patterns were found at $x = 0.20$, aside from the short-range $2a \times 2a \times 2c$. Figure 4.13 shows the bright field TEM image and its corresponding SAED pattern. Superstructure reflections were found, forming rotated hexagonal pattern at an angle of approximately 9°.

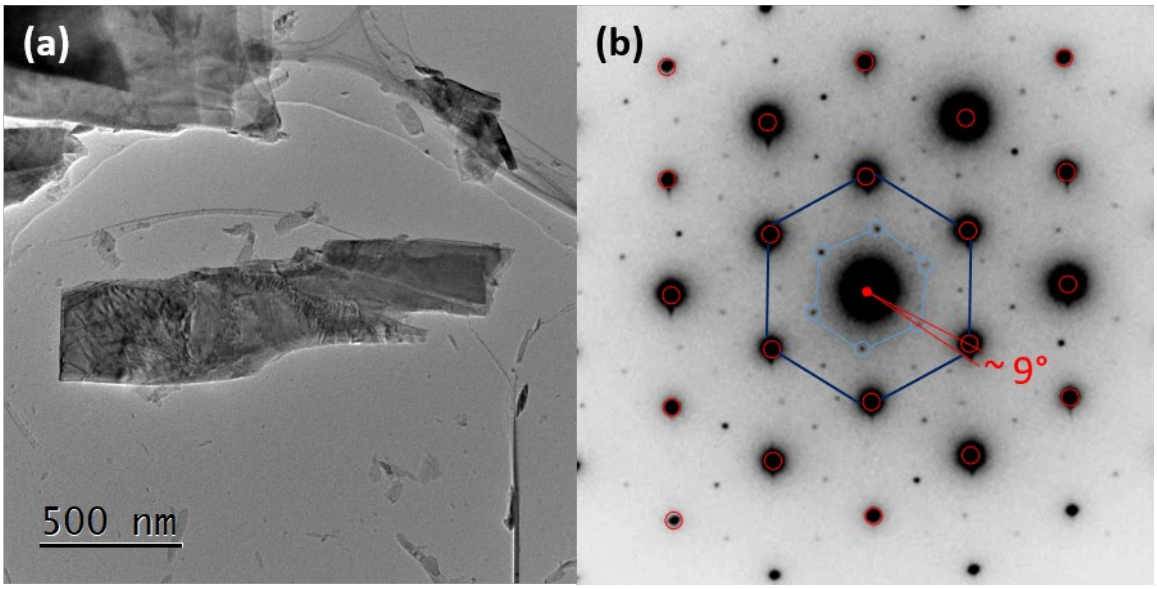

Figure 4.13: (a) Bright field TEM image of a crystal fragment that a unique superstructure TED pattern in (b).

Samples were grown with the nominal content of $x = 0.20$ but EDS measurement showed that the observation region consisted of a higher Fe content at $x = 0.24$, as shown in Figure 4.14. So this might have attributed to the different arrangement of Fe atoms in this fragment.

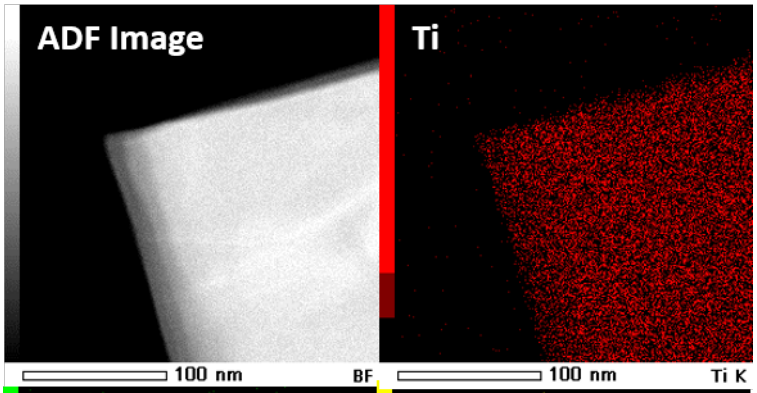

Ele...	Cl...	(keV)	Counts	Mass%	Sigma	Atom%
S K	Ref.	2.307	1908.82	48.17	1.53	58.89
Ti K		4.508	1318.20	40.36	1.60	33.05
Fe K		6.398	303.50	11.47	0.95	8.06
Total				100.00		100.00

Figure 4.14: EDS results of part of the crystal fragment in which superstructure reflections were observed.

Full Patterson map in Figure 4.15(a) shows that the superstructure had a unit size of $a_1 + 5a_2$ and $6a_1 - a_2$ with the calculated unit length of $\sqrt{31}a$. Then, by inverse Fourier transformation of the pattern consisting of the superstructure reflections only, partial Patterson map was obtained as shown in Figure 4.15(b), which shows 6-fold symmetry. In each fragment, there were 9 repeating peaks, as shown in Figure 4.16 and the positions of each peak are shown in Table 4.3.

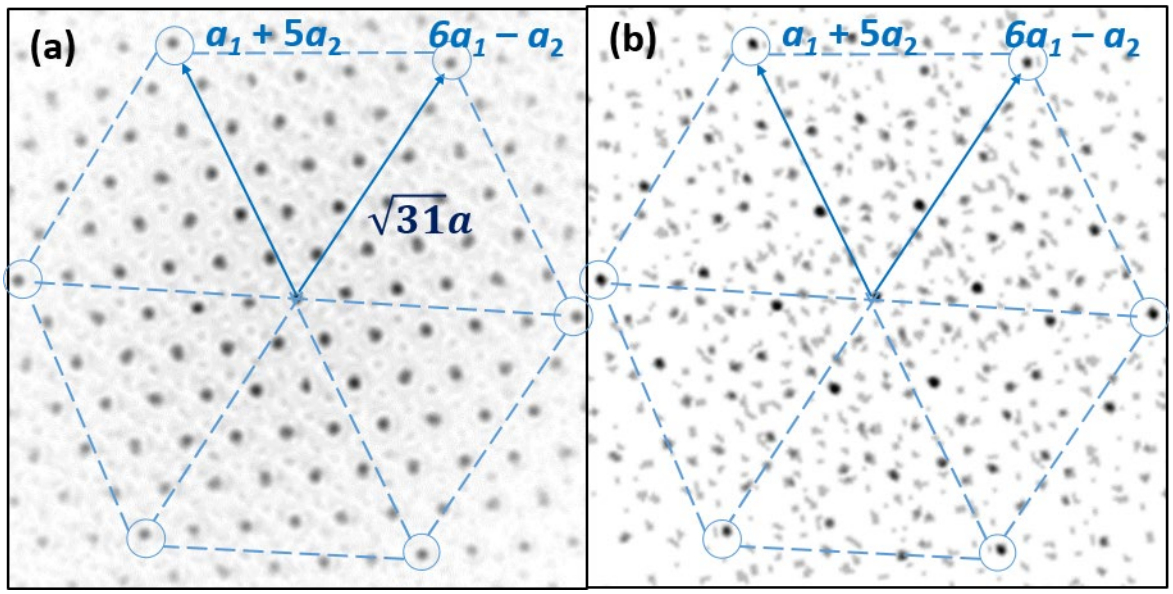

Figure 4.15: (a) Full Patterson map of the TED pattern showing a superstructure with unit size of $a_1 + 5a_2$ and $6a_1 - a_2$, and calculated unit length of $\sqrt{31}a$. (b) Partial Patterson map of the superstructure reflections in the TED pattern showing 6-fold symmetry.

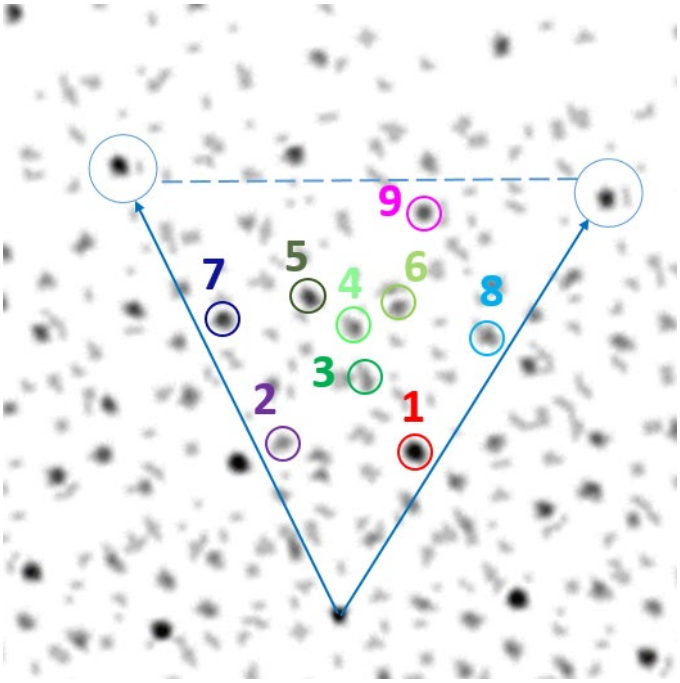

Figure 4.16: Enlarged fragment of the partial Patterson map, showing 9 main peaks.

Table 4.3 Patterson peak positions and atomic correlations between peaks in Patterson map.

Peak	**position [u, v]**	**Other equivalent positions [-v, u+v] [-(u+v), u]**	**Length (× a)**
1	[2,0]	[0, 2], [-2, 2]	2
2	[2/3, 5/3]	[-5/3, 7/3], [-7/3, 2/3]	2.08
3	[2, 1]	[-1, 3], [-3, 2]	2.65
4	[7/3, 4/3]	[-4/3, 11/3], [-11/3, 7/3]	3.21
5	[2, 2]	[-2, 4], [-4, 2]	$2\sqrt{3}$ (=3.46)
6	[3, 1]	[-1, 4], [-4, 3]	$\sqrt{13}$ (=3.61)
7	[1, 3]	[-3, 4], [-4, 1]	$\sqrt{13}$ (=3.61)
8	[11/3, -1/3]	[1/3, 11/3], [-10/3, 11/3]	3.51
9	[4, 1]	[-1, 5], [5, 4]	4.58

From the atomic correlations in partial Patterson map, the possible arrangement of Fe atoms was proposed, as shown in Figure 4.17. Fe atoms were almost evenly distributed, with 9 Fe atoms in the superstructure. This proposed structure explains the atomic correlations, as shown in Figure 4.18(b)-(f). Since the number of Fe atoms is 9 in the $\sqrt{31}a \times \sqrt{31}a$ unit cell, the calculated Fe concertation is 0.29, which is higher than the nominal concentration of 0.2. So, the superstructure model we proposed only had one Fe layer because if the superstructure was consisted of two Fe layers, the calculated concentration would then be halved and this was not reasonable since EDS analysis showed Fe concentration of 0.24. Fig. 4.19(a) shows our proposed superstructure, with the Fe atoms located at both octahedral and tetrahedral sites, similar to the $\sqrt{43}a \times \sqrt{43}a$ superstructure.

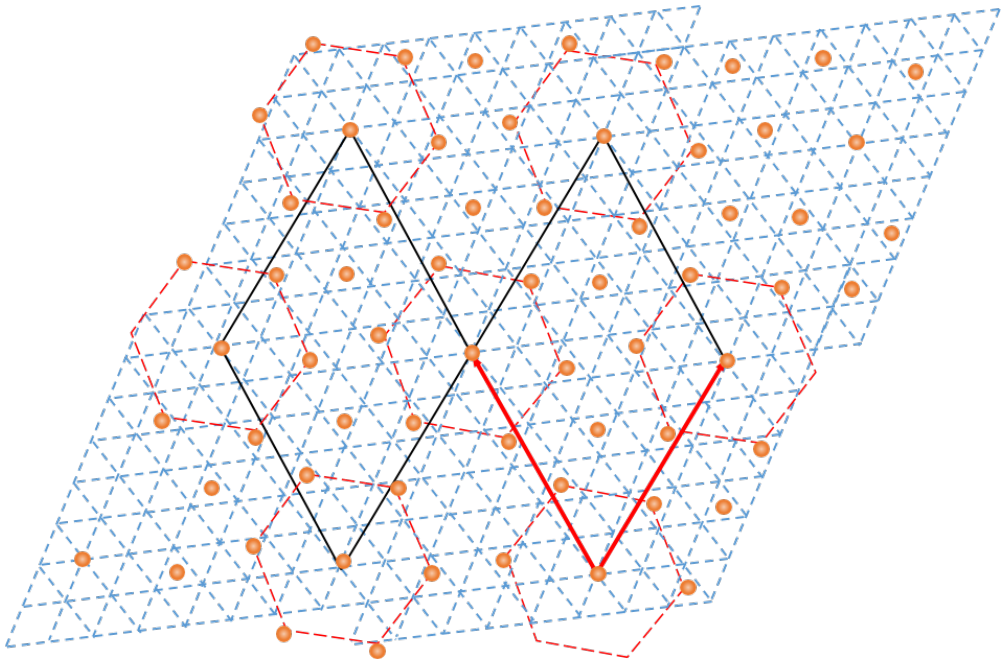

Figure 4.17: Proposed atomic model for the $\sqrt{31}a \times \sqrt{31}a$ superstructure.

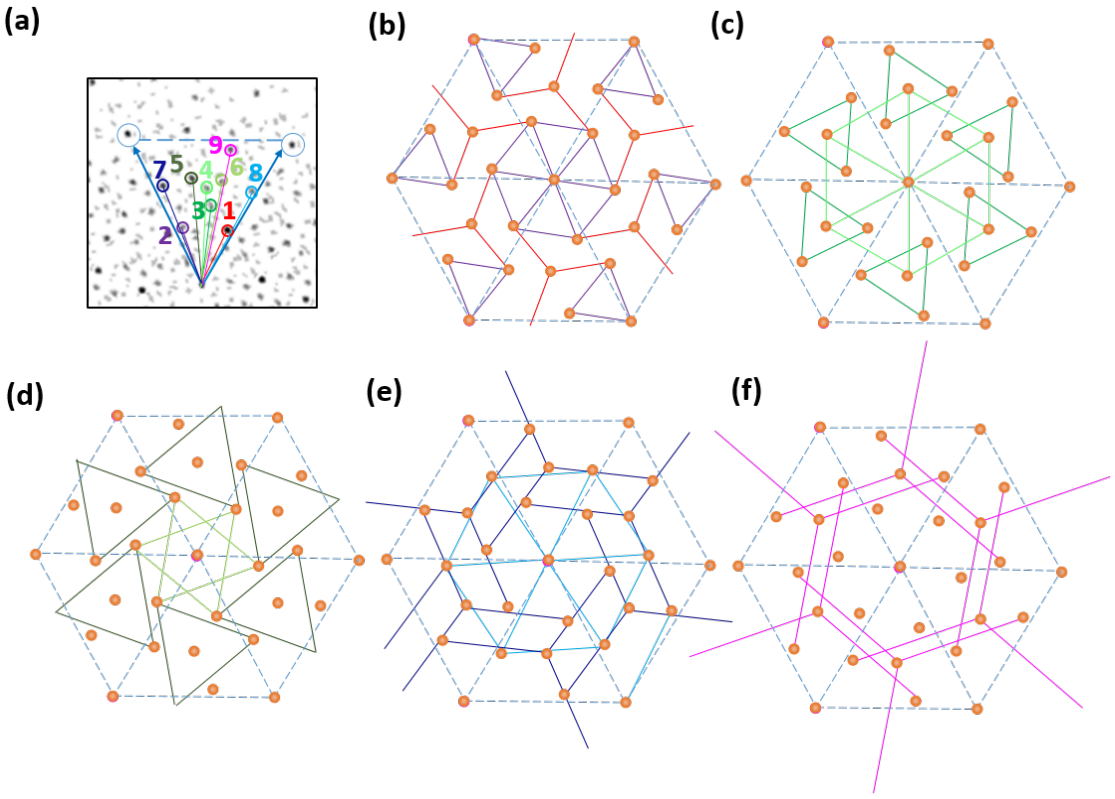

Figure 4.18: (a) Repeating unit in the partial Patterson map showing 9 Fe peaks. (b)-(f) Fe atomic correlations that fit the distances of the peaks from the origin for each peak.

The experimental TED pattern was compared with the simulated one, which was obtained using our proposed superstructure (Figure 4.19(a)) to confirm the reliability of our analysis. In the experimental TED pattern (Figure 4.19(c)), we found that two sets of 6 equivalent superstructure reflections, as indicated by blue and green dashed-lines around the fundamental reflections of the TiS_2 host structure. The simulated TED pattern as shown in Figure 4.19(b) shows similar intensity distribution of the superstructure reflections with the experimental one, although some reflections had different intensities due to dynamical scattering in actual specimen, thus confirming our model.

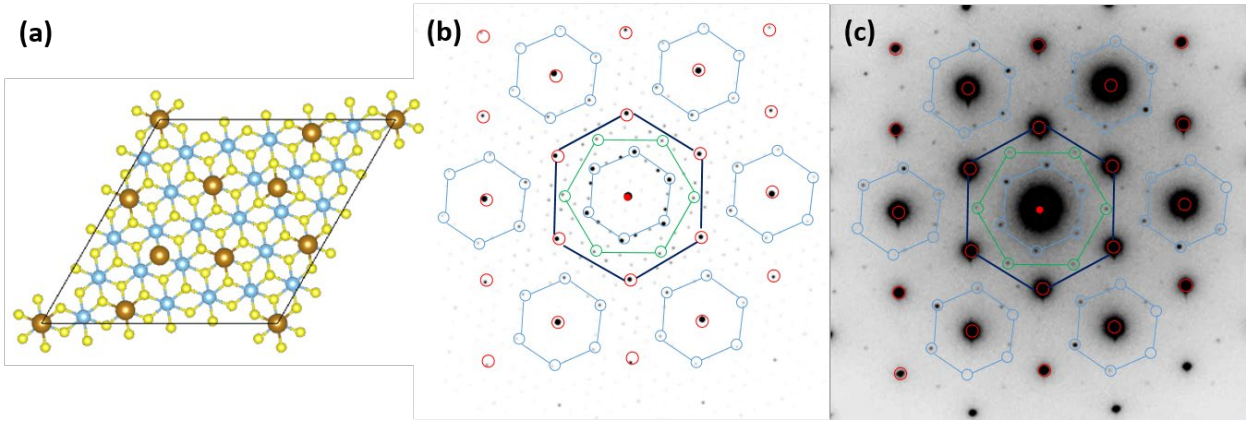

Figure 4.19: (a) $\sqrt{31}a \times \sqrt{31}a$ atomic model used for TED simulation with 9 Fe atoms in the model. (b) The reflection positions in the simulated TED matched well with the experimental TED in (c).

4.3.3. Patterson Analysis of TED Pattern with $\sqrt{7}\boldsymbol{a} \times \sqrt{7}\boldsymbol{a}$ Superstructure

In another crystal fragment (Figure 4.20(a)) which was also grown at $x = 0.20$, a different TED pattern was obtained as shown in Figure 4.20(b). Similarly, the superstructure reflections were rotated from the fundamental TiS_2 reflections, but in this case at an angle of approximately 19°.

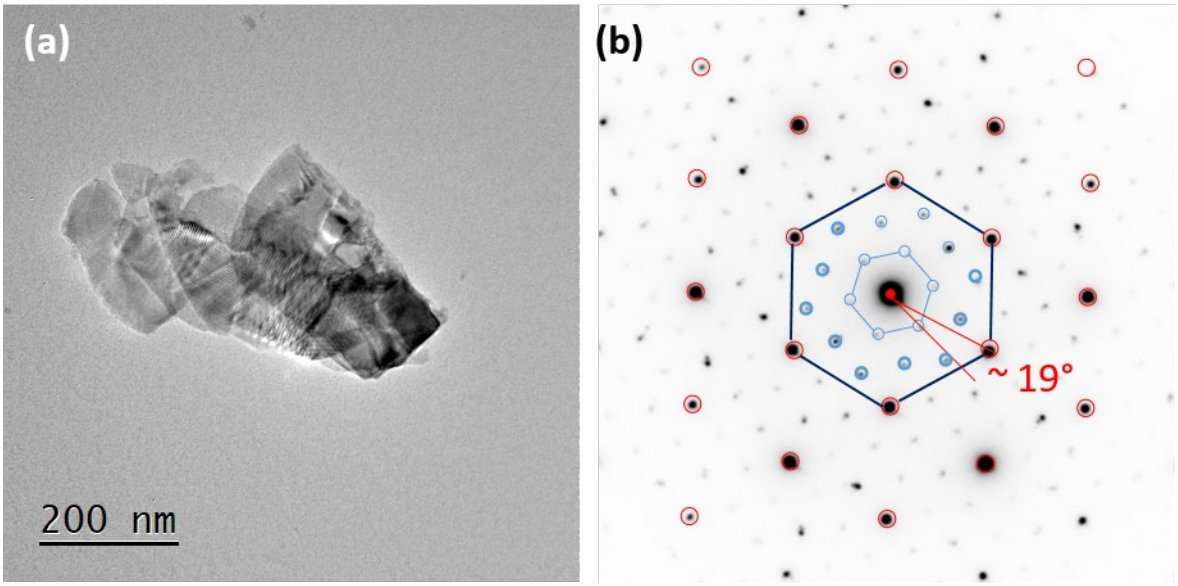

Figure 4.20: (a) Bright field TEM image of a crystal fragment that a unique superstructure TED pattern in (b).

EDS measurement showed that this crystal fragment had a slightly different Fe concentration of $x = 0.21$, as compared to the growth nominal content of $x = 0.20$, as shown in Figure 4.21. So this might have attributed to the different arrangement of Fe atoms in this fragment.

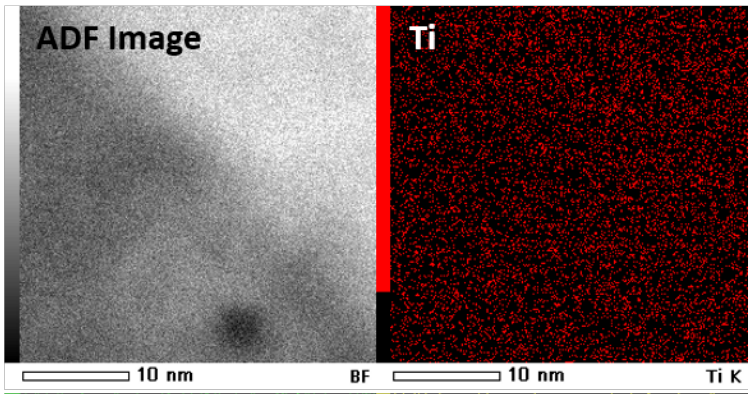

Ele...	Cl...	(keV)	Counts	Mass%	Sigma	Atom%
S K	Ref.	2.307	20837.53	46.49	0.45	57.18
Ti K		4.508	15797.27	42.75	0.48	35.23
Fe K		6.398	3219.30	10.76	0.27	7.60
Total				100.00		100.00

Figure 4.21: EDS results on part of the crystal fragment showed the superstructure reflections.

Full Patterson map of the TED pattern in Figure 4.22(a) shows that the superstructure has basic vectors of $a_1 + 2a_2$ and $3a_1 - a_2$ with the unit length of $\sqrt{7}a$. Then using only the superstructure reflections, the partial Patterson map in Figure 4.22(b) shows a 6-fold symmetry with a peak in the center of each repeating unit, suggesting that Fe atoms has such a correlation in this superstructure.

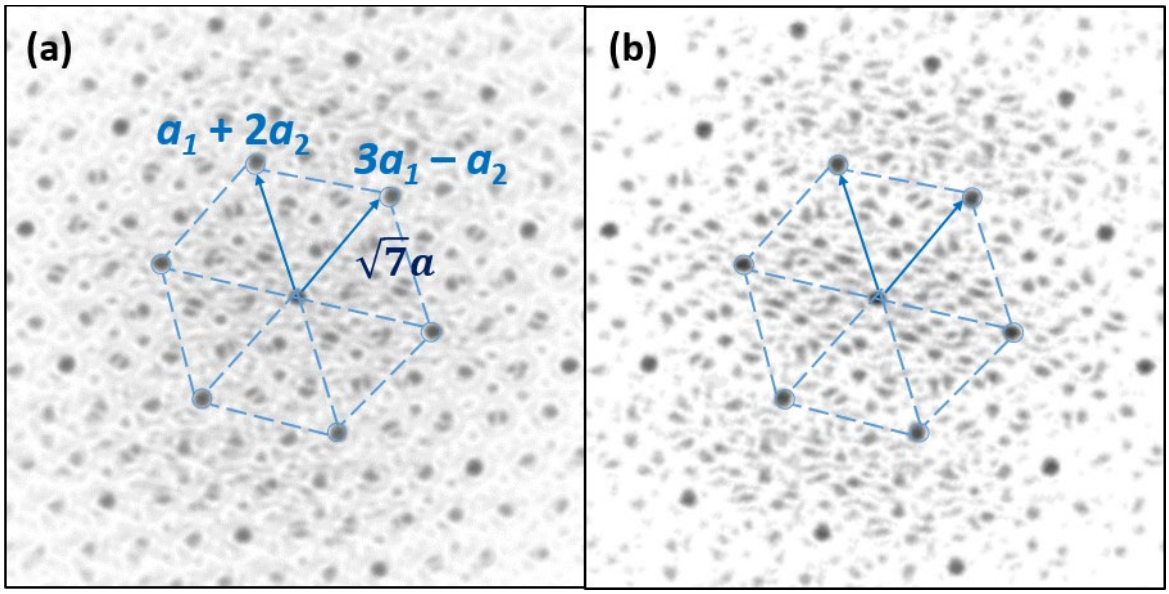

Figure 4.22: (a) Full Patterson map of the TED pattern showing a superstructure with unit size of $a_1 + 2a_2$ and $3a_1 - a_2$, and calculated unit length of $\sqrt{7}a$. (b) Partial Patterson map of the superstructure reflections in the TED pattern showing 6-fold symmetry.

Among several models of atomic arrangement of Fe atoms, the following model as shown in Figure 4.23(a) with a $2c$ ordering was proposed. This model has two Fe atoms existing in the superstructure of $\sqrt{7}a \times \sqrt{7}a \times 2c$. The Fe concentration became 0.14, which was lower than the EDS measurement. However, the simulated TED using this model in Figure 4.23(b) matched well with the experimental TED in Figure 4.23(c).

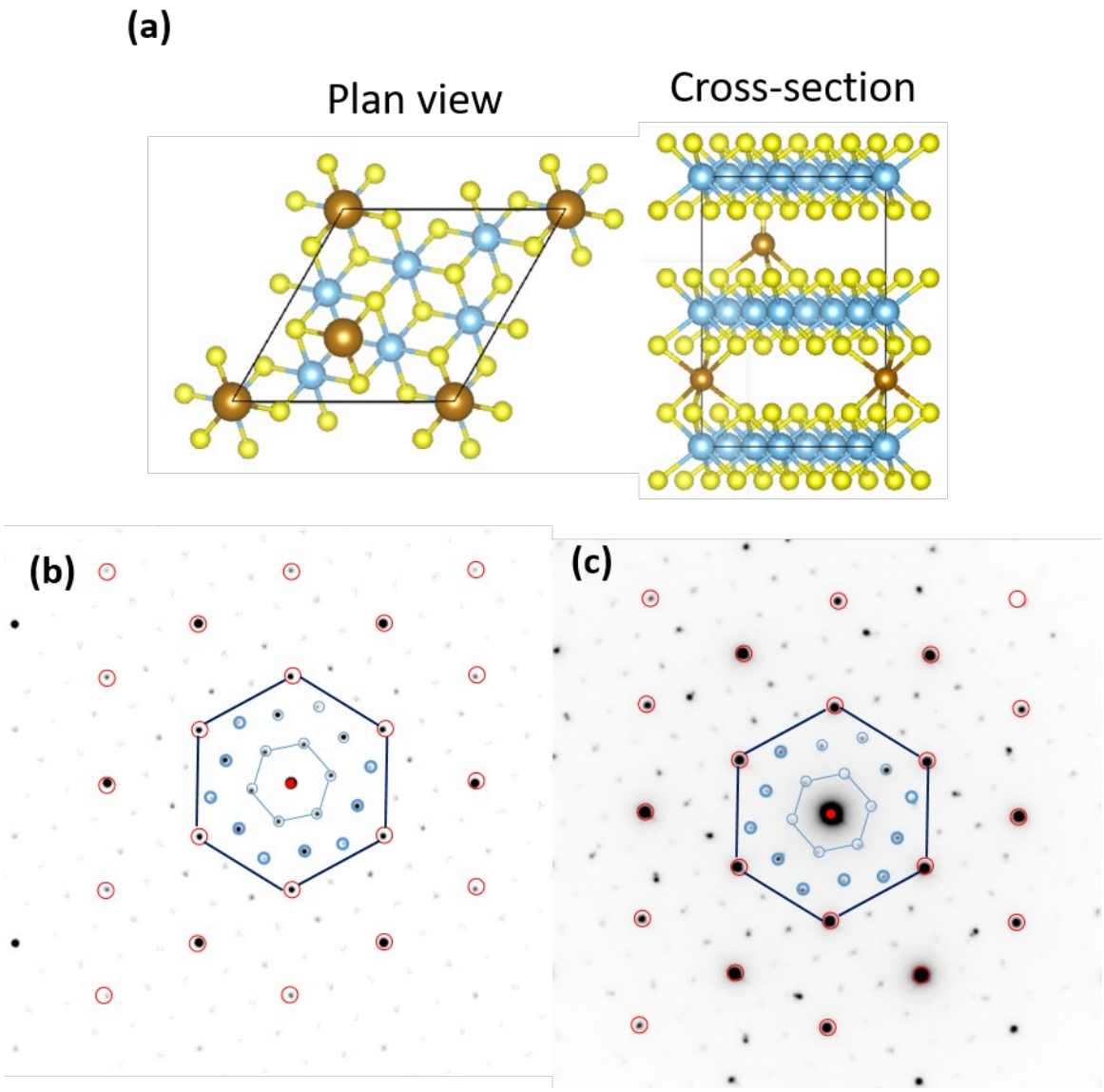

Figure 4.23: (a) $\sqrt{7}a \times \sqrt{7}a \times 2c$ atomic model used for TED simulation with 1 Fe atom in each layer of the model. (b) The reflection positions in the simulated TED matched well with the experimental TED in (c).

4.4. Conclusion

New superstructures of $\sqrt{43}a \times \sqrt{43}a \times c$, $\sqrt{31}a \times \sqrt{31}a \times c$ and $\sqrt{7}a \times \sqrt{7}a \times 2c$ were identified in Fe_xTiS_2 through Patterson analysis of the TED patterns. These Fe concentrations were 0.21, 0.29 and 0.14, respectively, which were obviously different from the nominal concentrations. The Fe atoms in these superstructures were found to occupy tetrahedral sites as well, aside from the octahedral sites. It seems that the Fe atoms would try to keep equivalent distance between each other. For both $\sqrt{43}a \times \sqrt{43}a \times c$ and $\sqrt{31}a \times \sqrt{31}a \times c$ structures, seven Fe atoms distanced themselves at $2.08a$ and formed hexagonal clusters at the edges of the superstructures.. This finding is almost consistent with the STEM observation, in which the Fe atoms would preferentially distanced themselves at $2a$ when the concentration became higher than 0.20. Since these superstructures were only observed in certain crystal fragments of the single crystals, this suggest that the formation of these new superstructures is a result of irregular arrangement of Fe atoms and it had very little effect on the magnetic properties.

CHAPTER 5

Magnetic Properties of Fe_xTiS_2

5.1. Introduction

Intercalation of foreign magnetic atoms in the van der Waals gaps of TMDC materials is a significant approach in introducing new capabilities for TMDC materials. Extensive studies have been done to tune the magnetic properties of the intercalated TMDC by modifying the nature and concentration of the magnetic intercalates. Examples of such intercalated TMDC materials are M_xTiS_2 where M is a transition metal such as V, Cr, Mn, Fe, and Co. Depending on the type of intercalated transition metals and the concentrations of the intercalated atoms, different magnetic orders are displayed. Taking M_xTiS_2 as an example, V_xTiS_2 and Mn_xTiS_2 at $x \leq 0.1$ were found to be paramagnetic; Cr_xTiS_2 displayed both ferromagnetic phase at $x \leq 0.75$ and antiferromagnetic phase at $x = 1$ [9], [37], [38]; Fe_xTiS_2 were found with three magnetic phase of spin glass phase at $x < 0.20$, cluster glass phase at $0.20 \leq x \leq 0.4$ and ferromagnetic phase at $0.4 \leq x \leq 1.0$ [1], [2], [39], whereby they displayed sharp switching and large magnetoresistance [5]. The types of chalcogen in the TMDC also affect the magnetic ordering that would be displayed by the intercalated material because of the bonding between chalcogen and intercalates. For example, Cr_xTiSe_2 at $x \geq 0.5$ [40] and Fe_xTiSe_2 at $x > 0.25$ [41] displayed only antiferromagnetic behavior, Cr_xTiTe_2 exhibited ferromagnetic behavior at $x > 0.33$ [42].

In this study, the objective was to obtain the dc magnetization measurements on Fe_xTiS_2 single crystals along the *c*-axis of the hexagonal flakes at concentrations of $x = 0.05$, 0.10, 0.15, 0.20, 0.25 and 0.33.

5.2. Methodology

Magnetic measurements were made in Quantum Design's Magnetic Property Measurement System (MPMS) that is equipped with a superconducting quantum interference device (SQUID) magnetometer. The system includes the components of a superconducting magnet to generate large magnetic fields, a superconducting detection coil which couples inductively to the sample, a SQUID connected to the detection coil and a superconducting magnetic shield surrounding the SQUID, as shown in Figure 5.1 [43]. A SQUID is consisted of a closed superconducting loop that includes one or two Josephson junctions in the loop's current path and thus it can measure extremely subtle changes in the magnetic flux, with sensitivity down to 1×10^{-8} emu [44].

Measurement is performed in the MPMS by moving the sample through the superconducting detection coils, located at the center of the magnet. As the sample moves through the coils, the magnetic moment of the sample induces an electric current in the detection coils, which in turn produces a change in the superconducting loop of SQUID. So, the SQUID functions as a highly linear current-to-voltage convertor, whereby the variation in the current of the detection coils leads to a variation in the SQUID output voltage that is proportional to the magnetic moment of the sample.

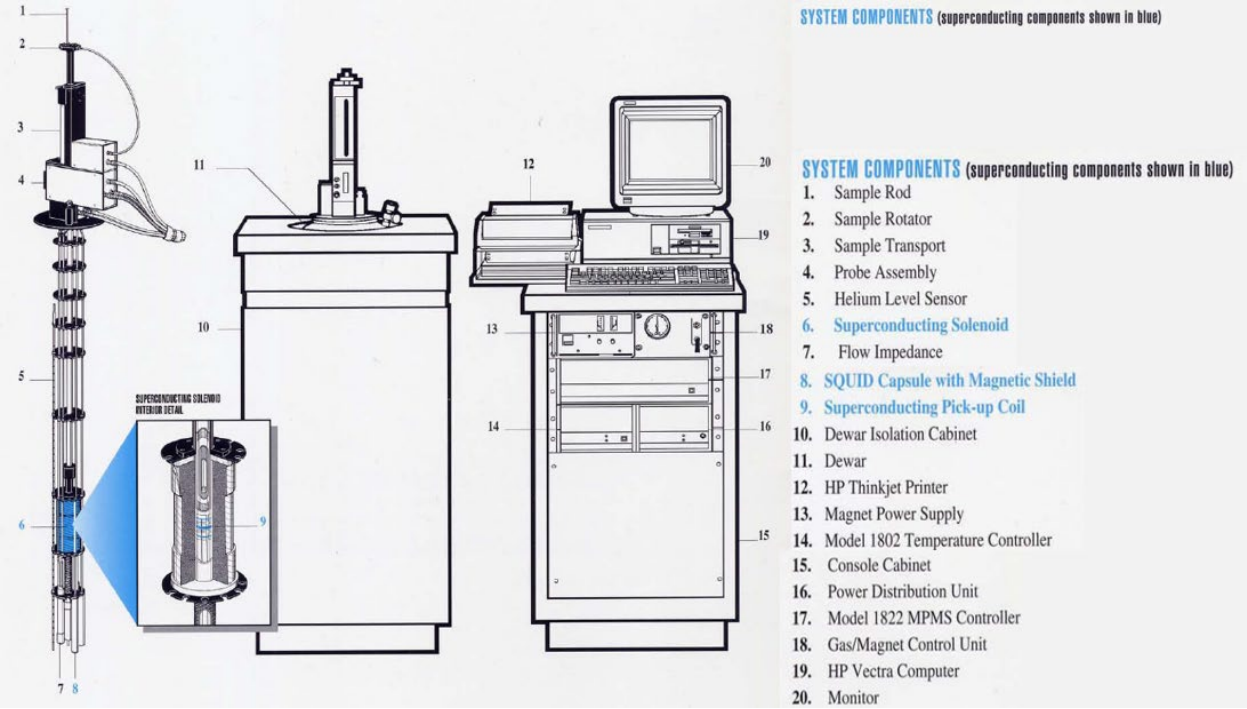

Figure 5.1: Components in MPMS system [43].

The samples for magnetic measurement have to be specially prepared in a 15 cm plastic straw so that it could be attached to the end of the MPMS sample rod. An example of the prepared plastic straw is shown in Figure 5.2.

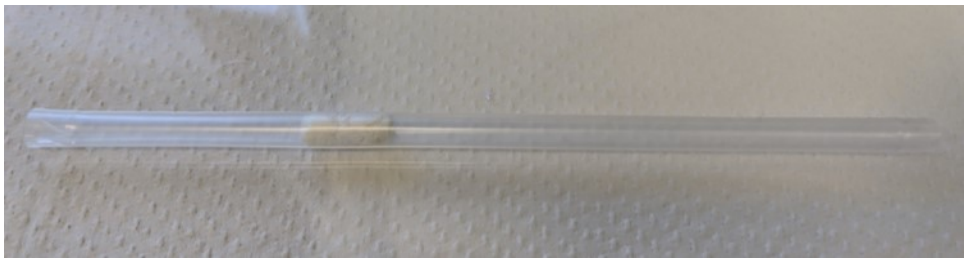

Figure 5.2: Plastic straw with sample sandwiched between two pieces of Kimwipe for magnetic measurements.

To ensure that the magnetic measurements are accurate for all samples, the weight of Kimwipe pieces and the Apiezon high vacuum grease used had to be same for each sample. Kimwipe pieces

were used to keep the samples in place for magnetic measurement. First, a piece of the Kimwipe was crumpled into a ball and pushed into the straw at a distance of 10 cm from one end. Depending on the sample sizes, either a piece of sample or 10 pieces of samples were placed onto the Kimwipe. Details on the samples are as shown in Table 5.1. The samples are arranged so that the flakes lie flat on the Kimwipe. The second piece of Kimwipe was then pushed in to keep the sample stationary during magnetic measurement. Next, the ends of the Kimwipe were sealed with the grease. One end of the plastic straw was then connected to a Delrin cap, fixed with cellophane tape. Some holes were introduced in the plastic straw above and below the Kimwipe so that the region inside the straw could be vacuumed down as well in the vacuum chamber.

Table 5.1: Preparation details for each sample.

Sample	Kimwipe weight (mg)	Grease weight (mg)	Sample weight (mg)	Number of samples
$x = 0.05$	89.09	2.82	1.45	10 to 20
$x = 0.10$	88.55	2.98	0.68	10 to 20
$x = 0.15$	89.04	2.71	2.71	1
$x = 0.20$	88.82	2.72	2.31	10 to 20
$x = 0.25$	88.91	2.68	5.58	1
$x = 0.33$	89.14	2.73	0.93	1

In this study, the dc magnetic measurements were performed in the temperature range of 5 K to 100 K and in the magnetic fields up to 60 kOe to study the temperature dependence of dc magnetization and the hysteresis loops. Demagnetization corrections were also applied onto the M-H plots to account for the effective magnetic field acting on the sample.

5.3. Results and Discussion

5.3.1. DC Magnetic Measurements of Fe_xTiS_2 Crystals

The temperature dependence of the dc magnetization measured in a static field of 1000 Oe is shown in Figure 5.3, for the samples of x = 0.05, 0.10, 0.15, 0.25 and 0.33. Both field-cooled (FC) and zero-field cooled (ZFC) data are shown as black curves and red curves, respectively. During ZFC, the magnetic moment spins were frozen in random orientations. When the temperature was raised from 5 K to 100 K, the frozen Fe spins started to align themselves to the direction of the applied magnetic field. However, upon reaching a transition temperature, thermal agitation became dominant and the spins started to align randomly. This caused a paramagnetic decrease in the magnetization values. Thus, the maxima in the ZFC peak is said to be the spin freezing temperature or glass transition temperature T_f. As the sample was slowly cooled down from 100 K to 5K in the FC measurement, the spin movement decreased again and thus led to a continuous increase of magnetization values, even after the transition temperature. This explained why the ZFC and FC curves bifurcated. The low magnetization values and the shape of the FC curves for x = 0.05, 0.10 and 0.15 indicated spin glass behavior. The slow rise of magnetization upon the ZFC-FC bifurcation is a sign of spin glass behavior [1]. The lowest Fe concentration at x = 0.05 showed a sharper cusp for the ZFC magnetization, which further proved the spin glass behavior at low Fe concentrations. Whereas for the samples x = 0.20, 0.25 and 0.33, the FC curves showed "Brillouin-like" temperature dependence of magnetization, which is a sign of ferromagnetic behavior [45]. An additional peak could be observed in the plots for x = 0.05 and x = 0.10 at higher temperature, 55 K for x = 0.05 and 47 K for x = 0.10. These additional peaks might be due to the non-uniform concentrations of the samples since multiple samples were used in these samples.

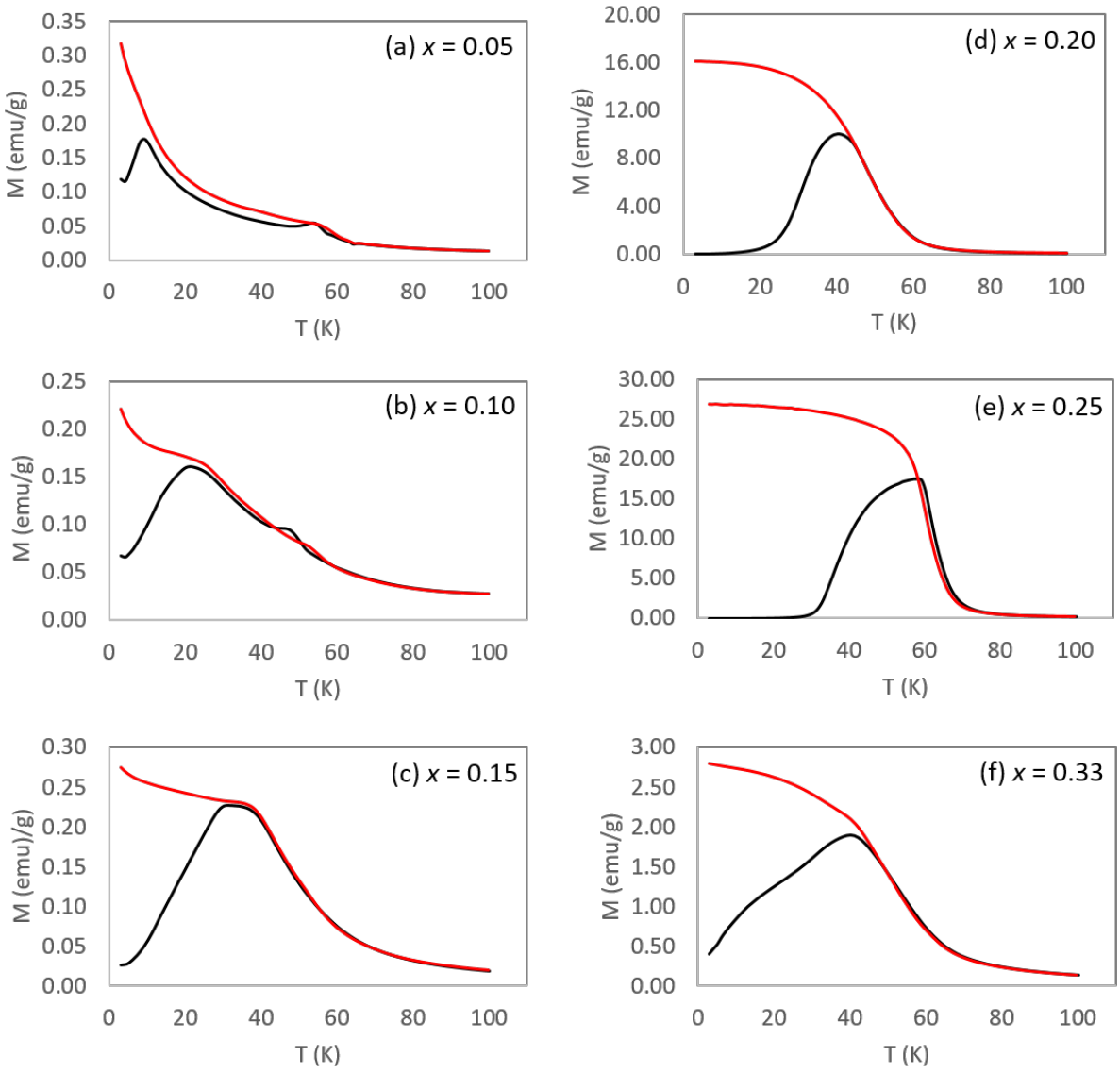

Figure 5.3: Temperature dependence of the DC magnetization for x = (a) 0.05, (b) 0.10, (c) 0.15, (d) 0.20, (e) 0.25 and (f) 0.33. ZFC curves are shown as black, whereas FC curves are shown as red.

The dependence of T_f on the concentration of Fe intercalates is shown in Figure 5.3. As concentration of Fe intercalates was increased, the transition temperature increased as well except for the case of x = 0.33. Basically, such increment trend was expected since a higher Fe concentration meant more Fe-Fe interactions. The exchange interactions might overcome the

thermal agitation of the spins and caused the spins to be aligned even at a higher temperature. However, when the concentration was increased to $x = 0.33$, it showed lower magnetization value and transition temperature. One possible reason for the reduction in the magnetization values is the different magnetic exchange interactions of two Fe atoms at different distance. Magnetic properties do not only depend on the distance of the nearest neighbor Fe atoms, but also those of second, third nearest neighbors and so forth. In the case of $2a \times 2a$ structure for the $x = 0.25$ sample, the first, second and third nearest neighbors are $2a$, $2\sqrt{3}a$ and $4a$, respectively. Whereas for $\sqrt{3}a \times \sqrt{3}a$ structure for the $x = 0.33$ sample, they are $\sqrt{3}a$, $3a$ and $2\sqrt{3}a$, respectively. Tazuke et al. [46] calculated the RKKY interaction constants of Fe_xTiS_2 up to 5th neighbors in the Fe layer, as shown in Figure 5.5. They found that the interactions between the Fe spins at the origin, indicated by the circle and Fe-spin at various sites in the Fe-layer were a combination of both ferromagnetic and antiferromagnetic interactions. Positive arrows indicate ferromagnetic interactions and negative arrows indicate antiferromagnetic interactions. The final magnetic behavior displayed by the material is then a summation of these interaction constants. So, referring to this chart, we could see that the interaction constants for the $2a \times 2a$ superstructure at $2a$, $2\sqrt{3}a$ and $4a$ distances (red open circles) were all positive interactions and thus accounted for the high magnetization value displayed in the $x = 0.25$ sample. However, for the $\sqrt{3}a \times \sqrt{3}a$ superstructure, a combination of positive and negative interactions were obtained at $\sqrt{3}a$, $3a$ and $2\sqrt{3}a$ distances (blue solid circles) and this weakened the overall ferromagnetic interactions between the Fe spins. So, this led to lower magnetization value for $x = 0.33$ and the spins were only able to be aligned at a lower temperature.

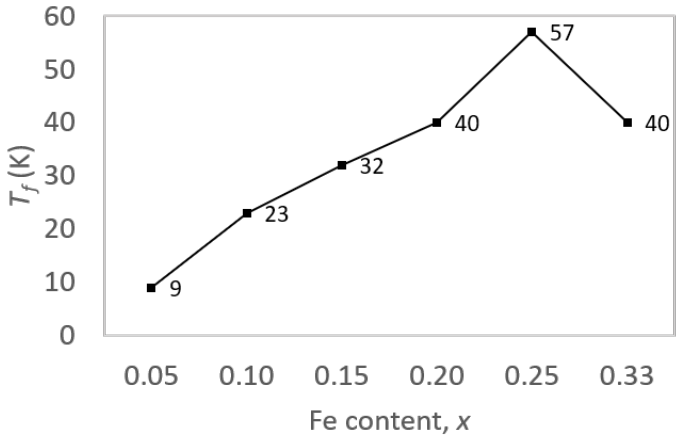

Figure 5.4: Fe concentration dependence of T_f at a static magnetic field of 1000 Oe.

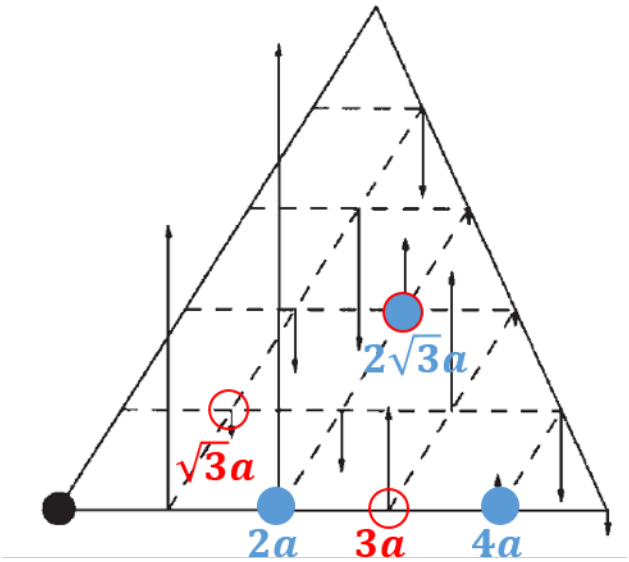

Figure 5.5: Calculated RKKY interaction constants between the Fe-spin at the origin indicated by the circle and Fe-spin at various sites in the Fe layer for $Fe_{0.12}TiS_2$. Red open circles indicate the first three nearest neighbors for $\sqrt{3}a \times \sqrt{3}a$ superstructure and blue solid circles indicate the first three nearest neighbors for The lengths of the arrow correspond to the magnitude of interaction constants on an arbitrary scale and the direction of the arrow show the positive (ferromagnetic) and negative (antiferromagnetic) values [46].

The M-H plots at the temperatures of 5 K, 25 K and 100 K for Fe_xTiS_2 ($0.05 \leq x \leq 0.33$) are shown in Figure 5.6. At low temperature of 5 K, hysteresis loops were observed for all samples. The shapes of the hysteresis loops for the higher Fe concentration ($x \geq 0.20$), with the presence of saturation magnetization and swift change of magnetization at the ends of the loops, were clear indications of ferromagnetic behaviors. Whereas the hysteresis loops at lower Fe concentrations ($x \leq 0.15$) showed typical features of spin glass behavior. The magnetization M increased slowly as H increased and could not reach saturation. When the temperature was increased to 25 K, the higher Fe concentration samples ($x \geq 0.20$) still showed hysteresis loop, since the measurement temperature was still lower than the spin freezing temperature, as seen in the M-T plots but for lower Fe concentrations ($x \leq 0.15$), the samples already started to exhibit paramagnetic behavior. This observation matched the data of spin freezing temperature. A much lower temperature is required to align the spins at these concentrations. At 100 K, no hysteresis loops were observed for all samples since the temperature was way above the determined spin freezing temperatures. The samples of $x = 0.15$, 0.20, 0.25 and 0.33 displayed paramagnetic behavior but the samples of $x = 0.05$ and 0.10 displayed diamagnetic behavior. The diamagnetic behaviors displayed by these two samples might be due to the background signals of the Kimwipe and plastic straw.

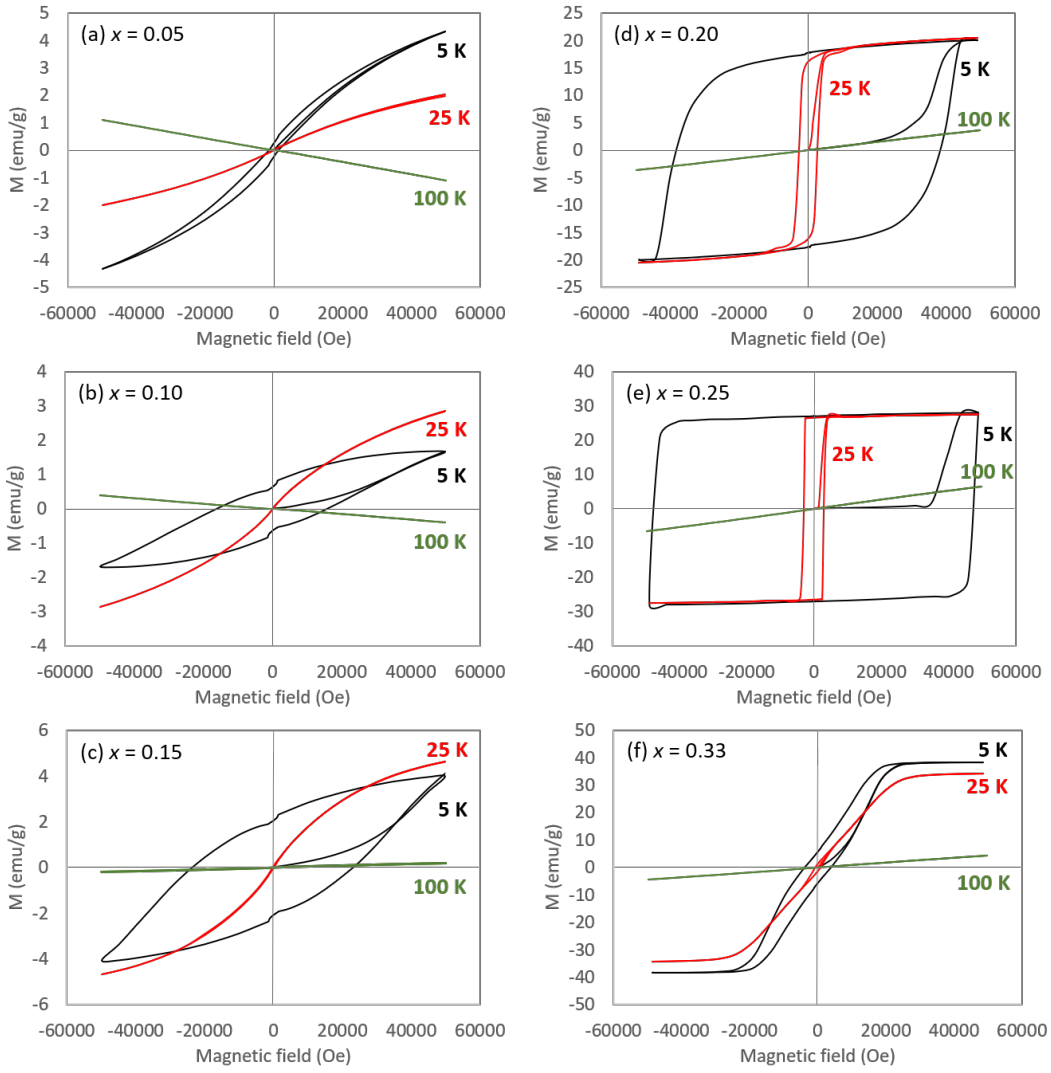

Figure 5.6: M-H curves for x = (a) 0.05, (b) 0.10, (c) 0.15, (d) 0.20, (e) 0.25 and (f) 0.33.

Figure 5.7 shows the saturation magnetization values in the hysteresis loops at different Fe concentrations at the temperature of 5 K. The saturation magnetization values for the lower Fe concentrations were obtained by fitting the curves to the Brillouin function. In this plot, the samples can be distinguished into two groups clearly because of the magnetization values. The three samples at lower Fe concentrations (x = 0.05, 0.10 and 0.15) display spin glass behaviors with lower magnetization values, whereas the samples at higher Fe concentrations (x = 0.20, 0.25

and 0.33) were ferromagnetic in nature with larger magnetization values and with increasing trend. Saturation magnetization is only achieved when all the spins were aligned in the same direction and so its value is dependent on the number of Fe spins available in the sample Thus, an increasing trend is expected for higher Fe content. The shape of the hysteresis curve, however, is dependent on the exchange interactions. As explained in earlier section, the Fe spins in x = 0.33 had both ferromagnetic and antiferromagnetic interactions depending on the interatomic distance. So, the antiferromagnetic interactions would resist the alignment of the spins to the direction of applied field and resulted in a slower rise in magnetization value as compared to x = 0.25.

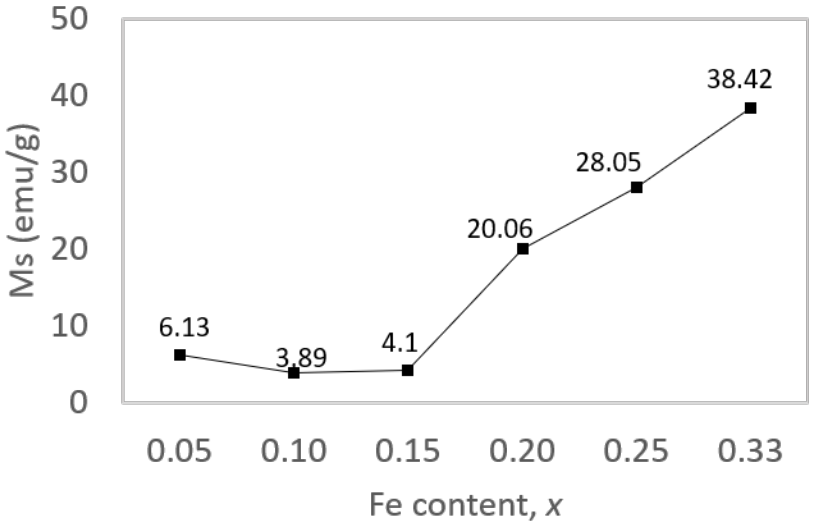

Figure 5.7: Fe concentration dependence of M_s at 5 K.

5.3.2. Discussion

The magnetic results show that x = 0.20 is the onset of ferromagnetic behavior. This finding coincide with the Fe ordering identified from the STEM observation, as shown in Figure 5.8, since the STEM results show that x = 0.20 is the onset of 3D ordering of Fe atoms as well. It indicates the 3D ordering of Fe atoms may be related to the ferromagnetic property of Fe_xTiS_2.

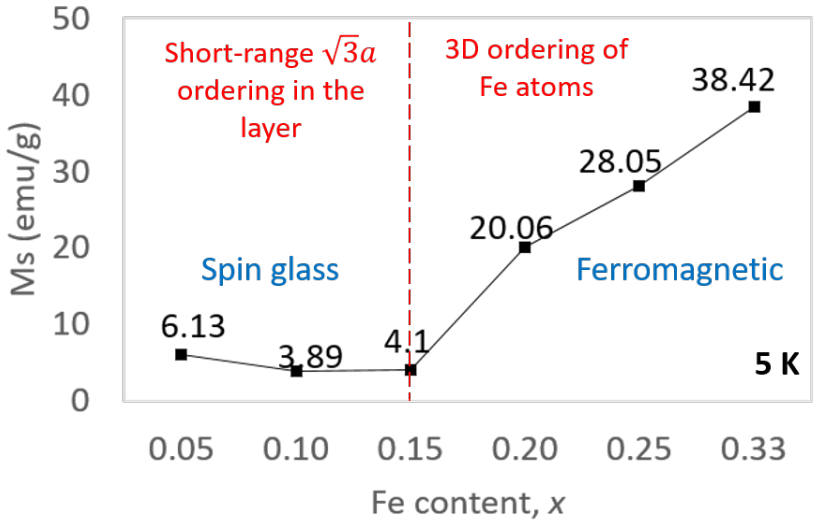

Figure 5.8: A clear structural-properties correlation could be observed from the Fe concentration dependence of M_s at 5, showing $x = 0.20$ as the starting point in which the crystals started to order three-dimensionally and switch from spin glass behavior to ferromagnetic behavior.

We propose the following explanation to correlate the Fe ordering observed and the magnetic properties measured. At concentrations above 0.20, 3D ordering of the Fe atoms is formed, which may have led to stronger exchange interactions of two Fe atoms (ions) in the layers and between the layers. It may cause the spins to align easier to the applied magnetic field showing ferromagnetic behavior. At concentrations less than 0.20, since the atoms only have short-range ordering of Fe atoms within the plane, the main contribution to the magnetic behavior comes from the exchange interactions of two Fe atoms (ions) in the layers and with diluted effect from the interlayered Fe atoms. Due to the large average distance between two Fe atoms, the average exchange interactions may be weak. Therefore, at concentrations less than 0.20, spin glass or cluster glass behavior is exhibited.

Comparing our results with previous studies, our samples already displayed ferromagnetic behavior at a lower Fe concentration of $x = 0.20$ which was a match with the study by Choe et al.

[5] but differed with the study by Negishi et al. and Yoshioka et al. [37], [47] in which the Fe_xTiS_2 crystals exhibited ferromagnetic behavior above Fe concentration of 0.40. One possible reason for such different magnetic properties may be due to the synthesis route of the crystals. We found a slight change in the temperature, the dimensions of the glass tube and amount of raw materials affected the growth and resulted in different crystalline quality or distribution of Fe atoms. However, we could not comment about this, since there was not much information given in their papers on the synthesis method.

5.4. Conclusion

DC magnetization measurements had been performed on Fe_xTiS_2 at the concentrations of x = 0.05, 0.10, 0.15, 0.20, 0.25 and 0.33. The results clearly showed that at lower concentrations of Fe intercalates ($x \leq 0.15$), the samples displayed spin glass behavior such as the lower magnetization values and the concave shape of the hysteresis loop. While for the higher concentrations of Fe intercalates ($x \geq 0.20$), the samples displayed clear ferromagnetic behavior.

The onset of ferromagnetic behavior at x = 0.20 coincided with the onset of 3D Fe ordering at x = 0.20 from the STEM results. So, we propose that 3D ordering of Fe atoms has an important influence on the magnetic phase transition between spin glass phase and ferromagnetic one.

CHAPTER 6

General Conclusion

Understanding of the arrangement of Fe atoms in the Fe_xTiS_2 at different Fe concentrations is essential in the engineering of materials so that the desired properties can be tuned correctly for their application. This is the first reported work to obtain the Fe ordering of Fe_xTiS_2 using TED, STEM, EELS and EDX at the concentrations of $0 \leq x \leq 0.33$. Magnetic measurements were obtained as well and the different behavior observed could be attributed to the type of Fe ordering in the material. Figure 6.1 shows a summary of the structures identified and the corresponding magnetic behavior of the Fe_xTiS_2 single crystals at different concentrations.

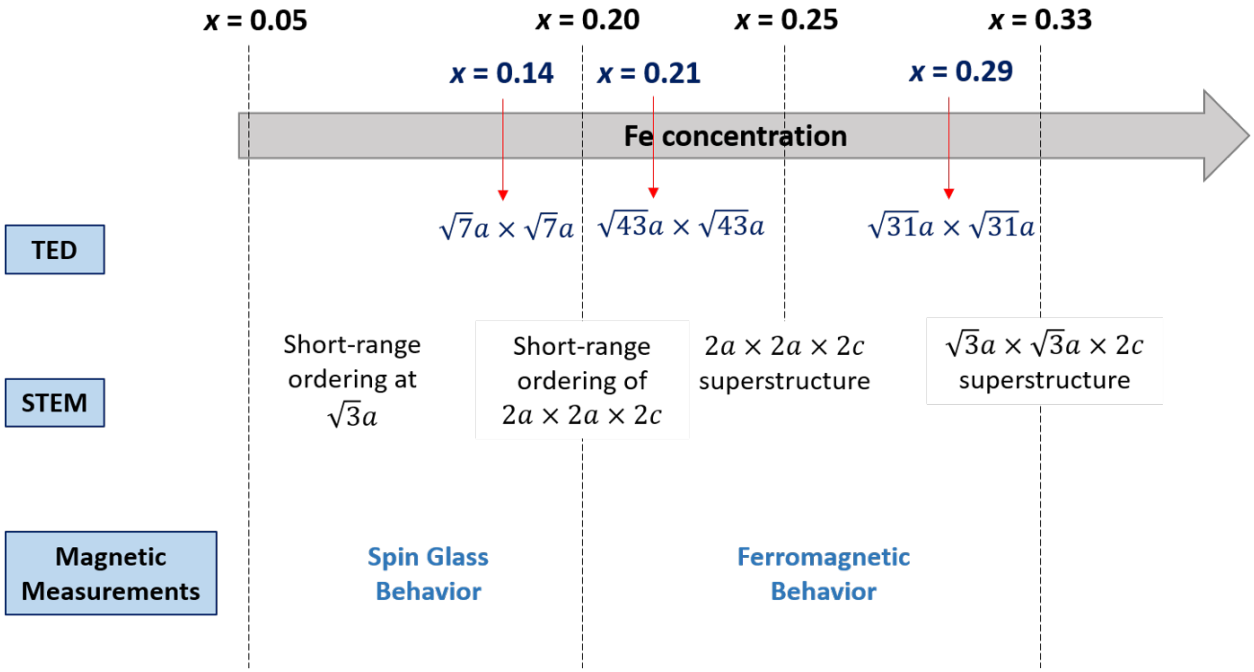

Figure 6.1: A summary of the structures identified for Fe_xTiS_2 single crystals and their corresponding magnetic behavior.

Several new findings in this study are as follow. First, through STEM observation, we found that the Fe atoms preferentially made short range ordering of $\sqrt{3}a$ distance at low concentrations ($x \leq 0.15$), as opposed to $2a$ distance in previous studies. As the concentration was increased, the Fe atoms started to be ordered three-dimensionally forming long-range ordering of $2a \times 2a \times 2c$ at $x = 0.20$ and 0.25, but then switched to $\sqrt{3}a \times \sqrt{3}a \times 2c$ ordering at $x = 0.33$. We think that the ordering may be a result of the pair-interactions between the Fe atoms. At low concentrations ($x \leq 0.15$), the Fe atoms were repulsed from each other but with no influence from Fe atoms in neighboring layers, as indicated by the cross-sectional STEM images. At higher concentrations with more Fe atoms between layers, the ordering of Fe atom was influenced by both Fe atoms in the layer and between the layers, thus creating 3D superstructures, with the Fe atoms separated further apart at $2a$ distance at $x = 0.20$ and 0.25. At $x = 0.33$, due to the limited interstitial sites available, the Fe atoms were then arranged closer together and formed the $\sqrt{3}a$ superstructure.

From the TED analysis, we found new superstructures of $\sqrt{43}a \times \sqrt{43}a$, $\sqrt{31}a \times \sqrt{31}a$ and $\sqrt{7}a \times \sqrt{7}a \times 2c$ that were never reported before. Since some Fe atoms were observed at S sites as well, the formation of these superstructures might be due to arrangement of Fe atoms that involve both octahedral and tetrahedral sites.

Through the magnetic measurements, the samples displayed spin glass behavior at low Fe concentrations ($x = 0.05$, 0.10 and 0.15) and ferromagnetic behavior at higher Fe concentrations ($x = 0.20$, 0.25 and 0.33). $x = 0.20$ showed the onset of ferromagnetic behavior, which matched the onset of 3D Fe ordering in the STEM observation. So, the switch from 2D ordering within the plane to 3D ordering at higher Fe concentrations might have caused the material to switch from spin glass behavior to ferromagnetic behavior since 3D Fe ordering would allow stronger exchange interactions between the Fe atoms.

BIBLIOGRAPHY

[1] M. Koyano, M. Suezawa, H. Watanabe, and M. Inoue, "Low-field magnetization and ac magnetic susceptibility of spin-and cluster-glasses of itinerant magnet Fe_xTiS_2," *Journal of the Physical Society of Japan*, vol. 63, no. 3, pp. 1114–1122, 1994.

[2] H. Negishi, S. Ohara, M. Koyano, M. Inoue, T. Sakakibara, and T. Goto, "Anisotropic Spin-Glass and Cluster-Glass of Layered Fe_xTiS_2 Crystals," *Journal of the Physical Society of Japan*, vol. 57, no. 12, pp. 4083–4085, 1988.

[3] G. V. S. Rao and M. W. Shafer, "Intercalation in Layered Transition Metal Dichalcogenides," in *Intercalated Layered Materials*, F. Lévy, Ed. Dordrecht: Springer Netherlands, 1979, pp. 99–199.

[4] Y. Kuroiwa, M. Nishimura, Y. Noda, and Y. Morii, "Neutron powder diffraction study of intercalation compound Fe_xTiS_2," *Physica B: Condensed Matter*, vol. 213–214, pp. 396–398, Aug. 1995.

[5] J. Choe, K. Lee, C.-L. Huang, N. Trivedi, and E. Morosan, "Magnetotransport in Fe-intercalated TS2: the comparison between T = Ti and Ta," *Phys. Rev. B*, vol. 99, no. 6, p. 064420, Feb. 2019.

[6] M. Kertesz and R. Hoffmann, "Octahedral vs. trigonal-prismatic coordination and clustering in transition-metal dichalcogenides," *J. Am. Chem. Soc.*, vol. 106, no. 12, pp. 3453–3460, Jun. 1984.

[7] M. S. Dresselhaus, *Intercalation in Layered Materials*. Springer, 2013.

[8] J. Rouxel, L. Trichet, P. Chevalier, P. Colombet, and O. A. Ghaloun, "Preparation and structure of alkali metal intercalation compounds," *Journal of Solid State Chemistry*, vol. 29,

no. 3, pp. 311–321, Sep. 1979.

[9] M. Inoue, H. P. Hughes, and A. D. Yoffe, “The electronic and magnetic properties of the 3d transition metal intercalates of TiS_2,” *Advances in Physics*, vol. 38, no. 5, pp. 565–604, Jan. 1989.

[10] D. B. Williams and C. B. Carter, *Transmission Electron Microscopy: A Textbook for Materials Science*. Springer Science & Business Media, 2009.

[11] R. F. Egerton, *Physical principles of electron microscopy*. New York, NY: Springer Berlin Heidelberg, 2016.

[12] “分析豆知識 | ユーロフィンイーエージー株式会社.” http://www.nanoscience.co.jp/knowledge/TEM/knowledge01.html (accessed May 05, 2020).

[13] “Keywords ‘annular’ | Keywords | Glossary of TEM Terms | JEOL.” https://www.jeol.co.jp/en/words/emterms/search_result.html?keyword=annular (accessed May 06, 2020).

[14] P. Champness, *An Introduction to Electron Diffraction in the Transmission Electron Microscope*. BIOS Scientific Publishers, 2001.

[15] J. M. D. Coey, *Magnetism and Magnetic Materials*. Cambridge University Press, 2010.

[16] D. C. Jiles, *Introduction to Magnetism and Magnetic Materials, Second Edition*. CRC Press, 1998.

[17] H. D. Young, *University physics.*, 8th ed. Reading, Mass: Addison-Wesley Pub. Co., 1992.

[18] P. Young, Ed., “Quadrupolar spin glasses,” in *Series on Directions in Condensed Matter Physics*, vol. 12, WORLD SCIENTIFIC, 1997, pp. 99–118.

[19] S. Kirkpatrick, “Frustration and ground-state degeneracy in spin glasses,” *Phys. Rev. B*, vol. 16, no. 10, pp. 4630–4641, Nov. 1977.

[20] S. Nagata, P. Keesom, and H. Harrison, “Low-dc-field susceptibility of CuMn spin glass,” *Physical Review B*, vol. 19, pp. 1633–1638, Feb. 1979, doi: 10.1103/PhysRevB.19.1633.

[21] G. Toulouse, “Theory of the frustration effect in spin glasses,” *Communications Physics*, vol. 2, p. 115, 1977.

[22] N. A. Spaldin, *Magnetic Materials: Fundamentals and Applications*. Cambridge University Press, 2010.

[23] S. Negishi, H. Negishi, M. Sasaki, and M. Inoue, “Montecarlo Simulation of Intercalated Atomic Distributions in Layered Dichalcogenide,” *Molecular Crystals and Liquid Crystals Science and Technology. Section A. Molecular Crystals and Liquid Crystals*, vol. 341, no. 2, pp. 69–74, Apr. 2000.

[24] B. Gu, Q. Song, and J. Ni, “Unified model for ordering and staging of intercalated M ions in M_xTiS_2,” *Journal of Applied Physics*, vol. 85, no. 2, pp. 819–824, Jan. 1999.

[25] F. Pawula *et al.*, “Anisotropic thermal transport in magnetic intercalates Fe_xTiS_2,” *Phys. Rev. B*, vol. 99, no. 8, p. 085422, Feb. 2019.

[26] 水田耀ピエール, “遷移金属層間化合物 $Fe_{0.33}TiS_2$ における異常 Hall 効果,” 金沢大学大学院, Jun. 2016.

[27] T. Malis, S. C. Cheng, and R. F. Egerton, “EELS log-ratio technique for specimen-thickness measurement in the TEM,” *J. Elec. Microsc. Tech.*, vol. 8, no. 2, pp. 193–200, Feb. 1988.

[28] K. Iakoubovskii, K. Mitsuishi, Y. Nakayama, and K. Furuya, “Thickness measurements with electron energy loss spectroscopy,” *Microscopy Research and Technique*, vol. 71, no. 8, pp. 626–631, 2008.

[29] L.-M. Peng, G. Ren, S. L. Dudarev, and M. J. Whelan, “Debye–Waller Factors and Absorptive Scattering Factors of Elemental Crystals,” *Acta Crystallographica Section A*, vol. 52, no. 3,

pp. 456–470, 1996.

[30] S. Gražulis *et al.*, “Crystallography Open Database – an open-access collection of crystal structures,” *Journal of Applied Crystallography*, vol. 42, no. 4, pp. 726–729, Aug. 2009.

[31] Y. Kuroiwa, H. Honda, and Y. Noda, “Neutron Magnetic Scattering of Intercalation Compounds Fe_xTiS_2,” *Molecular Crystals and Liquid Crystals Science and Technology. Section A. Molecular Crystals and Liquid Crystals*, vol. 341, no. 2, pp. 15–20, Apr. 2000.

[32] K. J. Koski, C. D. Wessells, B. W. Reed, J. J. Cha, D. Kong, and Y. Cui, “Chemical Intercalation of Zerovalent Metals into 2D Layered Bi2Se3 Nanoribbons,” *J. Am. Chem. Soc.*, vol. 134, no. 33, pp. 13773–13779, Aug. 2012.

[33] A. L. Patterson, “A Fourier Series Method for the Determination of the Components of Interatomic Distances in Crystals,” *Phys. Rev.*, vol. 46, no. 5, pp. 372–376, Sep. 1934.

[34] A. Monge, M. Martínez-Ripoll, and S. García-Blanco, “The adduct zinc dicyanide–bis(2,9-dimethyl-1,10-phenanthroline) trihydrate,” *Acta Cryst B*, vol. 34, no. 9, Art. no. 9, Sep. 1978.

[35] K. Takayanagi, Y. Tanishiro, S. Takahashi, and M. Takahashi, “Structure analysis of Si(111)-7 × 7 reconstructed surface by transmission electron diffraction,” *Surface Science*, vol. 164, no. 2–3, pp. 367–392, Dec. 1985.

[36]K. Motizuki and N. Suzuki, “Intercalation Compounds of Transition-Metal Dichalcogenides,” in *Physics of New Materials*, F. E. Fujita, Ed. Berlin, Heidelberg: Springer, 1994, pp. 106–138.

[37] H. Negishi, A. Shoube, H. Takahashi, Y. Ueda, M. Sasaki, and M. Inoue, “Magnetic properties of intercalation compounds M_xTiS_2 (M = 3d transition metal),” vol. 67, pp. 179–186, 1987.

[38] H. Negishi, M. Koyano, M. Inoue, T. Sakakibara, and T. Got, “High field magnetization of 3d transition metal intercalates M_xTiS_2 (M = 3d metals),” vol. 74, pp. 27–30, 1988.

[39] H. Negishi, H. Takahashi, and M. Inoue, “Linear and nonlinear AC magnetic susceptibilities in intercalation compound Fe_xTiS_2,” *Journal of Magnetism and Magnetic Materials*, vol. 68, pp. 271–279, 1987.

[40] N. V. Baranov, A. N. Titov, V. I. Maksimov, N. V. Toporova, A. Daoud-Aladine, and A. Podlesnyak, “Antiferromagnetism in the ordered subsystem of Cr ions intercalated into titanium diselenide,” *J. Phys.: Condens. Matter*, vol. 17, no. 34, pp. 5255–5262, Aug. 2005.

[41] N. V. Baranov, N. V. Selezneva, V. G. Pleshchev, N. V. Mushnikov, and V. I. Maksimov, “Magnetic Structure and Properties of the Intercalated Compound $Fe_{0.5}TiSe_2$,” *Solid State Phenomena*, 2011.

[42] N. V. Baranov *et al.*, “Ferromagnetism and structural transformations caused by Cr intercalation into $TiTe_2$,” *J. Phys.: Condens. Matter*, vol. 21, no. 50, p. 506002, Nov. 2009.

[43] M. McElfresh, “Fundamentals of magnetism and magnetic measurements featuring Quantum Design’s magnetic property measurement system.” Quantum Design, 1994.

[44] “超伝導量子干渉磁束計・SQUID,” *JAIST 北陸先端科学技術大学院大学.* https://www.jaist.ac.jp/areas/materials-science/main-equipment/squid.html (accessed May 15, 2020).

[45] J. Wu and C. Leighton, “Glassy ferromagnetism and magnetic phase separation in $La_{1-x}Sr_xCoO_3$,” *Phys. Rev. B*, vol. 67, no. 17, p. 174408, May 2003.

[46] Y. Tazuke, Y. Ohta, and S. Miyamoto, “Exchange Interactions in Fe_xTiS_2,” *J. Phys. Soc. Jpn.*, vol. 74, no. 9, pp. 2644–2645, Sep. 2005.

[47] T. Yoshioka and Y. Tazuke, “Magnetic Properties of Fe_xTiS_2 System,” *J. Phys. Soc. Jpn.*, vol. 54, no. 6, pp. 2088–2091, Jun. 1985.

LIST OF ACHIEVEMENTS

List of Publication

- Yi Ling Chiew, Masanobu Miyata, Mikio Koyano, and Yoshifumi Oshima, "Ordering of intercalated Fe atoms in Fe_xTiS_2 structures clarified using transmission electron microscopy," *Journal of Physical Society of Japan* vol. 89, 074601, Jun. 2020.
- Yi Ling Chiew, Masanobu Miyata, Mikio Koyano, and Yoshifumi Oshima, "Study of Planar Distribution of Intercalated Fe atoms in TiS_2 Using Transmission Electron Diffraction" (in preparation).
- Yi Ling Chiew, Masanobu Miyata, Mikio Koyano, and Yoshifumi Oshima, "Correlation of Fe atomic ordering in Fe_xTiS_2 and their dc magnetic properties" (in preparation).

International Conferences

- YiLing Chiew and Yoshifumi Oshima, "Synthesis of Silver Sulfide Nanostructure and Its Microstructural Observation," Asian conference on Nanoscience and Nanotechnology, 18-21th Oct. 2018, Qingdao (China) (Poster Presentation)
- Yi Ling Chiew, Satoshi Abe, Masanobu Miyata, Mikio Koyano and Yoshifumi Oshima, "Unravelling the planar distribution of Fe intercalated atoms in TiS_2 layered structure using transmission electron diffraction," 10^{th} International Conferences on Materials for Advanced Technologies, 23 -28 June 2019, Singapore (Best Poster Award)

Domestic Conferences and Symposiums

- Yi Ling Chiew, Kuan Yew Cheong, Yoshifumi Oshima, "Growth of SiC Nanowires and Nanocones Using Mixture of Oil Palm Fibres and Rice Husk Ash," 65th JSAP Spring Meeting, 19th, March,2018 (Waseda Univ.) (Poster Presentation)
- Yi Ling Chiew, Satoshi Abe, Masanobu Miyata, Mikio Koyano and Yoshifumi Oshima, "Determination of intercalated Fe atomic arrangement in TiS_2 layers using transmission electron diffraction," Jaist Japan-India Symposium on Advanced Science 2019, 8 February 2019, JAIST. (Poster Presentation)
- Yi Ling Chiew, Satoshi Abe, Masanobu Miyata, Mikio Koyano and Yoshifumi Oshima, "Determination of intercalated Fe atomic arrangement in TiS_2 layers using transmission electron diffraction," 66^{th} Japan Society of Applied Physics Spring Meeting 2019, 9 – 12 March 2019, Tokyo. (Oral presentation)
- Yi Ling Chiew, Satoshi Abe, Masanobu Miyata, Mikio Koyano and Yoshifumi Oshima, "A TED study of intercalated Fe atomic arrangement in TiS2 layers," 75th annual meeting of the Japanese Society of microscopy, P-M_47、17th June. 2019, Nagoya Convention center (Poster Presentation)